Movement of Thumb-Base Joints

In-Vivo anatomy and biomechanics to support Implant Design

Yuan, T.

Important note
To cite this publication, please use the final published version (if applicable).
Please check the document version above.

Movement of Thumb-Base Joints: In-Vivo Anatomy and Biomechanics to Support Implant Design

MOVEMENT OF THUMB-BASE JOINTS: IN-VIVO ANATOMY AND BIOMECHANICS TO SUPPORT IMPLANT DESIGN

Dissertation

for the purpose of obtaining the degree of doctor
at Delft University of Technology,
by the authority of the Rector Magnificus, Prof.dr.ir. T.H.J.J. van der Hagen,
chair of the Board for Doctorates
to be defended publicly on
Monday, 13 November 2023 at 12:30 o'clock

by

Tianyun YUAN

Master of Science in Mechanical Engineering,
Prairie View A&M University, Texas, the United States
born in Shanghai, China.

This dissertation has been approved by the promotors.

Composition of the doctoral committee:

Rector Magnificus,   chairman
Prof. dr. ir. R.H.M. Goossens,   Technische Universiteit Delft, promotor
Dr. Y. Song,   Technische Universiteit Delft, promotor
Dr. G.A. Kraan,   Reinier Haga Orthopedisch Centrum, copromotor

Independent members
Prof. dr. P. Vink   Technische Universiteit Delft
Prof. dr. J.A.C. Rietjens   Technische Universiteit Delft
Prof. dr. G.J. Kleinrensink   Erasmus Medical Center
Dr. J.M. Colaris   Erasmus Medical Center

Reserve member
Prof. ir. D.J. van Eijk   Technische Universiteit Delft

CONTENTS

SUMMARY

"HUMAN hands are one of the most intimate organs" [a], that are well-developed in the course of evolution. The hands enable us to express emotions (e.g., anger, anxiety), protect ourselves (e.g., from falls), exchange information (e.g., through sign language), identify different objects (e.g., textures, sizes, shapes), manipulate various tools (e.g., pens, screws), etc. The thumb, in particular, plays a crucial role in manipulation tasks such as using smartphones and writing. The base joint of the thumb – the carpometacarpal (CMC-1) joint – allows it to move in opposition to the other fingers for firm grips and precise object control. This dexterity is essential for our daily activities.

However, the thumb can experience reduced mobility and functionality as a result of osteoarthritis. Osteoarthritis is a degenerative disease that leads to irreversible joint damage and disability. Among all joints in the hand, degeneration at thumb-base joints is strongly associated with painful feelings and manipulation disability. Joint replacement is one of the surgical options that can restore joint mobility and functionality. Yet, the high revisit/failure rate and short durability of the replacements for the thumb-base joint underline the need for a more comprehensive understanding of the anatomy and biomechanics of this critical joint.

The in-vivo measurement (in and on the body), and research on the thumb-base joint are challenging because it is a small saddle joint that is covered by several layers of ligaments (connective tissue that protects the joint and holds bones together) and muscles. By taking advantage of 4D CT scanning, this dissertation reaches this delicate and deep joint and explores the bone shape and joint movement among healthy participants to answer the main research question: "What is the natural state of asymptomatic CMC-1 (the thumb-base joint)?". These deeper insights into the structure and mechanics of the thumb-base joints are crucial for studying the etiology of thumb-base osteoarthritis and informing the enhancement of treatment designs. The findings based on the healthy nature of the thumb-base joint can serve as a valuable reference for optimizing thumb-base implant replacements, resulting in improved long-term outcomes.

The bone shape of the trapezium and the 1st metacarpal bones were first investigated with both within-subject and between-subject shape variances analysis (Chapter 2). An interesting finding was that the bones on the dominant side were slightly but consistently larger than the bones on the non-dominant side. Results implied the association between bone shape and joint movement.

Subsequently, the relative movement of the 1st metacarpal bone to the trapezium during maximum thumb circumduction was assessed, focusing on joint contact

---

[a]Prof.Dr. Gert-Jan Kleinrensink, professor of Anatomy, lecture

(Chapter 3) and the motion boundary trace (Chapter 4). In one full circle of movement, the thumb-base joint for females exhibited a higher recurrence frequency and a greater contact ratio. This finding indicates that a larger portion of the articulate surface for females experienced constant stress in most scenarios which can lead to more vulnerable cartilage. This can explain the higher prevalence of thumb-base osteoarthritis among females than males from a different mechanical perspective. Furthermore, the trace of the maximum reachable movement for the thumb-base joint forms a skewed hyperboloid shape, with the waist of the shape positioned on the 1st metacarpal side instead of the trapezium side. The continuous measurement results provide novel insights into the design of implant replacements for the thumb-base joint.

The last two chapters of this dissertation extend the research analysis from the skeletal system to the skin system and expand the research focus to all finger joints. An optical tracking system was implemented to capture the continuous joint rotation angles of target joints simultaneously during various tasks (Chapter 5). The comparison of the range of motion during active, functional, and passive activities (Chapter 6) revealed that the functional range of motion can exceed the active range, especially for the distal interphalangeal joint during fine manipulations. These results emphasize the importance and role of these three types of range of motion.

In conclusion, this dissertation examined bone shape, joint contact, and the active motion boundary of the thumb-base joint among participants without signs of joint degeneration. This dissertation also compares the joint movement between females and males for the etiology of thumb-base osteoarthritis. The deeper insights gained into the structure and mechanics of the thumb-base joints can help researchers and healthcare professionals improve and develop more effective treatments for patients with thumb-base osteoarthritis. Furthermore, the exploration of connecting information between the skeletal and skin systems opens up possibilities for future research perspectives.

Samenvatting

"Menselijke handen behoren tot de meest intieme organen."[b], die goed zijn ontwikkeld in de loop van de evolutie. De handen stellen ons in staat om emoties uit te drukken (bijv. woede, angst), onszelf te beschermen (bijv. een val opvangen), informatie uit te wisselen (bijv. via gebarentaal), verschillende objecten te identificeren (bijv. textuur, maten, vormen), diverse gereedschappen te manipuleren (bijv. pennen, schroeven), etc. De duim speelt in het bijzonder een cruciale rol bij manipulatietaken, zoals het gebruik van smartphones en schrijven. Het basisgewricht van de duim – het carpometacarpale gewricht (CMC-1) – stelt het in staat om in oppositie te bewegen ten opzichte van de andere vingers om stevige grepen en nauwkeurige controle over objecten mogelijk te maken. Deze behendigheid is essentieel voor onze dagelijkse activiteiten.

Echter kan de duim verminderde mobiliteit en functionaliteit ervaren als gevolg van artrose. Artrose is een degeneratieve ziekte die leidt tot onomkeerbare gewrichtsschade en invaliditeit. Onder alle gewrichten in de hand wordt degeneratie van de duimbasisgewrichten sterk geassocieerd met pijn en beperkingen in de manipulatie. Gewrichtsvervanging is een van de chirurgische opties die gewrichtsmobiliteit en functionaliteit kunnen herstellen. Echter benadrukken de hoge revisie-/faalfrequentie en de korte levensduur van vervangen duimbasisgewrichten de behoefte aan een breder begrip van de anatomie en biomechanica van dit cruciale gewricht.

Het in-vivo (in en op het lichaam) meten en onderzoeken van het duimbasisgewricht is uitdagend omdat het een klein zadelgewricht is dat bedekt wordt door verschillende lagen ligamenten (bindweefsel welk het gewricht beschermen en botten bij elkaar houden) en spieren. Door gebruik te maken van 4D CT-scans slaagt dit proefschrift erin van dit delicate en diep gelegen gewricht haar bot vorm en gewrichtsbeweging te onderzoeken bij gezonde participanten. Dit heeft als doel de belangrijkste onderzoeksvraag te beantwoorden van dit proefschrift: 'Wat is de natuurlijke staat van asymptomatische CMC-1 (het duimbasisgewricht)?'. Deze diepgaande inzichten in de structuur en mechanica van de duimbasisgewrichten zijn cruciaal voor het bestuderen van de oorzaken van artrose aan de duimbasis en voor het verbeteren van medische behandelingen. De bevindingen gebaseerd op de gezonde toestand van het duimbasisgewricht kunnen dienen als waardevolle referentie voor het optimaliseren van vervangende implantaten voor het duimbasisgewricht, welk kan bijdragen aan een verbeterde levensduur van vervangen duimbasisgewrichten.

De botvorm van het trapezium en de eerste middenhandsbeentjes werden eerst onderzocht door middel van een vormvariantie analyse zowel binnen (intra) als tussen (inter) proefpersonen (Hoofdstuk 2). Een interessante bevinding was dat de bot-

---

[b]Prof.Dr. Gert-Jan Kleinrensink, Hoogleraar Anatomie ErasmusMC, docenten

ten aan de dominante handzijde iets, maar consistent, groter waren dan de botten aan de niet-dominante zijde. De resultaten gaven een verband aan tussen de bot vorm en gewrichtsbeweging.

Vervolgens werd de relatieve beweging van het eerste middenhandsbeentje ten opzichte van het trapezium tijdens maximale duimrotatiebeweging onderzocht, waarbij de focus lag op gewrichtscontact (Hoofdstuk 3) en de bewegingsgrens (Hoofdstuk 4). Tijdens één volledige cirkelbeweging vertoonde het duimbasisgewricht bij vrouwen een hogere frequentie van contact en een groter contactratio. Deze bevinding geeft aan dat bij vrouwen in de meeste scenario's een groter deel van het articulaire oppervlak van het duimbasisgewricht constant stress ondervindt, wat kan leiden tot kwetsbaarder kraakbeen. Vanuit een mechanisch perspectief, kan dit de hogere prevalentie van duimbasisartrose bij vrouwen ten opzichte van mannen verklaren. Bovendien heeft de baan van de maximale bereikbare beweging van het duimbasisgewricht een scheef hyperboloïde vorm, waarbij het midden van de vorm zich bevindt aan de kant van het eerste middenhandsbeentje in plaats van aan de kant van het trapezium. De continue meting van één volledige cirkelbeweging biedt nieuwe inzichten voor het ontwerpen van implantaten ter vervanging van het duimbasisgewricht.

De laatste twee hoofdstukken van dit proefschrift breiden het domein van dit onderzoek uit van het skeletstelsel naar het huidstelsel, en wijd uit naar alle vingerkootjes. Een optisch volgsysteem werd gebruikt om de continue rotatiehoeken van specifieke gewrichten gelijktijdig te traceren bij het uitvoeren van verschillende taken (Hoofdstuk 5). De vergelijking van het bewegingsbereik tijdens actieve, functionele en passieve taken (Hoofdstuk 6) onthulde dat het functionele bewegingsbereik het actieve bereik kan overtreffen. Dit was vooral het geval in het distale interfalangeale gewricht tijdens fijne manipulaties. Deze resultaten benadrukken het belang en de rol van deze drie soorten bewegingsbereiken in gewrichten.

Concluderend onderzocht dit proefschrift de botvorm, het gewrichtscontact en de actieve bewegingsgrens van het duimbasisgewricht bij participanten zonder tekenen van gewrichtsdegeneratie. Dit proefschrift vergelijkt ook de gewrichtsbeweging tussen vrouwen en mannen voor de etiologie van duimbasisartrose. De inzichten die zijn verkregen in de structuur en de mechanische werking van het duimbasisgewricht in dit proefschrift kunnen onderzoekers en zorgprofessionals helpen bij het verbeteren en ontwikkelen van effectievere behandelingen voor patiënten met duimbasisartrose. Bovendien biedt de verkenning van de relatie tussen het skelet- en huidsysteem mogelijkheden voor toekomstige onderzoeksperspectieven.

1

INTRODUCTION TO THE THUMB-BASE JOINT

This chapter provides a brief overview of the importance of the thumb in our daily activities and quality of life. It proceeds to discuss the fundamental anatomy of the thumb-base joint (CMC-1) and highlights the prevalence and treatment of CMC-1 osteoarthritis (OA). Subsequently, the research questions are presented, followed by an introduction to the two studies and an outline of the dissertation's structure.

1

1.1. Why Thumb is Important for Us

1.1.1. Thumb usage in activities of daily life

Human thumbs are important for independent activities of daily life [1]. The functionality of the thumb accounts for 40% of the hand functionality [2, 3]. The thumb base joint is a high degree-of-freedom joint that can move in multi-direction for different purposes, e.g., power grasp as holding water bottles, fine manipulation as writing with pens, or communication as performing sign language [3, 1, 4]. Nevertheless, the importance of the thumb is increasing with the growing demand for computer work [5], and the change of lifestyle with smartphones [6, 7, 8].

One special and important movement of the thumb is the opposition. This movement presents the advancement of human beings in tool manipulation and highlights the importance of the thumb finger [3, 4, 9], as many mammals can hardly perform this movement with their thumb [3]. Thus, this motion range during opposition is an important sign for surgeons during clinical diagnosis. Opposition (Fig. 1.2 left) means the movement of the thumb towards or touches the other fingers (index, middle, ring, and pinky finger). This movement is a combination of flexion and adduction. Following the medical definitions, two essential thumb movements for research are 1) **flexion-extension (flx-ext)** (Fig. 1.2 right): the thumb moves toward the palmer direction and the dorsal direction respectively, and 2) **adduction-abduction (add-abd)** (Fig. 1.2 middle): the thumb moves close to the index finger or away from the index finger.

Figure 1.1: Sample of thumb usage in daily activities.
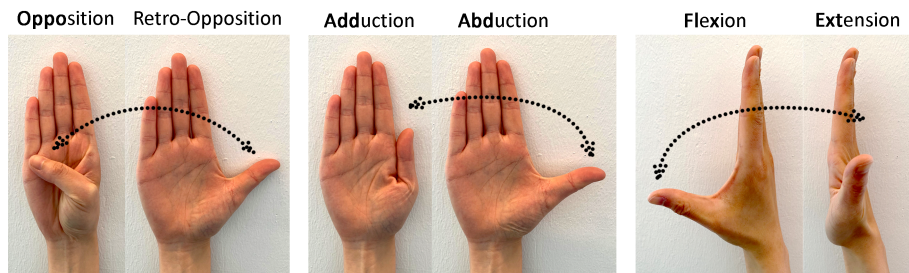
Figure 1.2: The illustrations of the three identical thumb movements.

1.1.2. The anatomy of the thumb-base joint

The base of the thumb is a small carpal bone named trapezium (TPM). This bone is surrounded by the scaphoid, trapezoid, and 1st metacarpal (MC1), which forms three joints. The joint that connects the TPM and MC1 is the thumb-base joint, and it is also named the thumb carpometacarpal (CMC-1) joint or trapeziometacarpal joint (TMCJ). This joint locates on the radial side of the human wrist (see Fig. 1.3). The articulate surface between the TPM and MC1 is a saddle surface. This concave-convex shape enables a large range of motion for flexion-extension, adduction-abduction, and a certain range of self-rotation. Also, it bears a large force transmitted from the tip of the thumb, which can be magnified 2 to 10 times [10, 11]. This exquisite joint is generally connected by multiple ligaments to stabilize the bones during thumb movements and is covered and activated by several layers of tendons and muscles.
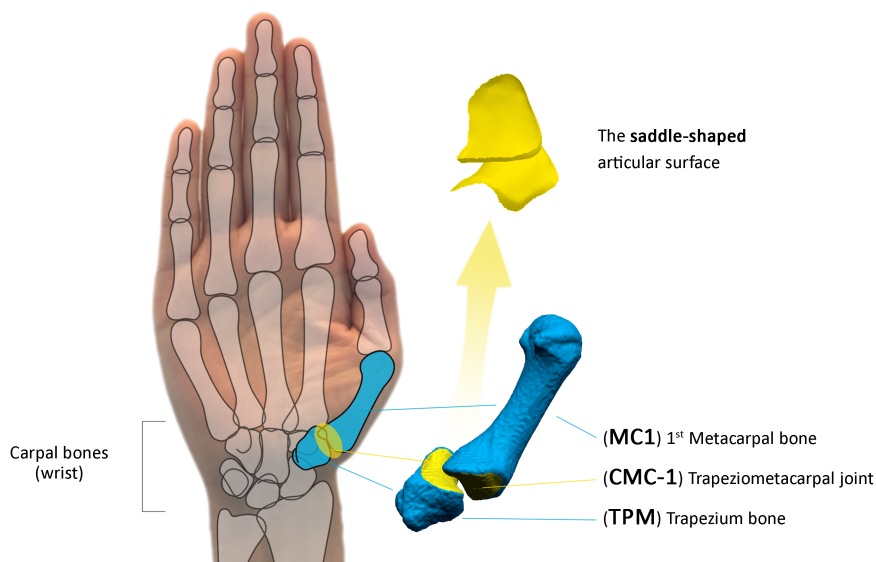
Figure 1.3: The anatomy of the thumb-base joint.

1.2. THE PREVALENCE AND TREATMENTS OF CMC-1 OA

1.2.1. THE MECHANISM OF OSTEOARTHRITIS(OA)

Osteoarthritis (OA) is a disease that leads to irreversible joint damage. Patients with osteoarthritis suffer pain, stiffness, and disability at the affected joint. The soft tissue, e.g., the cartilage on the articulate surface, is worn out and the bones were exposed during joint movements (see Fig. 1.4). Hips, knees, and hands are the most commonly affected sites [12]. Among hand joints, the CMC-1 has a stronger association with hand pain and disability than other joints, which greatly influences the quality of life [13, 14]. Typical symptoms for the CMC-1 OA include pain feeling, weaker grasping, swelling at the base of the thumb, thumb twisted or crooked, and stiff fingers.
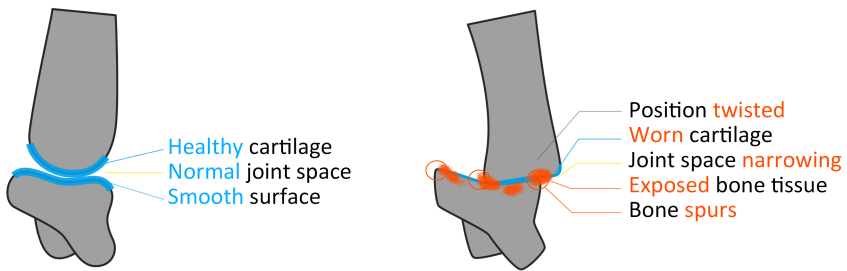
Figure 1.4: The illustration of OA mechanism.

1.2.2. THE PREVALENCE OF CMC-1 OA

The OA at the CMC-1 is a sex- and age-related disease. Population studies have shown that the symptomatic prevalence of CMC-1 OA was around 2% and 7% for females and males over 50 years old [15]. However, the radiographic prevalence of CMC-1 OA raised from 5.8-7.3% to 33.1-39.0% for the 50-year-old and 80-year-old population, especially among females [16]. Around 16-51% of the patients with different stages of joint degeneration may present symptoms as pain [17].

With the change in living habits and the increase in life expectancy, clinical studies have pointed out that CMC-1 OA threatens the young generation (age below 40) who still actively and highly requires the functionality and mobility of the thumb [18]. This can lead to an increasing social burden caused by CMC-1 OA [19].

1.2.3. THE TREATMENT MANAGEMENT FOR CMC-1 OA

With the diagnosis of CMC-1 OA, clinicians usually first suggest conservative treatments, including hand therapy, wearing a hand splint, or intra-articular injection [20, 21]. However, surgical treatments are necessary if the symptom persists and influences daily activities [15]. Options include arthrodesis, osteotomy (currently rarely operated in practical), joint replacement (all known as arthroplasty), trapeziec-

tomy [22, 23]. The remaining bone tissues in these surgeries decrease in sequence as illustrated in Fig. 1.5. The primary goal of these surgical treatments is to remove the pain feeling and enable the mobility and functionality of the thumb.

Arthodesis
Fix the joint by with a plate connects the the two bones.

Joint Replacement
Remove part of the two bones, and implant the replacement.

Trapeziectomy
Remove the whole trapezium bone with/without soft tissue interpolatio to fill the space.
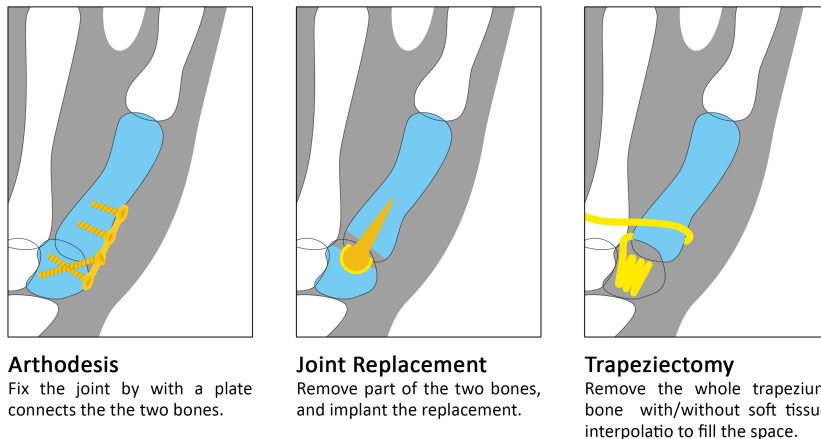
Figure 1.5: The illustration of the three surgical treatments.

Comparing the three surgical options, joint replacement can restore joint mobility while still conserving part of the bones. Other advantages include requiring a short recovery time after the surgery and maintaining the thumb length for appearance [24]. Following the guideline, this surgical option is mostly suggested for patients with Eaton grade II or III OA [25]. Hand surgeons in Belgium and France showed a greater preference for the joint replacement option than hand surgeons in other European countries and the USA [26]. In the Nederlands, the joint replacement for CMC-1 OA is currently the alternative choice for hand surgeons and patients [25, 27]. The treatment decisions are made between surgeons and the patients based on multi-factors, including treatment cost, insurance coverage, as well as outcomes, and the durability of the replacement [15, 26]. Therefore, a superior outcome of the joint replacement is needed when its current cost is higher than the other surgical options.

1.2.4. Joint replacements for CMC-1 OA

Since the first reported total joint replacement (named after the surgeon De la Caffinière) for CMC-1 joint in the early 1970s [28, 29], the ball-socket mechanism (see Fig. 1.5 middle) has been modified and dominating the market [24, 28]. This mechanism is similar to the mechanism applied for hip replacements, and the ball-socket mechanism presents a simplified model of normal anatomical kinematics for the CMC-1 joint.

Today, short-term satisfaction meets requirements with joint replacements, yet optimization is expected to improve long-term outcomes. Implant loosening and

1

dislocation are the two leading causes of revisit or failure [30, 31, 28], where the improvement from the mechanical aspects is needed. A long-lasting implant replacement for CMC-1 for thumb functional activities is demanded, especially for young and active patients [29, 23].

1.2.5. Comparison with the joint replacements for hip and knee

In contrast to the debate on the performance and the cost of the implant replacement for the CMC-1 joint, the treatment with joint replacement is (almost) the standard surgical solution for patients with complaints for knee and hip joints. The product variety and the research resources for big joints (knee and hip) have supported the optimization and improvement of these replacements. Improvements not only include the material strength, movement mechanism, stress analysis, and patient-specific implants (PSI) that relate to the performance of the implant replacements, but also the surgical tools (e.g., surgical robotics, planing systems) that relate to improving the accuracy during the surgery. the research and studies on these big joints have kept enhancing the designs for longer durability, weight-bearing, and functionality.

1.3. Research Motivation and Knowledge Gap

In brief, the following trends underline the research needs on the CMC-1 joint to support a better implant replacement for this joint:

• The CMC-1 joint is essential for basic mobility and functionality in the activities of daily living;

• The change of lifestyles increasingly requires the use of thumb;

• Life expectancy is extended and the more young and active patients with CMC-1 OA are noticed;

• Current in-vivo research is inadequate to support the implant replacement designs for CMC-1.

To support and optimize the implant replacement for CMC-1 joints, an extensive understanding of the anatomy and the biomechanical of the CMC-1 joint are essential as the baseline. However, the understanding of this joint in the in-vivo environment is limited due to the challenges in approaching this small and deep joint. Current knowledge is mainly based on static measurement (e.g., CT, X-ray, MRI) [32, 33, 34, 35]. Dynamic measurements for the CMC-1 joint are still mostly with cadaver studies during passive thumb movement [11, 36, 37, 38]. The performance of the joint during movement with living participants is missing. **The results of this dissertation can enhance medical knowledge for clinical practice, facilitate biomechanical modeling and simulation for the CMC-1 joint, and guide the design optimization and validation for joint replacements.**

1

1.4. RESEARCH QUESTIONS

Based on the above, the main research question (RQ) of this dissertation is: What is the natural state of asymptomatic CMC-1? To answer this, this dissertation studied the average shape and motion pattern for an asymptomatic population with mixed sexes and investigated the following RQs.

- **main RQ:** What is the natural state of asymptomatic CMC-1?

- **RQ-1:** What's the shape variance among asymptomatic CMC-1?

- **RQ-2:** What's the contact pattern between the two bones during the movement?

- **RQ-3:** What's the movement boundary for the asymptomatic CMC-1?

- **RQ-4:** What's the range of motion for finger joints in different scenarios?

1.5. THESIS STRUCTURE

The chapters of this dissertation addressed the research work on the two studies, as the structure in Fig. 1.6:

1) Study: Skeleton System. The in-vivo measurement of the thumb-base joint. (Chapter 2,3,4) This study was approved by the Medisch-Ethische Toetsingscommissie Leiden-Den Haag-Delft (METC-LDD) (NL70432.058.19). In total 54 participants were enrolled with their consent. The 4D CT medical images for both dominant and non-dominant hands were recorded when the participant performed a maximum thumb circumduction movement following the instruction. The data collection was conducted in the Reinier de Graaf Gasthuis.

2) Study: Skin System. The optical measuring system for the finger joints. (Chapter 5,6) This study was approved by the TU Delft Human Ethical Reviewed Board (HERC). Video clips recorded the hand movement with multiple RGB cameras from different angles. In total data of 36 participants were collected with consent. Participants performed a list of hand activities with instructions. The data collection was conducted in the Faculty of Industrial Design Engineering of TU Delft.

Chapter 1 presents a brief anatomy of the CMC-1 joint, introduces the prevalence and the treatment for the CMC-1 OA, summarizes the importance of the thumb finger and the need for a long-lasting joint replacement, as well as underlines the research demands CMC-1 OA.

With the in-vivo dataset, Chapter 2 investigates the bone shape variance among the population (between-subject comparison) and compares the bone shape differences between the dominant and non-dominant hands of each participant (within-subject comparison) for RQ1. Chapter 3 shows the joint contact proximity pattern and recurrency frequency during the maximum circumduction. This chapter focuses on the joint space between the TPM and MC1 and answers RQ2 by comparing the

1

contact pattern for females and males. Chapter 4 connects the static hand postures and traces the boundary motion locus. Additionally, the changes in the arthrokinematics variables during one circle of circumduction were analyzed. The results in this chapter answer the RQ3, which can also provide insights into the replacement designs and support the simulation and the validation for the design and clinical understanding.

Based on the video clips, Chapter 5 proposes an optical tracking system based on the ArUco makers for continuously measuring joint rotation angles. The accuracy and the repeatability of the system were evaluated in detail. Using this system, Chapter 6 measures the range of motion of all finger joints in active, passive, and functional activities. The results of this chapter answer RQ4 and tackle RQ3 from the ergonomic perspective, and this underlines the considerations of the required functional motion range and the anatomical motion range in future splint or implant replacement designs for hands.

Chapter 7 discusses this dissertation in general and concludes the research outcome of this dissertation. Discussions include the reflection on the study design and outcome implications, insights for future studies, and limitations of the two studies in this research work.

1

Chapter 1
Introduction

Study: Skeleton System

Chapter 2
The Shape Variance

Chapter 3
The Contact Pattern

Chapter 4
The Active Boundary

Study: Skin System

Chapter 5
RGB Measuring System

Chapter 6
Ranges of Motion

Chapter 7
Discussion and Conclusion
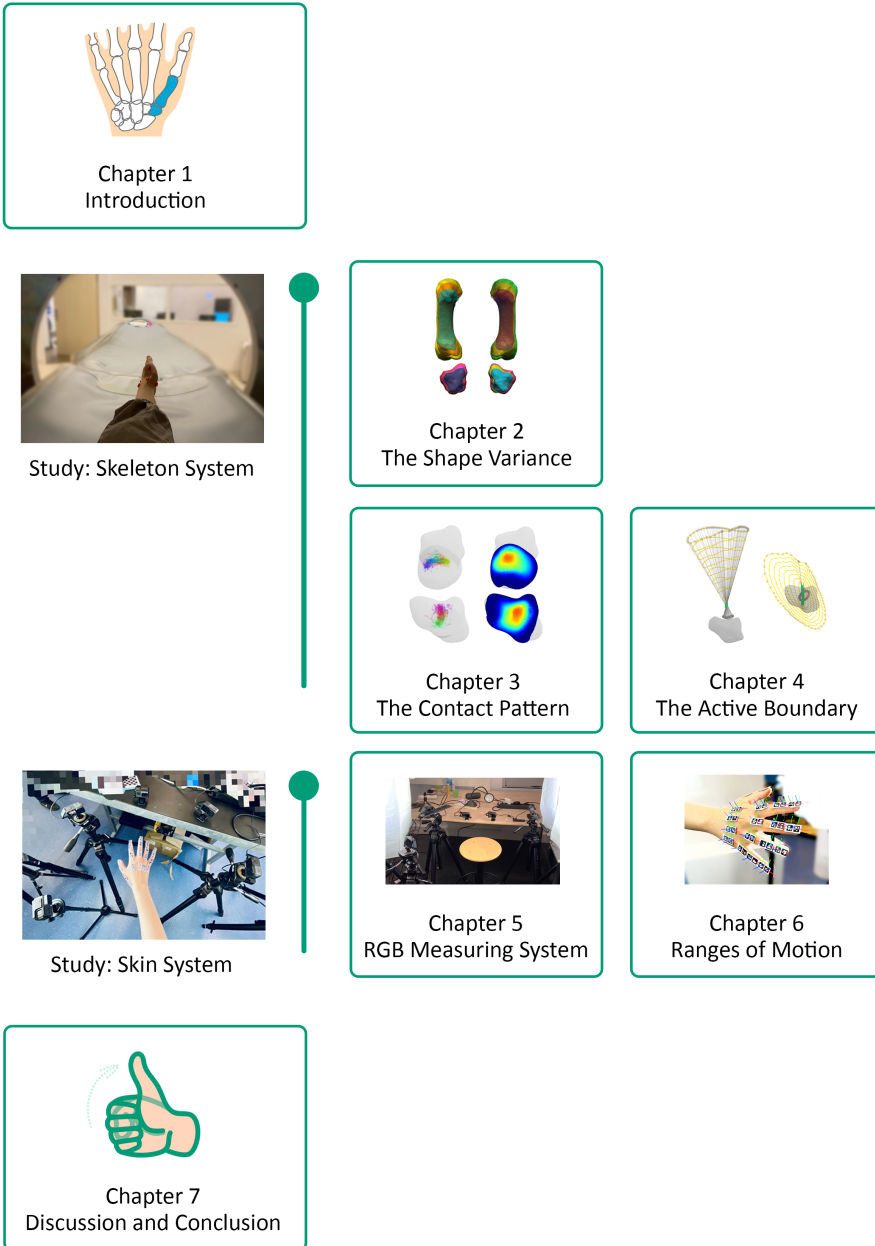
Figure 1.6: The thesis structure.

2

CMC-1 BONE SHAPE

This chapter **assesses the within-subject and between-subject shape variance for trapeziums and 1$^{\text{st}}$ metacarpal bones**. The analysis includes bone models from both dominant and non-dominant hands. The shape analysis indicates that relatively high shape variations are observed around the tubercles and the attachment sites of connective tissues. Another interesting finding is that the bones on the dominant side are slightly but consistently larger than the bones on the non-dominant side. These outcomes imply an association between bone shape variations and the movement of the thumb.

2.1. INTRODUCTION

Thumb carpometacarpal joint (CMC-1) osteoarthritis (OA) is commonly diagnosed among females at ages above 50 years old [39, 40, 16]. Bone morphology is mentioned in the pathology of CMC-1 OA [41, 42], and the prediction of worse osteophytic formation [43]. CMC-1 is a saddle-shaped joint that is essential to the mobility of the thumb in functional activities. Also, this concave-convex shape increases the instability of the joint. For patients who suffer pain and disability with CMC-1 OA, restoring degenerated joints into healthy states in surgical treatment is important. Knowledge of the average bone shape and its variation in the asymptomatic state is helpful, as well as the bone shape of the bilateral asymptomatic side which can provide guidance and reference in surgical planning.

The similarities and differences between the bilateral bones are necessary when one side of the bone is seriously destroyed and requires information from the contralateral side [44, 45]. Existing studies measured shoulder or lower-limb joints, including the humerus, talus, calcaneus, tibia, and fibula, concluded that the bone morphology of the two sides was generally similar [46, 47, 48], thus the geometry of the asymptomatic side can be adopted as the reference or mirrored for the symptomatic side in the treatment. However, Tumer, et. al., pointed out the intra-subject difference of lunate bones, and they suggested that the contralateral lunate was unsatisfactorily for an accurate patient-specific lunate implant [49]. The use of the two hands is less equivalent than the use of the lower limb [2], the comparison between the two sides is worth detailed investigation. Similar to lunates, the trapezium (TPM) and 1st metacarpal bone (MC1) are also small bones that are located in the wrists and are involved in a large range of daily functional activities. Yet, the symmetric assumption for CMC-1 is undetermined.

Knowledge of bone morphology and its variations among the population is valuable to understanding the development of bone degeneration. For example, research on the hip and knee has pointed out that bone shapes can predict the risk level of OA and outcomes of surgical treatments [50, 51, 52]. In comparison, current knowledge on the morphology of CMC-1 seems controversial between observation research and quantitative research. The observation studies indicated the morphological difference among TPM specimens with relatively large sample sizes [43, 53, 54]. These studies assessed TPM specimens, described eleven bone features, and classified the articulate surface into three types: quadrilateral, bean, and heart [43]. Contrarily, the quantitative analyses concluded that the bone shapes of females and males were similar excluding the size factor [55, 56]. Using 3D models from in-vivo data, researchers analyzed the bone volumes [57, 55, 58, 56], the curvature of the articulate surfaces of the two bones [55, 59], the orientation of the local bone coordinates [57], and statistical shape modeling, which suggested the principal bone shape variations was along the principal axis among the population [60, 56]. However, the detailed clinical understanding of shape variations needs improvement.

This study aims to evaluate the bilateral morphological variance within asymptomatic CMC-1 (within-subject comparison), as well as the morphological variance

among the bones of all participants (between-subject comparison). Two methods were implemented in evaluating the shape variance: 1) point-to-point signed distance and 2) statistical shape modeling. The first approach is a straightforward method to understand the general morphological variances, and the second method presents detailed variation modes in space. Data, e.g., bone 3D counter models (including TPM and MC1), grasp and pinch forces, of dominant and non-dominant asymptomatic CMC-1 were collected. Both within- and between-subjects variations among all females, males, and mixed sexes were displayed. The finding regarding the extent of bone morphology of participants can be valuable to the anatomy understanding of CMC-1 for future patient-specific implant design and also benefits for etiology research and clinical diagnosis.

2.2. METHOD

2.2.1. PARTICIPANTS AND DATA ACQUISITION

Approved by the local medical ethical committee, 54 participants were enrolled with no history of hand surgery, injury, or discomfort. After signing the informed consents, both of their hands received CT scans (Canon Aquilion ONE 320-slice, tube voltage 80kV, slice thickness 0.5mm, FOV 180mm, and resolution 512x512 with increment of 0.25mm, maximum 0.06 mSv per scan). Screened by the researcher and the hand surgeon, data of three participants were excluded due to mid-position in the CT scanning or the presence of Eaton I degeneration; the remaining 51 bilateral asymptomatic MC1 and TPM were included. The average age of the included participants was 35.1 (± 11.1). Besides the CT data, we collected information on the participants: gender, ethnicity, age, hand dominancy, grasp force, and pinch force. The grasping force and pinch force were measured using a dynamometer and a pinch gauge, respectively. Participants were instructed to produce maximum grasp and pinch force three times, and the mean of the three measurements was recorded.

2.2.2. DATA PROCESSING

A proper point correspondence among the dataset is often a prerequisite for shape analysis (Heimann and Meinzer, 2009). For this, all collected CT images were first segmented using Philips IntelliSpace Portal (Amsterdam, Netherlands). With Geomagic Design X (Geomagic Inc., Morrisville, NC, USA), we post-processed the segmented 3D models by keeping the continuous outer contour of the two target bones: the TPM and MC1. Left-side models were mirrored along the sagittal plane. A reference model was selected among the bone models in the dataset, then, all models were coarsely aligned to this reference model using the iterative closest points rigid registration method. Point-level correspondences among 3D models were constructed by using Wrap (R3DS, 2020.08.7). After this, all models were scaled to the average size, and the alignment was adjusted using generalized Procrustes alignment, followed by a final computation of the global mean model. The processing procedure is illustrated in Fig. 2.1. The analysis was executed with a self-developed Python

program (version 3.7) based on the Trimesh library (Version 3.15.3).
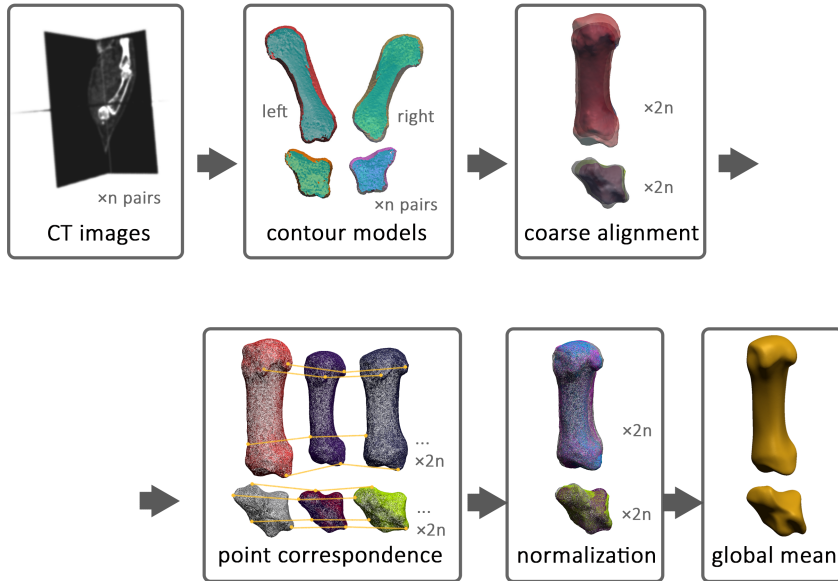
Figure 2.1: The workflow to establish point correspondence from medical images.

2.2.3. POINT-TO-POINT SIGNED DISTANCE (METHOD 1)

Based on the constructed point correspondence, the point-to-point signed distance of the vertices for the normalized models was conducted for morphology variation analysis. For **within-subject** shape variance in the paired sets, models of the dominant side were first aligned to the corresponding models of the non-dominant side; then the distances from the vertices of the non-dominant-side model to the corresponding vertices of the dominant-side model were calculated. If the vertex was inside the contour of the dominant-side model, the distance was in negative value; the positive distance meant the vertex was outside the dominant-side model. For **between-subject** shape variation, all models were normalized to the global mean model, followed by the distance analysis for all bones of the dominant side and non-dominant side respectively. Similarly, the positive and negative distance meant that the vertex was outside or inside the mean model. After these, the standard deviations of the signed distances were computed; the regions with larger deviations suggested higher shape variance among the population.

Taking the paired nature of data into account, the shape symmetry between the dominant and non-dominant sides was analyzed first, followed by evaluating the morphology variation among the participants. In symmetric analysis, matched sample test and intra-class correlation (ICC) analysis were conducted to measure the within-subject difference in the list of quantitative parameters. Shapiro-Wilk test re-

sults indicated that the differences were not normally distributed, therefore Wilcoxon signed-rank test was used to identify the within-subject differences of these parameters (effect size=0.6, power=0.95). The ICC analysis, which used a single measurement, absolute agreement, and two-way random effects model was applied to assess the relationship of the within-subject difference and the between-subjects difference.

2.2.4. STATISTICAL SHAPE MODELING (METHOD 2)

The between-subject comparison was conducted using statistical shape modeling (SSM) in addition to the straightforward distance analysis. The SSM has the advantage of describing the 3D shape variations directions in detail. Two Statistical Shape Models (SSMs) for TPM (SSM-TPM) and for MC1 (SSM-MC1) were built based on the wrapped models. Correspondingly, the variation modes of the two SSMs, e.g., T1, T2, … for SSM-TPM, and M1, M2, … for SSM-MC1, were named in descending orders regarding the variance explained by each of them. The weights of the modes for each input model, which resemble the amount of deviation from the mean shape of the corresponding mode, were acquired and used in the analysis. Then, any TPM or the MC1 can be represented using the eq. 2.1

$$Model_{TPM} = Mean_{TPM} + \sum_{i=1,2,3,...} \alpha_i Ti$$
$$Model_{MC1} = Mean_{MC1} + \sum_{i=1,2,3,...} \beta_i Mi$$

$$(2.1)$$

where the $Model_{TPM}$ and $Model_{MC1}$ means any TPM and MC1 bone model; the $Mean_{TPM}$ and $Mean_{MC1}$ represents the mean model of the collected dataset for the two bones; α_i and β_i refers to the coefficient for the corresponding principal variation modes T_i for SSM-TPM and M_i for SSM-MC1; i are ordered according to the variation ration suggested by the PCA model (e.g. as indicated in Fig. 2.8).

To interpret the shape variations indicated by an SSM, we evaluated the principal variation modes which account for more than 5% of the total variance [61]. Besides observation and description, we underlined the area that presents the most 25% deviation of each selected mode, named the highly-deviated area. Also, these selected modes were adopted in statistical analysis. The cross-validation of the SSMs was based on root-mean-squared (RMS) error which was calculated with principal modes whose cumulative explained variance reaches 90% of the total variance.

2.2.5. STATISTICAL ANALYSIS ON MEASURED PARAMETERS

With the grasping force, the pinch force, and the parameters extracted from the models in real size, as Fig. 2.2, a list of quantitative parameters was included in the within-subject analysis. The list includes parameters based on measured information: grasp force, pinch force, hand length, wrist breadth, measured MC1 length, thumb breadth, aspect ratio between hand length and wrist breadth, and aspect ratio between MC1 length and thumb breadth. The extracted measures from the bone models in the original states were: the bone volume, the dimensions along principal inertial axes, the aspect ratio between the length and the diagonal length of the two short sides of

the minimum bounding box, the area of the articulate surface, and the two principal curvatures of the articulate surface, and the primary principal modes of two SSMs.
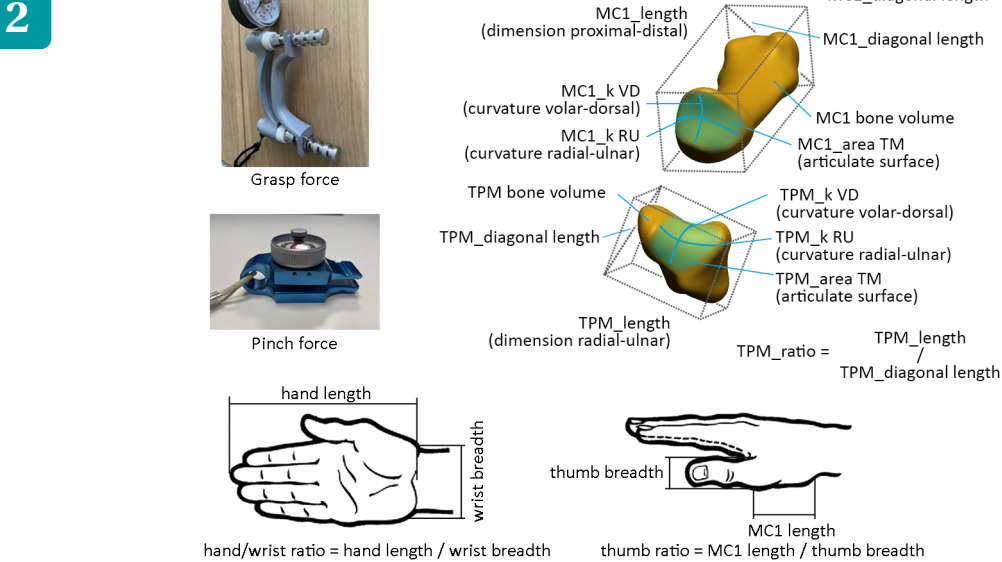
Figure 2.2: The illustration of parameters extracted from bone models and anthropometry measurements from hands.

2.3. Results

2.3.1. Demography results

The analysis included bilateral data from 51 asymptomatic participants. The dataset covered: 48 right-handed and 3 left-handed; 28 females and 23 males; 26 Europeans, 24 Asians, and one from Latin America.

2.3.2. Dimensions of the global mean models

The mean models of the target bones among the 102 datasets were computed. The bone volumes were 1686.3 mm3 for the TPM and 4515.4 mm3 for the MC1, and the dimension of the bounding box along the principal inertia axes (in sequence: ulnar-radial direction, volar-dorsal direction, proximal-distal direction) was 19.68×15.0×12.9 mm for a TPM and 14.9×15.1×46.1 mm for the MC1.

2.3.3. Symmetric comparison in real size

From the symmetric analysis based on the parameters measured in real size, we noticed that the grasp force of the dominant hands was larger than that of the non-

dominant hands, while the pinch forces produced by the two hands were compara-ble. The bone volumes of TPM and MC1 on the dominant sides were imperceptibly larger than those of the non-dominant side. A similar phenomenon was also ob-served for the area of the articulate surface of the two bones, and the dimensions along the principal inertia axes of the MC1. Meanwhile, the ICC analysis suggested low correlations between the within- and between-subjects differences. Details of the comparisons on the mean values are listed in Table 2.1.

Table 2.1: The mean and the statistical test results of the symmetric comparison Note: domi: dominant side; nond: non-dominant side; TM area: trapezium-metacarpal articulate surface area; k: curvature; dim: dimension; VD: volar-dorsal; RU: radial-ulnar; PD: proximal-distal.

Metrics	Mix	Domi	Nond	Domi – nond	P-val (W)	ICC	95% CI
Grasp force (kgF)	34.34 (±10.95)	35.35 (±11.33)	33.34 (±10.46)	2.01 (±4.66)	0.001	0.895	0.8-0.94
Pinch force (LBS)	19.26 (±5.05)	19.53 (±4.90)	18.99 (±5.18)	0.54 (±2.75)	0.437	0.849	0.75-0.91
MC1_volume (mm3)	4637.13 (±1340.17)	4719.93 (±1342.88)	4554.33 (±1332.32)	165.60 (±168.99)	<0.001	0.985	0.89-0.99
MC1_TM area (mm^2)	126.45 (±25.18)	128.04 (±24.82)	124.85 (±25.45)	3.19 (±3.39)	<0.001	0.983	0.89-0.99
MC1_k VD (mm^{-1})	118.76 (±28.76)	113.81 (±27.05)	123.71 (±29.56)	-9.90 (±26.21)	0.013	0.544	0.31-0.71
MC1_k RU (mm^{-1})	-121.05 (±30.86)	-122.90 (±30.58)	-119.20 (±31.02)	-3.70 (±23.84)	0.303	0.7	0.53-0.82
MC1_dim RU (mm)	14.90 (±1.44)	14.99 (±1.45)	14.81 (±1.43)	0.19 (±0.30)	<0.001	0.971	0.92-0.99
MC1_dim VD (mm)	15.39 (±1.44)	15.47 (±1.41)	15.31 (±1.47)	0.16 (±0.35)	0.005	0.965	0.93-0.98
MC1_dim PD (mm)	46.21 (±4.59)	46.42 (±4.58)	46.00 (±4.60)	0.42 (±0.68)	<0.001	0.985	0.96-0.99

2.3.4. WITHIN-SUBJECT COMPARISON IN NORMALIZED SCALE

The distance deviations of the symmetric analysis within the 51 pairs (mixed female and males) of TPM and MC1 suggested that normalized bones of non-dominant sides deviated from the dominant side in a range of -2.22—1.50 mm and -2.56—1.76 mm respectively, and the standard deviation of this signed distance were 0.20—0.51 mm for TPM and 0.22—0.71 mm for MC1, as presented in Fig. 2.3. Relative larger de-viations were found in regions around the trapezial ridge, edge of scaphoid-trapezium surface, palmar tubercle, and the dorsal-radial tubercle of TPM; the sesamoid tuber-cles, the hook of the trapezium-metacarpal articulate surface, and the radial border of the epiphysis of the MC1. The bone shaft and the center of the articulate surface of the MC1 presented relatively lower deviation in the dataset.

2.3.5. BETWEEN-SUBJECTS COMPARISON IN NORMALIZED SCALE

The signed distance among all normalized bone models was compared with the global mean. The average distance difference ranged between -2.69—1.86 mm for TPM and
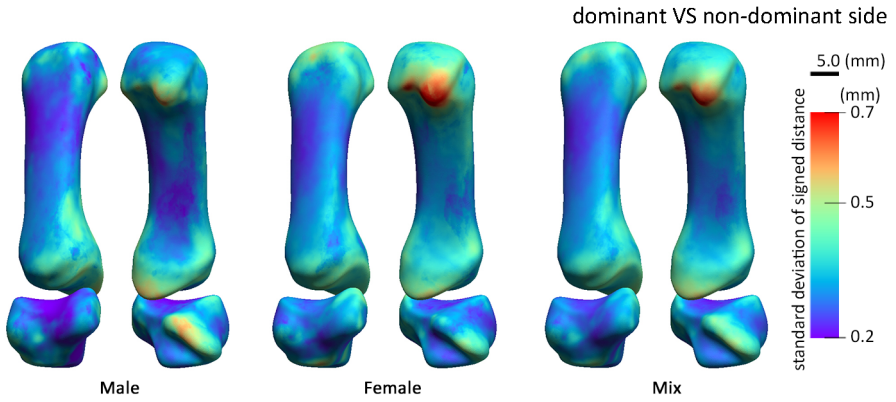
Figure 2.3: The shape variations of within-subject comparison. Color means the value of the standard deviation of signed-distance analysis.
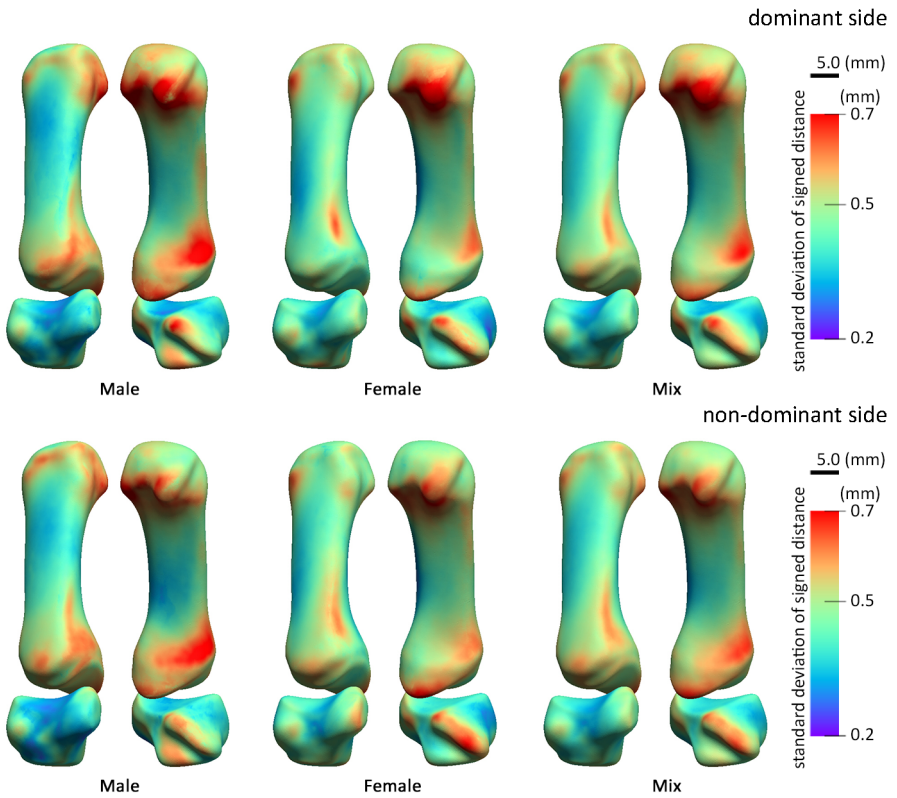
Figure 2.4: The shape variation of between-subjects comparison for dominant and non-dominant sides respectively. Color means the value of the standard deviation of signed-distance analysis.

-2.77—2.35 mm for MC1 on the dominant side, -2.02—1.66 mm and -1.96—1.68 mm for TPM and MC1 on the non-dominant side. The standard deviation for all dominant TPM was 0.32—0.77 mm and the ones for all dominant MC1 was 0.35—1.00 mm; respectively the ones for all non-dominant bones were 0.33—0.75 mm and 0.33—0.81 mm. Figure 2.4 shows the distribution of the standard deviation of the vertices over the bone models, where the highly-deviated areas were close to the tubercles or the attachment sites of connective tissues, e.g., trapezial ridge, palmar tubercle, the dorsal-radial tubercle, and ulnar lip for TPMs, and the sesamoid tubercles, the hook of the MC1, radial and ulnar side of the bone shaft, especially around the epiphysis, for the MC1.

2.3.6. THE SSMS AND THE INTERPRETATION OF TPM AND MC1

Using the bone models that scaled to the mean size, the SSMs for the two bones were constructed respectively. Fig. 2.5 presents the cumulative variance modes for the two SSMs. The first 20 principal variation modes of SSM-TPM and the first 14 principal variation modes of SSM-MC1 accounted for over 90% of the total shape variance. Using these modes, cross-validation suggested 0.2 mm and 0.24 mm RMS errors for the two SSMs respectively.
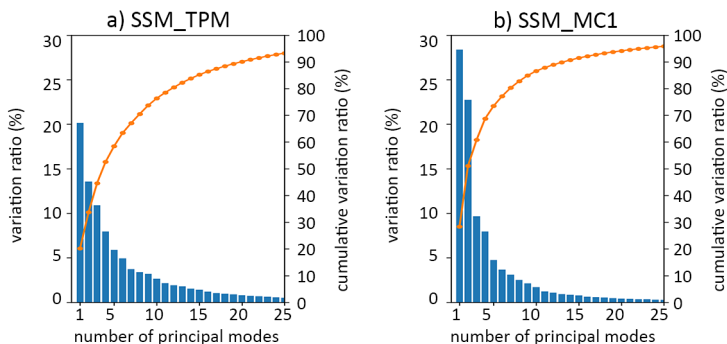
Figure 2.5: The ratio of the variation modes and the cumulative explained variance for SSM-TPM (left) and SSM-MC1 (right).

The first five modes of SSM-TPM and the first four modes of SSM-MC1 were selected, as each mode accounted for more than 5% of total shape variations. Respectively, their accumulated variances reached 58% and 68.7% of the total variance. The highly-deviated area and the deformation with -3SD and +3SD of each principal mode were presented in Fig. 2.6. Compared with the anatomy study on the TMC ligaments [62, 63], excluding the trapezium-trapezoid surface in mode T2, the majority of the highly-deviated area in both SSMs were in close proximity to the tuberosity or tubercle, where the connective tissue attaches. Moreover, the pairwise distance deviation analysis suggested similar results, as presented in Fig. 2.8. The deviation among the vertices on the size-normalized bone models was 0.4-0.77 mm for TPM and 0.67-1.07 mm for MC1.

(a) SSM principal modes for TPM   (b) SSM principal modes for MC1
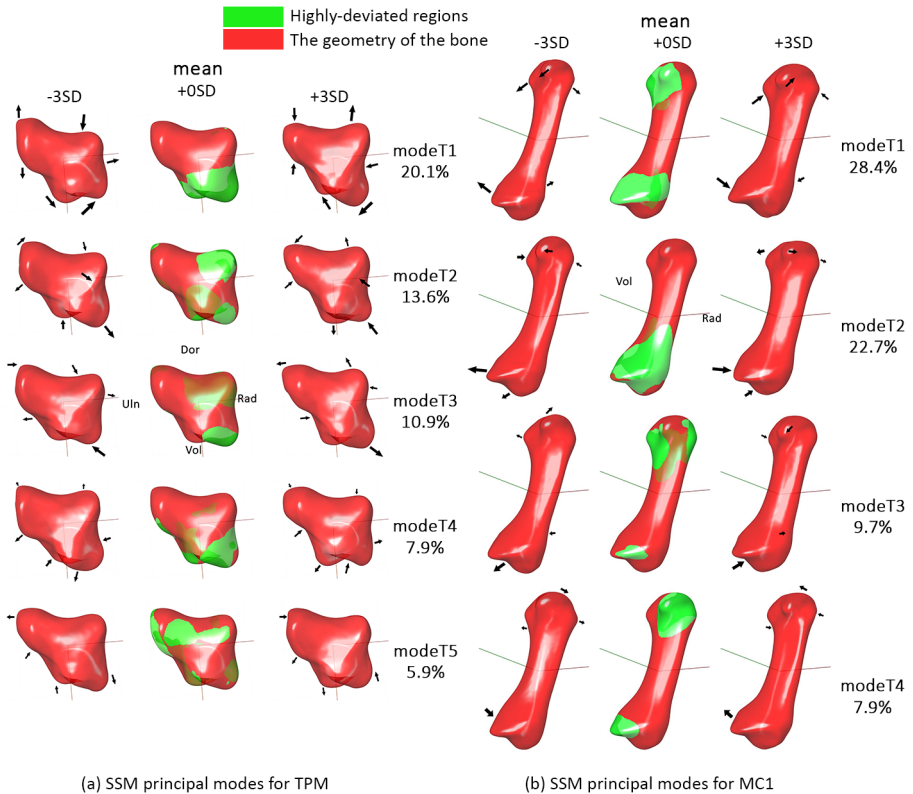
Figure 2.6: The deviation flow and the high-deviated area (green) of selected principle variation modes of SSM-TPM (a) and SSM-MC1 (b). Dor: dorsal side; Vol: volar side; Rad: radial side; Uln: ulnar side.

2.3.7. CORRELATION AMONG QUANTITATIVE PARAMETERS

The included quantitative parameters were classified into three categories: 1) force: the grasp and pinch force; 2) size: metrics related to bone volume, length, and width; 3) shape: here includes the aspect ratios of hands and bones, the curvature of the articulate surface, and the weights of selected modes (first 5 for SSM-TPM, and first 4 for SSM-MC1).

At the top left of Fig. 2.7, most size parameters suggest considerably high correlations with each other. Excluding the length of MC1, the relatively high correlations with force parameters and bone size indicate people with larger hands can produce greater grasp and pinch force; however, the length of MC1 is a poor predictor of force. Size parameters also show moderate correlations with the maximum curvature of the TMC articulate surface of the MC1 bone and the minimum curvature of the TPM bone. The minimum curvature of the TPM side and the maximum one of the MC1 side are correlated with each other, and these two principle curvatures are approximately along the ulnar-radial direction [55, 59]. With the focus on shape parameters,

participants with longer MC1 bones (measured data) seem to have a larger aspect ratio of thumb, and those with wider wrist breadth have relatively shorter hands on average. In addition, mode M1 is highly positively correlated with the aspect ratio of the MC1 bone. Four of the five variation modes of SSM-TPM present weak relationships with the aspect ratio of TPM.
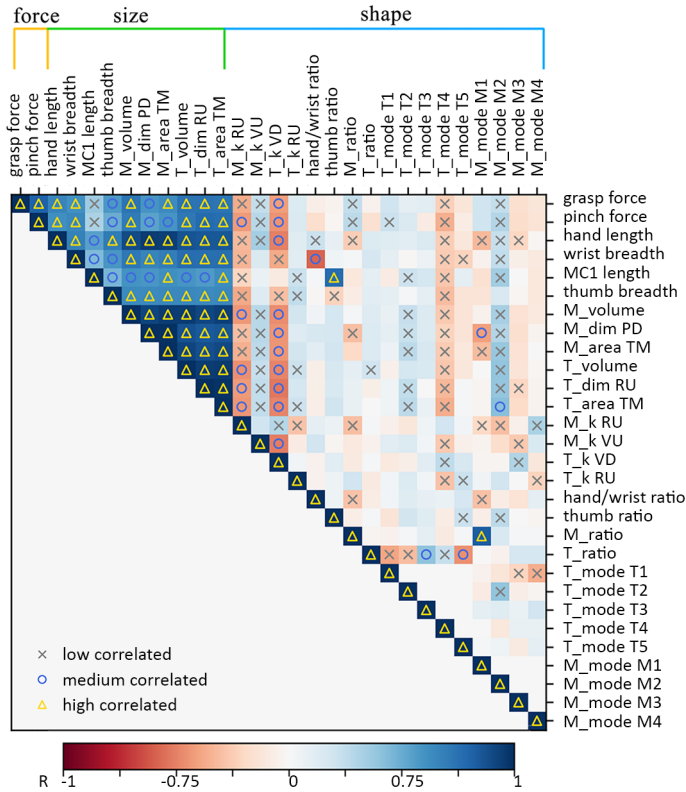
Figure 2.7: Heatmap of the correlation among quantitative parameters.

2.4. DISCUSSION

The goal of this study is to understand both within-subject and between-subject shape variations of trapeziums (TPM) and 1st metacarpals (MC1). Bilateral CT data of asymptomatic participants were included. We evaluated the bone symmetric and the shape variance among the database based on dimensional parameters extracted from 3D bone models. The pair-matched statistical analyzed the measurements in original-sized models and 3D shape analysis (pairwise signed distance analysis and statistical shape modeling (SSM) analysis) excluded the bone size influence by evaluating the bone models that normalized to the average size.

2

2.4.1. SLIGHT BUT CONSISTENT DIFFERENCE IN WITHIN-SUBJECT COMPARISON

The symmetric analysis suggested a size difference between the paired bones. The volume of the dominant side is consistently larger than that of the non-dominant sides, although the difference was about 1% to 3% of the average bone volume, which was incomparable with the between-subjects difference. Similar results were observed for side-dependent parameters, e.g., articulate surface areas and the dimensions of the MC1, etc.

Considering the within-subject analysis based on normalized models, similar to the between-subjects variance, the tubercle features presented relatively higher deviation than other regions. The deviation approximates the palmar tubercle, dorsal-radial tubercle, and the articulate surface might explain the principal curvature difference between the two sides. The shape deviation between the most vertices on the paired bones was below 0.45 mm, and the average edge length of the meshes of the mean models was 0.23 mm. The measured symmetric shape deviation in this study was comparable with the standard deviation measured in studies on lower limbs: approx. 0.43-0.88 mm [46, 47, 48], and slightly larger than the one standard deviations of lunate: 0.3 mm [49]. However, the talus, fibula, tibia, and calcaneus are much larger than the wrist bones. Small morphological variations in wrist bones may account for larger shape deviation thus affecting the biomechanics of the joints.

2.4.2. BETWEEN-SUBJECTS VARIANCE AND LIGAMENT ATTACHMENT SITES

The maximum deviations in the pairwise distance analysis were close to the mean thickness of cartilage which was 0.7 and 0.8 mm for the two bones [64]. For normalized bone models to the global mean model, the maximum deviation was 0.8 and 1.0 mm for TPM and MC1 among mixed-side models. The shape variation pattern in the study was in accordance with the results of previous morphology studies where one study of the statistical shape models indicated that the tubercle features mainly led to bone shape variations [56]; another study measured the distance from the estimated model with 3 times SD to the mean model, and the maximum deviation was around 1.40 mm and 1.87 mm for TPM and MC1 [60]. Our analysis suggested that features mentioned in an observation study: the ulnar-dorsal, radial-dorsal edges, ulnar-volar, and radial-volar joint line [43], deviated relatively prominently among individuals and within individuals. Knowledge of the shape variation can be beneficial for future implant design, e.g. fixation design, or the cup design, especially when the patient-specific implant has demonstrated a superior advantage in some joints [65, 44].

The between-subjects comparison, that analyzed by both the pairwise distance approach and SSM method, indicated that the shape variance around the tuberosities or tubercles was higher than the articulate surface between TPM and the MC1. These highly deviated areas were approximately where the connective tissue attaches [62, 63, 66]. Compared with the Fig. 2.3 and Fig. 2.4 to the features illustrated in Fig. 2.8, the regions with large shape variance of trapezium are around the attachment

sites of the transverse carpal ligament (TCL), the ligament between volar trapezium to second/third metacarpal (VT-MC), dorsal radial ligament (DRL), volar trapezio-trapezoid ligament (VTT), and volar scaphotrapezial ligament (VST). Most of these ligaments tighten with supination and extension [62]. For MC1, most shape deviation presented at an area around the epiphysis and metaphysis of the bone, which, respectively, relates to the attachment site of the volar plate, the ulnar and radial collateral ligament (UCL, RCL), and volar beak (AOL). Additionally, areas of proximal-radial and -ulnar border of the shaft were also relatively highly deviated, and they enclose where the abductor pollicis longus (APL) and intermetacarpal ligament (IML) attach. Among these ligaments, the AOL and IML are important in resisting pronation [62, 66].
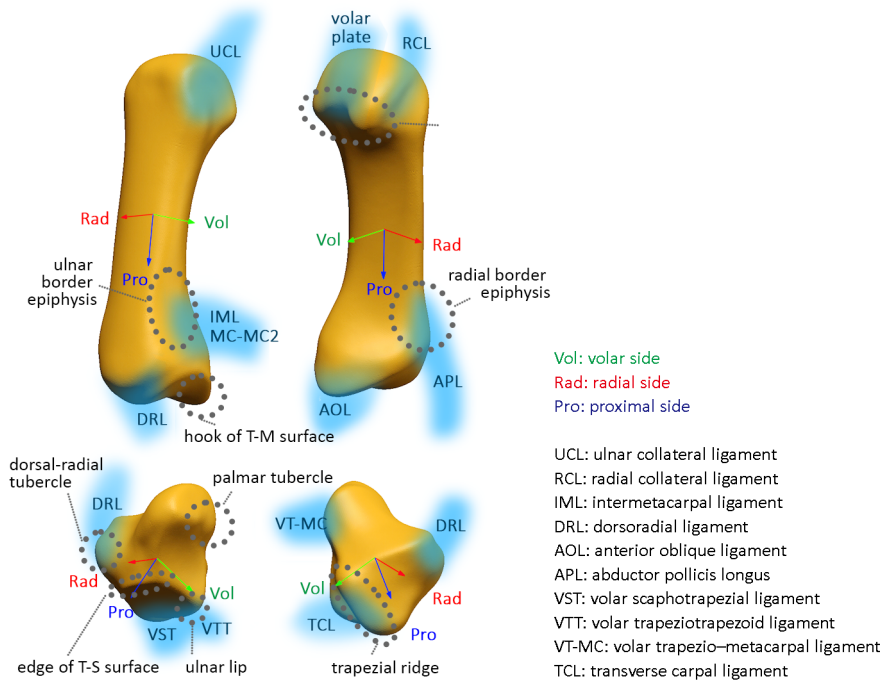
Figure 2.8: Illustration of the association between highly deviated area and related connective tissues. Vol: volar; Pro: proximal; Rad: radial; TCL: transverse carpal ligament; VT-MC: ligament between volar trapezium to second/third metacarpal; DRL: dorsal radial ligament; CTT: volar trapeziotrapezoid ligament; VST: volar scaphotrapezial ligament; UCL: ulnar collateral ligament; RCL: radial collateral ligament; AOL: anterior oblique ligament; IML: intermetacarpal ligament; APL: abductor pollicis longus.

2.4.3. THE ASSOCIATION WITH HAND USE

The general between-subjects deviation patterns for dominant and non-dominant bones were similar, still, Fig. 2.4 presents apparent differences between the two sides for both sexes and mixed sex, e.g., around the trapezial ridge, volar side of

the epiphysis, and the radial sesamoid tubercle. The morphological difference between the two sides and among the population can reveal potential association with thumb usage, including loading and the movement of dominant and non-dominant thumbs in daily activities; for instance, the focused area with shape variation over 0.5 mm seemed smaller for the dominant side, yet the maximum variation value of dominant side was larger than that of non-dominant side. Also, the variation around ulnar border epiphysis was greater for males, and the trapezial ridge of females presents a larger difference. Previous studies tracked the hand usage of participants in daily activities and indicated that humans tended to use two hands in different tasks: dominant hands for precision tasks and non-dominant hands for powerful tasks [67, 68, 69]. Human biology research concluded that bone shapes were affected by mechanical load and joint movements [70]. Research on spines and hips also concluded that movement can affect bone shapes [71, 72]. These may explain the greater morphological deviation of asymptomatic bones at the attachment sites of connective tissue than the articulate surface between the bones. Measuring hand usage or investigating the relationship between bone morphology and the range of motion of the joint can be helpful in understanding the morphology variation and deformation in the degeneration process. The understanding of shape variation may be beneficial and need to be considered in future research on the biomechanics of the ligament for CMC-1, e.g., the directions of the applied forces and movements.

2.4.4. LIMITATION

In this study, we focused on the morphological variations within individuals and among the population. However, the effect of shape variation in a healthy state on potential degeneration was unclear since the longitude information was currently unknown. Another limitation is that the analyses of both the TPM and MC1 were in isolation of surrounding bones and joints. The edge of the scaphoid-trapezium articulate surface demonstrated a relatively noticeable variance for both within- and between-subject (s) distance analysis; however, the shape and the relative positions of the scaphoid were excluded. Moreover, the insufficient information on connective tissue was an additional limitation. Using CT data, along with corresponding images e.g., MRI, to detect ligaments, can better support and possibly validate the connections between shape variations and ligament attachment sites. Since we suggested this potential association, future works will also consider the relationships between joint movements and bone shapes.

3

CMC-1 JOINT CONTACT

This chapter studies the movement of the CMC-1 joint by **evaluating its joint contact and comparing the pattern for females and males**. A motion smoothing method is implemented by interpolating a NURBS curve constructed with kinematic variables. The comparison suggests that the CMC-1 joint for females exhibits a larger contact ratio (contact area of one frame/contact area of the full motion) and higher contact recurrent frequency. This explains the higher prevalence of CMC-1 OA among females, as their articulate surface can be more vulnerable due to a larger portion of it being under constant stress.

3.1. INTRODUCTION

The thumb carpometacarpal joint (CMC-1) is a common site of osteoarthritis (OA). Population studies have shown that the CMC-1 OA ranged from 5.8—7.3% to 33.1—39.0% for the population in 50- and 80-year-old, especially higher among females [16, 12, 73]. However, the etiology and pathology of CMC-1 OA remain unclear. Many risk factors have been suggested, including inherent factors such as advanced age, female gender, congenital joint malformation, and genetic predisposition [16, 12, 73]. Other factors include acquired or environmental factors such as medical conditions, acute trauma, or long-term low-level stress [73, 74, 75]. Of these many factors, smaller bone size for females is one of the mechanical factors that explain the higher prevalence of CMC-1 OA among females [56]. The CMC-1 is essential for independent daily activities. The companied pain and stiffness along with the joint degeneration can eventually cause functional loss of hand movement [76, 13]. The contribution of the joint contact in the thumb during dynamic movements to joint degeneration is unclear, and such difference between females and males remains unknown.

Improving our understanding of the asymptomatic movement based on dynamic measurement is essential to deepen the knowledge of joint arthrokinematics and dynamic instability. Tteshiahis knowledge will in turn lead to developing better interventions to restore a healthy joint state. In other joints like the hip and knee, research outcomes of the proximity pattern, the migration of contact centers, and stress distribution patterns of joint articulate surfaces during movements of healthy volunteers and patients have all supported clinical understanding and improved treatment designs [77, 78, 79, 80]. However, measurements for the CMC-1 joint mostly are based on cadaver studies [36, 37, 38, 11] or on discrete static CT scanning at selected positions [81, 33, 82], and the resulting continuously dynamic information for asymptomatic participants is unclear. Key static positions at extreme motion range, e.g., flexion, extension, adduction, abduction, and opposition, or three functional tasks with extreme force, e.g., key pinch, jar twist, and grasp, were investigated [37, 81, 33, 83, 84]. Limited studies have evaluated the CMC-1 joint using in-vivo dynamic measurements, e.g., 4D CT scanning [83, 85]. Knowledge of the contact of the bone articulate surfaces with spatiotemporal relations benefits understanding the mechanical factors of cartilage damage and OA pathogenesis.

In this study, we collected the in-vivo 4D CT scans of asymptomatic participants after they performed a maximal reachable circumduction. The circumduction includes and connects the opposition, extreme flexion, extension, adduction, and abduction while allowing natural movements without intervention [83, 86, 87]. Based on the collected frames, we screened and augmented additional frames representing the maximum circumduction for analysis. The primary goal of our study was to investigate joint contact of asymptomatic CMC1 with spatiotemporal relations and compare the patterns for females and males in the thumb circumduction. Metrics included: contact recurrency, contact ratio, and the migration of the contact center. The outcomes of this study will provide insights into the cause of the etiology and degeneration cases, and lead to possible interventions for CMC-1 OA in the future.

3.2. Method

3.2.1. Participants and data acquisition

Following medical protocol approval, we enrolled participants who indicated no history of hand injury or discomfort. All participants were informed of the study goal and offered their written consent. A hand surgeon conducted a pre-screening. The participants were then instructed to perform a maximum reachable circumduction with the thumb of their dominant hand. The movement followed the sequence: adduction-flexion-opposition-adduction-extension-adduction (Figu.3.1). A pre-recorded video with the designed motion was displayed to instruct the participants on the approximate positions and to align their movement speeds (12 seconds per circle) during the practice and scanning. In total, 47 4D CT scans from 24 females and 23 males with a mean age of 34.3 ±9.8 (range: 19–57 years old) were acquired. Based on the medical images, a hand surgeon confirmed that all included data showed no evidence of bone degeneration.

3.2.2. Data processing

The 3D models of the 1st metacarpal (MC1) and trapezium (TPM) from the scans of each participant were constructed using the Philips IntelliSpace Portal (Amsterdam, Netherlands), resulting in 47 pairs of high-quality MC1 and TPM models. Then, for each dataset, the bone models were post-processed with Geomagic Design X (Geomagic Inc., Morrisville, NC, USA). The point correspondence among models from all datasets was established using Wrap (R3DS, version 2020.08.7), thus all MC1/TPM models had the same number of vertices and topology. The relative translation and the rotation of the MC1 to the paired TPM were then extracted with a self-developed Python program (version 3.6) (see Chapter 4). Among all collected frames of the motion, the frames with key positions: flexion, extension, adduction, abduction, and opposition of each participant were selected and agreed upon by three researchers. The key frame selection followed the image contours of the palm and thumb based on either transverse view or frontal view, as illustrated in the bottom row of Fig. 3.1. The definitions are detailed in Table 3.1

Table 3.1: Descriptions of the key positions for frame selection.

Positions	Description
Flexion	The thumb tip points most away from the palm, or the thumb is approximately perpendicular to the palm.
Extension	The thumb most towards the back of the hand.
Adduction	The thumb is attached to the index finger.
Abduction	The thumb is in the palm plane and points most away from it.
Opposition	The tip of thumb closest to the proximal end of the pinky finger.
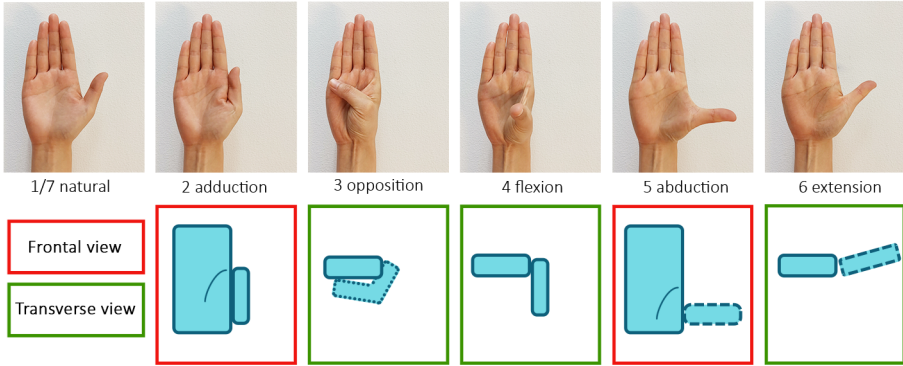
Figure 3.1: Key positions of the circumduction for instruction. The upper row shows the definition of the key positions from visualization, and the bottom row illustrates the definition based on the views of medical images.

3.2.3. MOTION INTERPOLATION

A 4D CT dataset consisting of 45 to 50 frames was collected in the full circumduction for each participant. However, the collected movements were often unevenly distributed due to the physical constraints of each participant. To analyze the motion among participants, we rearranged the collected frames and interpolated the motion based on the spatiotemporal information. Specifically, the interpolation took two steps. The first step was to identify the frames with larger rotations in all directions, as rotation is a size-independent variable. The longitudinal axis (unit length) of the MP1 was orthogonally projected on the transverse plane of the TPM (Fig. 3.2 left). Then, the frames with the projected points that were connected by the alpha shape ($\alpha = 2$) were retained, and frames with projected points inside this polygon were excluded (Fig. 3.2 right). The second step was to smooth and augment the retained frames. Using translation (tx,ty,tz along the three axes) and rotation (the Euler angles ez,ex,ey extracted based on the Z-X-Y sequence, corresponding to flexion-extension, adduction-abduction, and self-rotation), a B-Spline was implemented to evenly discretize the boundary movement into 100 frames (positions); see the pink lines in Fig. 3.3. The sequence of these augmented frames was then further adjusted in a clockwise direction, starting from the orientation of the axis pointing most dorsal direction.

3.2.4. MEASUREMENT METRICS OF JOINT CONTACT

In this study, we analyzed proximity pattern, contact region, contact area, contact centroid, contact recurrency, and contact ratio to explore the spatiotemporal relations of the MC1 and the TPM in all positions of the movement. In the analysis, we applied 1.5 mm as the average cartilage thickness between MC1 and TPM based on the literature [82, 88, 64, 59]. Detailed definitions of these metrics were:
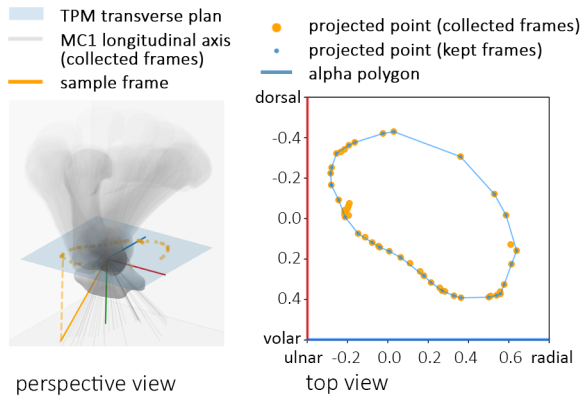
Figure 3.2: Step1: Select frames based on the orthogonal projection on the transverse plane of TPM. The projected points of the longitudinal of MC1 from collected frames are in yellow. The alpha shape as the boundary polygon is in solid blue lines. The small blue dots connected by the polygon are the frames kept for the interpolation step.
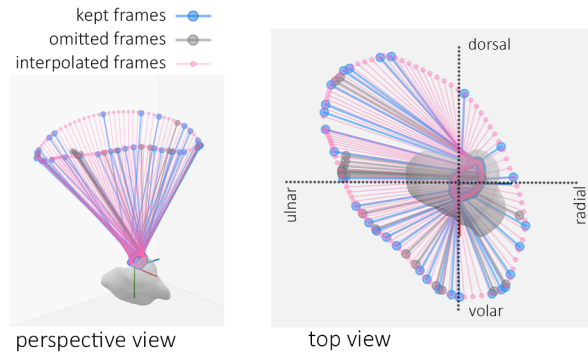
Figure 3.3: Step2: The interpolated frames (pink) based on the selection collected frames (blue). The grey dots mean the omitted frames. The MC1 bone was simplified with a bar for visualization.

- **Proximity pattern:**
  The proximity pattern measures the shortest bone-to-bone distance of the vertices on one bone to the vertices on the other bone.

- **Contact region:**
  The region where the bone-to-bone distance is smaller than 1.5 mm.

- **Contact area:**
  The area of the contact region.

- **Contact centroid:**
  The centroid of the contact region.

- **Contact recurrence:**
  For each vertex on the bone mesh, the frequency of its occurrences that the bone-to-bone distance is smaller than 1.5 mm.

- **Contact ratio:**
  For each frame, the ratio of the area of its contact region over the area of the contact region of the full circle.

$$contact\ ratio = \frac{the\ area\ of\ the\ contact\ region\ of\ a\ frame}{the\ area\ of\ the\ contact\ region\ of\ the\ full\ circle} \quad (3.1)$$

3.2.5. STATISTICAL ANALYSIS

The measurement metrics of joint contact were analyzed for female and male participants. An independent t-test was applied to investigate the average difference between the two groups. With a sample size (of 23 males and 24 females, the power of the reported analysis was around 0.8 (effective size 0.6). Based on the constructed point correspondence, the contact recurrency of all vertices on the contact region was also compared between the two sexes. The results were projected to the mean model of all included bone models based on the point correspondence for visualization.

3.3. RESULTS

3.3.1. THE MIGRATION OF CONTACT CENTER

The interpolated frames were aligned using spatial parameters approximately in the sequence of extension-abduction-flexion-adduction-extension, as shown in Fig. 3.4. Through the circumduction, the contact centroid mainly migrated along the ulnar-radial direction on the contact surface MC1 close to the volar side. For TPM, the major direction was along the dorsal-volar direction slightly around the radial aspect of the articulate surface. The contact centroid in each corresponding frame was extracted for females and males and is shown in Fig. 3.5.
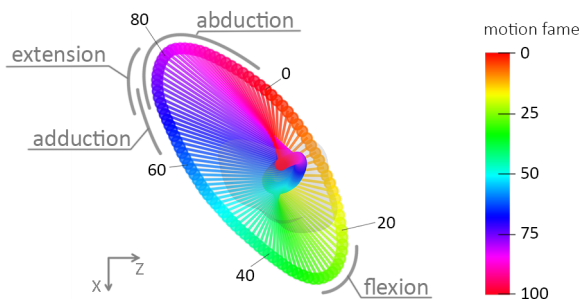
Figure 3.4: The average motion locus of the circumduction with interpolated frames. The approximate frame range representing the extreme key positions: extension, abduction, adduction, and flexion, are underlined with grey lines.
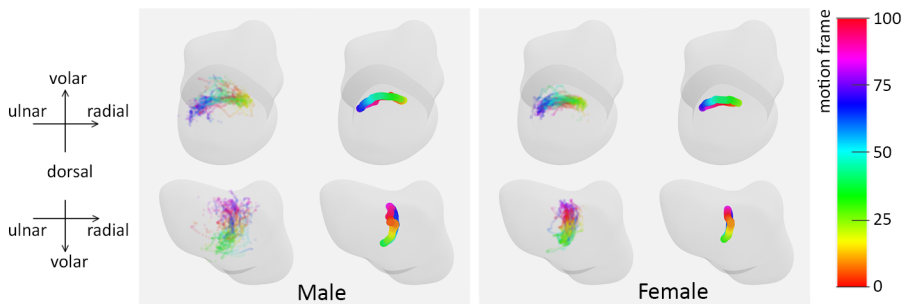
Figure 3.5: The migration of contact centroid of each participant (left of subplots) and the average (right of subplots) in the full circumduction are shown in the subplots for males and females. The contact centers in different frames are shown in the corresponding colors in the color bar.

3.3.2. CONTACT RECURRENCY OF THE MOTION CIRCLE

Joints of females presented higher recurrent frequency than those of males (with a 1.5 mm threshold). Fig. 3.6 shows the mean ±SD of the contact recurrency for females and males. The central-volar areas of MC1 and the central-radial areas of TPM have a higher frequency, with over 85% for females and 70% for males.
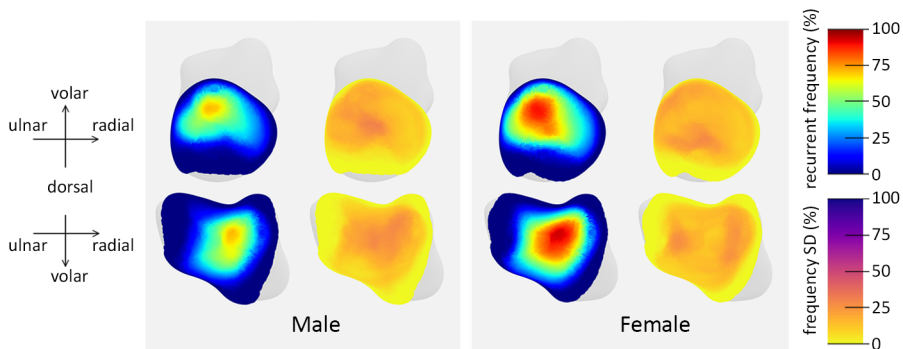
Figure 3.6: The contact frequency throughout the circumduction for males and females.

3.3.3. PROXIMITY PATTERN AND CONTACT AREA

The joint proximity patterns at five selected positions and of the full motion are presented in Fig. 3.7 for females and males, where the boundaries of the contact region are highlighted. The corresponding contact areas were measured, as shown in Table 3.2. After excluding flexion and opposition, the contact area of females in selected positions was larger than those of males. Females also had a smaller contact area regarding the full motion circle. The mean ±SD contact area of the TPM and MC1 in the full motion circle were 124.0 ±17.0 mm2 and 121.6 ±16.9 mm2 for females, and 138.6 ±20.5 mm2 and 135.3 ±20.1 mm2 for males.

The mean ±SD minimal bone-to-bone distance was 0.57 ±0.19 mm and 0.59 ±0.23 mm respectively for females and males. The distance of the volar radial quarter of both MC1 and TPM articulate surface was less than other quarters. Among the five selected positions, the minimal bone-to-bone distance of flexion and opposition positions were smallest for both sexes: 0.74 ±0.23 mm and 0.76 ±0.26 mm for females and 0.80 ±0.21 and 0.85 ±0.26 for males. The distance was largest in adduction, 1.02 ±0.14 mm and 1.13 ±0.17 for females and males respectively, as detailed in Table 3.2.
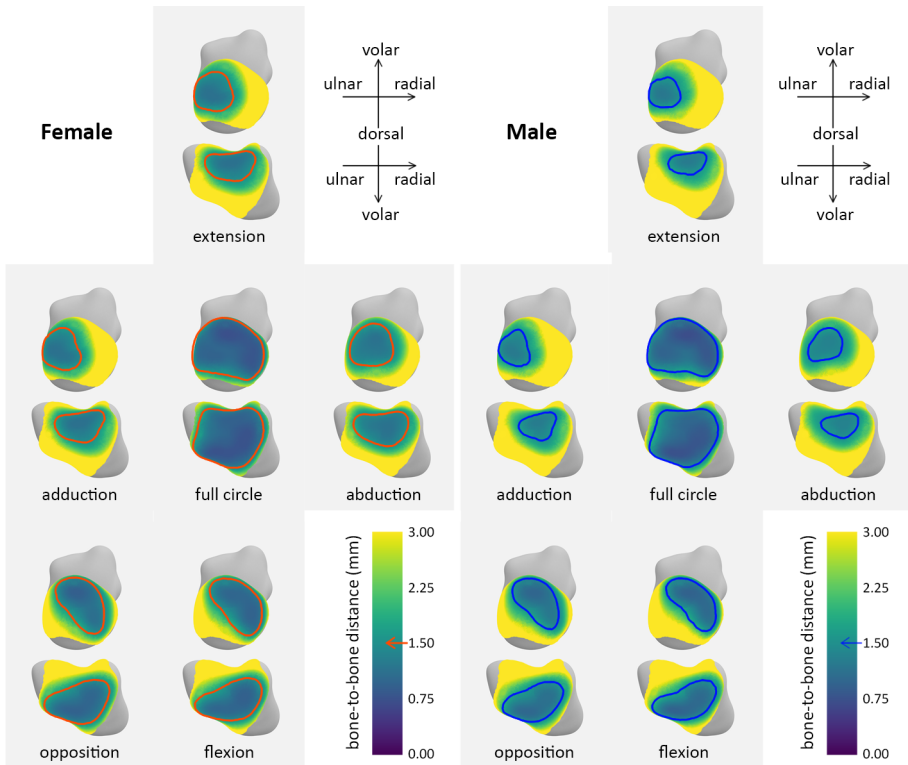
Figure 3.7: The proximity pattern in the five key positions and through the full movement circle. The boundaries of the region with proximity less than 1.5 mm are highlighted.

3.3.4. CONTACT RATIO OVER THE MOVEMENT

The contact ratio and the contact area in corresponding interpolated frames were investigated. The patterns for both females and males were generally similar. The peak of the contact ratio and the contact area appeared around frame 30 (approx. extreme flexion). Both the contact ratio and the contact area for females were significantly larger than those for males in most positions, excluding frames around 20 45 (approx. flexion and opposition), as shown in Fig. 3.8.

Table 3.2: Descriptions of the key positions for frame selection.

Positions	TPM contact area mean ± SD (mm2)			MC1 contact area mean ± SD (mm2)			minimal distance mean ± SD (mm)		
	Female	Male		Female	Male		Female	Male	
Flexion	63.4 ± 14.0	65.0 ± 15.5		62.4 ± 13.9	64.8 ± 15.7		0.74 ± 0.23	0.80 ± 0.21	
Extension	42.2 ± 15.2	32.1 ± 16.7	*	42.5 ± 14.9	33.0 ± 16.7	*	1.00 ± 0.20	1.10 ± 0.22	
Adduction	41.6 ± 13.8	30.9 ± 14.8	*	41.6 ± 13.2	31.6 ± 14.7	*	1.02 ± 0.14	1.13 ± 0.17	*
Abduction	51.4 ± 15.3	33.2 ± 21.7	*	52.6 ± 15.2	34.7 ± 22.3	*	0.96 ± 0.19	1.11 ± 0.27	*
Opposition	63.6 ± 16.8	62.8 ± 26.4		63.1 ± 16.6	62.1 ± 26.8		0.76 ± 0.26	0.85 ± 0.26	
Full circle	124.0 ± 17.0	138.6 ± 20.5	*	121.6 ± 16.9	135.3 ± 20.1	*	0.57 ± 0.19	0.59 ± 0.23	
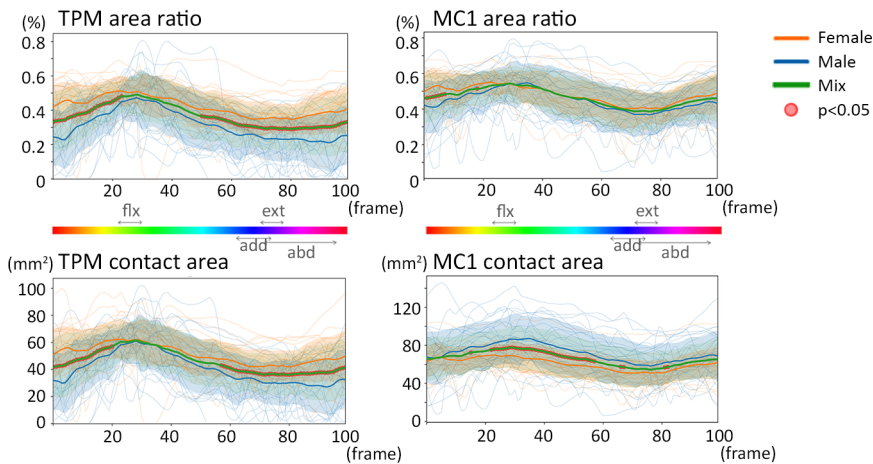
Figure 3.8: The average of the contact ratio and the contact area of the interpolated circumduction for females and males are shown in orange and blue lines. The solid lines mean the average and the corresponding transparent bands indicate the standard deviation. The green solid lines mean the average of the mixed-sex population, and frames with a statistical difference (p<0.05) are pointed with red dots.

3.4. DISCUSSION

The goal of this study was to investigate the joint contact of asymptomatic thumb carpometacarpal joints (CMC-1) during maximum thumb circumduction and compare the contact measurement metrics between males and females. The results show

that the contact recurrency for females is higher than that for males. Moreover, the contact ratio was higher for females in the majority part of the circumduction. The contact area in these frames was also larger for females, however, their contact area of full motion circle was smaller than those of males. The contact centroid of all participants mainly migrated along the volar-dorsal direction for trapezium (TPM) and along the ulnar-radial direction close to the volar aspect for the 1st metacarpal bone (MC1).

3.4.1. COMPARABLE PROXIMITY PATTERN AND CONTACT CENTERS

The minimal bone-to-bone distance of the full circumduction was similar for females and males, and both appeared around the volar and radial aspects of the two bones. The minimal distance of the volar and radial aspects of TPM was smaller than that of the dorsal-ulnar quadrants; similarly, the minimal distance of the dorsal aspect of MC1 was larger than that of the other regions. Throughout the circumduction, the minimal proximity was about 0.6 to 1.1 mm. This range is approximate to the sum of the cartilage thickness of the four quadrants of the two bones: 0.5 to 1.0 mm as reported in a CT measurement [89]. The proximity pattern seems also associated with the variation of cartilage thickness of the articulate quadrants. Several studies have confirmed that the cartilage of the ulnar-dorsal quadrant was the thickest and the radial-volar quadrant was the thinnest for both TPM and MC1 for asymptomatic CMC-1 [88, 59, 89].

For the measurement of selected positions, we compared our results with those from the existing literature (Fig. 3.9). For oppositions and flexion, the contact region was mainly in the volar and radial aspect for both sides, in accordance with the literature [33, 83]. The dorsal aspect of TPM and the ulnar and central aspects were the main contact area of MC1 for adduction, abduction, and extension, as found in most studies [37, 81, 33, 83]. The calculated contact area of our study was slightly smaller than that reported in a study with a single participant dynamic measurement [83], while our results presented the average of all participants. Moreover, we observed the migration of the contact centroid of the two target bones in greater detail, and our continuous pattern is consistent with a study where the contact centroid of the selected frames was mostly close to the volar side of MC1 and the radial side of TPM at selected key positions [33]. The migration of the contact center is worthy of consideration in an implant design [90].

3.4.2. HIGHER CONTACT RECURRENCY FOR FEMALES

With the advantage of dynamic in-vivo measurement and the augmented frames, we aimed to assess the contract recurrency and contact ratio during the circumduction. Our analysis suggests higher recurrent frequency for females; the area with recurrency over 70% was much larger for females than males. This higher recurrency suggests constant pressure over these regions in more possible positions within the motion range, which can possibly lead to a more vulnerable state with the same material (cartilage) property [91, 92]. For both sexes, the recurrence of central and radial
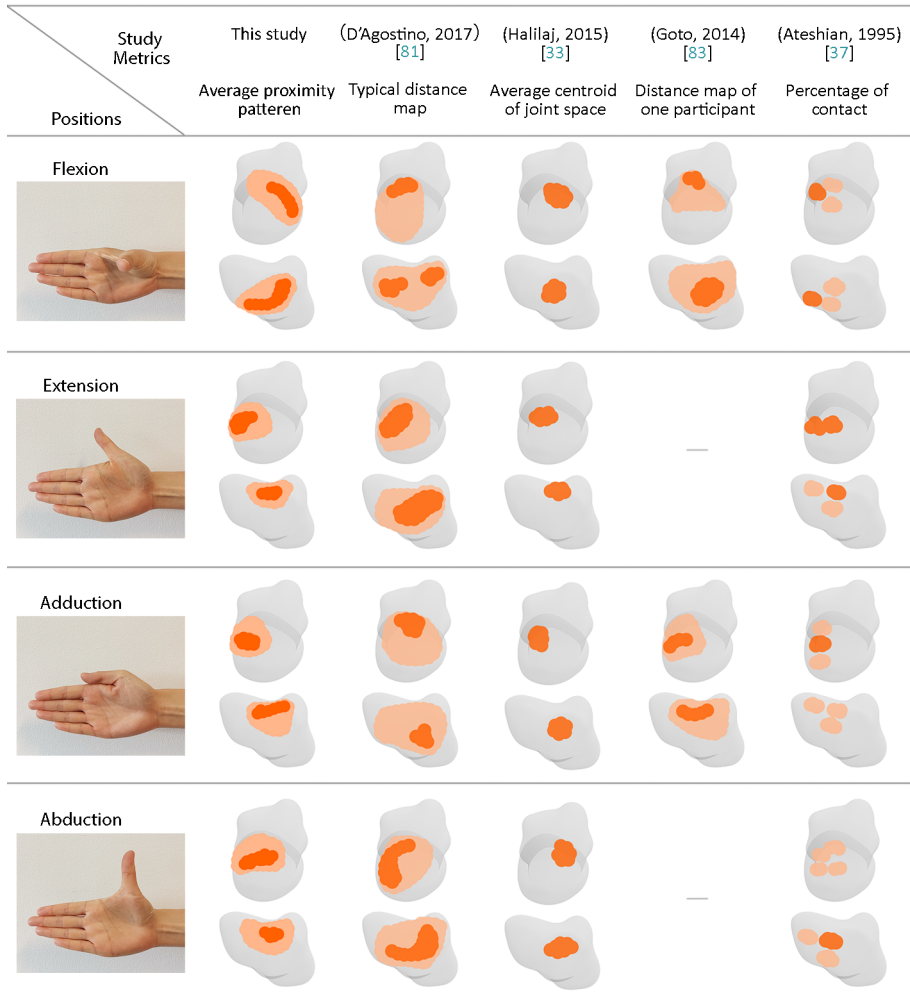
Figure 3.9: The summary of the proximity/contact center/percentage of contact in previous studies and this study for comparison.

aspects of TPM and volar and central aspects of MC1 presented higher contact recurrency (Fig. 3.6). This phenomenon was also mentioned in a study with selected static positions, yet without further assessment [81]. The more frequent contact in the volar and radial side for MC1 and TPM may be associated with wear patterns of CMC-1 OA which initiated from the radial aspect to the volar aspect for the two bones [64, 93, 94, 95]. Population-based studies have reported that females are more vulnerable to the CMC-1 OA than males [16, 13]. Although multiple factors (e.g., genetic and metabolic factors) can lead to joint degeneration [16, 12, 73], the mechanical

contribution also has to be considered. From the aspects of bone morphology and biomechanics, research on the bone shape indicates that the significantly smaller bone size of females may lead to higher stress with the same loading, which may explain the higher prevalence of CMC-1 OA among females [56]. Focusing on joint contact, this study analyzed the contact recurrence and contact area. We found a larger contact area for females in extension, adduction, and abduction. Our findings on the higher contact recurrency for females can also extend the understanding of the etiology of CMC1 osteoarthritis and the higher prevalence of CMC-1 OA for females.

3.4.3. HIGHER CONTACT RATIO FOR FEMALES

The comparison of the contact ratio between the two sexes over the movement implies that female CMC-1 joints are more vulnerable than those for males. As shown in Fig. 3.8, a larger portion of the articulate surface of females was involved in the circumduction, excluding approximately 1/4 of the movement around the opposition position. However, the contact area of the full circle for females was smaller than that for males. As also shown in Fig. 3.7, the projected contact area on the mean model of females is larger than that of males. The higher contact ratio of the movement suggests that a larger part of the articulate surface of females is under stress in most possible positions, and thus these soft tissues are more vulnerable to the fatigue limit of the cartilage [91, 92].

Nonetheless, further measurement of cartilage thickness is necessary as our analysis was based on a uniform cartilage thickness assumption. The measurement of soft tissue was excluded due to the limitations of the scanning resolutions and the knowledge of cartilage modeling. Instead, following previous research [56, 33, 96], we defined the cartilage thickness of all articulate regions as 1.5 mm for both females and males. This is supported by cadaver studies, where the average cartilage thickness of MC1 and TPM articulate surfaces were 0.7 ±0.2 mm and 0.8 ±0.2 mm [88, 64, 89]. The literature suggests no significant material property differences between articular sub-regions [59], although the volar side has thinner cartilage [88, 89]. Also, no significant sex- or size-related differences were found [89, 97]. Yet, its relationship with bone size is uncertain. Current investigations of cartilage thickness have mainly been based on cadavers of people aged over 50 [88, 64], while the majority of our participants were aged between 20 to 40 and whose cartilage property may be in a better condition. A confirmation of the relationship between cartilage thickness and the bone volume or dimension for the CMC-1 can be helpful to the cartilage modeling in analysis, and this is also important to the finding of a high contact recurrency for females.

3.4.4. LIMITATIONS

The circumduction in this study was represented with unified interpolated frames, since the limited knowledge and the measurement of motion range of thumb and frequency in daily activities. The weighting of the frames can be optimized in future analysis [98, 99, 100], e.g., increasing the weighting for opposition, flexion, and

adduction. Considering the results in Fig. 3.7, the recurrency at the radial side of TPM and the volar side of MC1 may even magnify. Studies on daily hand manipulation concluded that medium wrap, lateral pinch, and thumb-2 finger, were the top three manipulation positions in daily life, and these actions involved thumb opposition and adduction, accounting for around 60% of daily use [2, 98, 67]. However, the rotation angles during these activities and the approximate weighting are currently unclear. Apart from this, collecting continuous active movement has the advantage of enabling a more natural movement without constraint from applied guided jigs [33], but the external forces applied in reality may further deform joint contact [11, 84]. Besides, compared with studies that employed 3D CT images that recorded the bone in static positions, images of 4D CT can include motion blur in some frames. This phenomenon was mainly observed in the movement from opposition to adduction. Therefore, we adopted a B-spline interpolation approach to smooth and mitigate such influence.

3.5. CONCLUSION

This study assessed the joint contact of CMC-1 with continuous measurement during a maximum thumb circumduction. The goal was to understand the average joint contact in the asymptomatic population, and the difference of the joint contact between females and males. The finding suggested a similar migration pattern of the contact center for both sexes in general. However, differences were found regarding contact recurrency, contact area, and contact ratio. For females, a larger portion of the articulate surface was involved in most frames of the circumduction than males, and the contact recurrency was higher. Our results of continuous measurement can extend the knowledge of the arthrokinematics of CMC-1 joint. The findings based on asymptomatic populations can serve as the baseline and might also be useful for the etiology and intervention of CMC-1 OA.

4

CMC-1 MOVEMENT BOUNDARY

This chapter continues the CMC-1 in-vivo study during movement by **tracing the motion boundary in three dimensions**. The relative translations and rotations between the 1st metacarpal bone and trapezium are analyzed. One highlighted finding is that the locus of the first metacarpal bone in a circumduction forms a skewed hyperboloid shape, and the waist of the shape is on the first metacarpal side instead of the trapezium side. The findings enrich the understanding of CMC-1 movement in 3D and provide a reference for improving the validation examination in the development of implant replacements for CMC-1.

4.1. INTRODUCTION

The thumb-base joint (CMC-1) supports the movement of the thumb which is indispensable to hand use in daily activities [101, 13]. A degenerated CMC-1 causes pain and limits the use of the thumb [13, 73, 102]. Clinical studies pointed out that the age of patients with CMC-1 osteoarthrosis is younger than before [19]. For patients who still require thumb mobility and functionality [19, 24], implant replacement is one of the options to correct the biomechanical factors of the symptomatic joints into a healthy state.

Although CMC-1 implants have realized pain relief and joint mobility with satisfaction in the short-term, implant loosening and dislocation are the leading complications for the long-term outcome [24, 103]. Currently, the CMC-1 implants are mainly based on a ball-socket mechanism: the socket is placed in the trapezium (TPM) and the steam is in the 1st metacarpal (MC1). This mechanism is similar to the one for hip implants [24]. With the optimization of the materials and structures, some studies reported an approximate 90% survival rate for 10 years [24, 103]. Still, some research argues that the ball-socket mechanism failed to represent the natural movement of the CMC-1 [104], which can be linked with low satisfaction and the high failure rate caused by mechanical factors.

Therefore, a solid knowledge of the arthrokinematics of the natural state of the asymptomatic CMC-1 is essential. Invasive radiographic scanning is still necessary to acquire the accurate in-vivo positions of TPM and MC1 in different poses. Most research was based on the selected extreme positions or the linear movement between positions: flexion, extension, adduction, and abduction, or sometimes, the opposition [32, 105, 85, 106, 36]. Yet, the continuous form of these extreme positions and the details between these frames were only studied with specimens [38, 107, 108] or a small dataset with in-vivo measurements [83, 84]. The movement in daily activities is usually a combination of flexion-extension (flx-ext) and adduction-abduction (add-abd). Thus, research on the composite circumduction movement is needed to cover more scenarios for a comprehensive understanding of thumb movement [100].

In this study, we aim to understand the boundary trace of the CMC-1 movement in space for the asymptomatic population. For this, we collected 4D CT data during the maximum thumb circumduction and analyzed the movement by extracting the motion trace and the arthrokinematics variables throughout one circle of the maximum circumduction. The circumduction can enable participants to perform a more natural movement with less intervention. In addition, 4D CT scanning techniques were applied to collect and track detailed motion frames. The outcome of this study can inspire implant optimization, provide boundary conditions for engineers in designing and validating future implant replacements for CMC-1, and help clinicians for a better understanding of the biomechanics of the CMC-1 joint in the natural state.

4.2. Methods

4.2.1. Data acquisition

With the approval by the local medical-ethics committees (NL70432.058.19), this study included the 4D CT scans of the dominant hands of 47 participants: 24 females and 23 males, 45 righted-hand and 2 left-handed. The average age of all participants was 34.6 (± 10.7) years old, ranging from 19 to 61 years old. All participants signed the consent form and indicated no discomfort or injuries or history of hand surgery. Also, the absence of joint degeneration in these datasets was confirmed by the hand surgeon (GK) based on the medical images or 3D bone models. The study goal was well informed to the participants to ensure that we collected the maximum reachable range of their thumb mobility. A pre-recorded video of the movement was displayed as guidance during practice and scanning to ensure the movement speed and approximate poses [a]. The target circumduction started from 1) natural position, followed by 2) adduction, 3) opposition, 4) flexion, 5) abduction, 6) extension, and back to the 7) initial position, as shown in Fig. 4.1. A full circle of the movement took approximately 12 seconds. The applied scanner was Canon Aquilion ONE 320-slice, with scanning setting: tube voltage 80kV, slice thickness 0.5mm, FOV 180mm, and resolution 512x512 with an increment of 0.25mm, 4 frames per second. The total radiation dose was less than 0.06 mSv for one scanning.

1./7. natural
ready to start/end at a
natural position

2. adduction
rotate the thumb next to
the index finger

3. opposition
rotate the thumb towards the pinky finger

4. flexion
rotate the thumb and point
away from the palm

5. abduction
rotate the thumb away
from the index finger

6. extension
rotate the thumb towards
the back of the hand
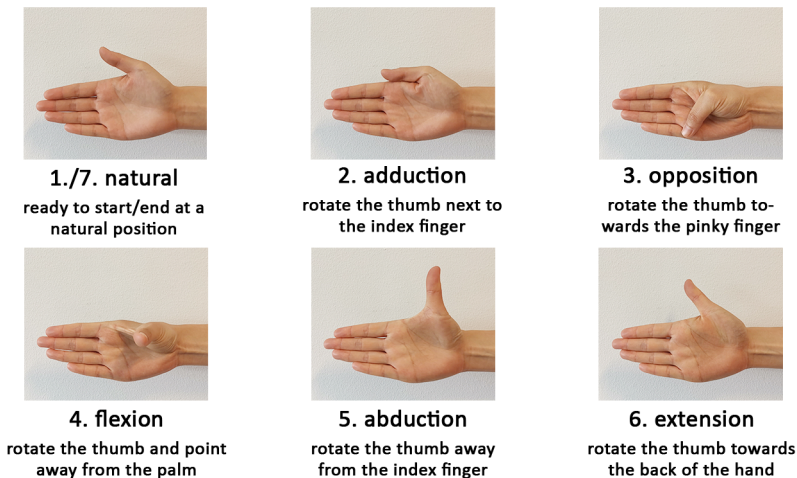
Figure 4.1: Key poses of the target circumduction movement.

4.2.2. Local coordinate systems

The geometry contours of TPM and MC1 in the first frames were extracted to generate bone meshes respectively with Philips IntelliSpace Portal (Amsterdam, Nether-

---

[a]link: https://www.youtube.com/watch?v=-A88Y0tI18Y

lands). Respectively, the positions of the two target bones in the remaining frames were identified with a self-developed Python program (version 3.6). All processed data were further checked and adjusted using Geomagic Design X (Geomagic Inc., Morrisville, NC, USA) to guarantee that the data depicted the real movement. Thus, each movement was represented by a sequence of mesh models.

These models were adopted to construct the local coordinate systems (*LCS*) of the two bones: LCS_{TPM} and LCS_{MC1}. For this, the region with bone-to-bone distance less than 3mm throughout the full movement was first identified, as:

$$p_{TPM_i}, p_{MC1_i} | \forall f, \| p_{TPM_{i,f}} - p_{MC1_{j,f}} \| < 3$$

where the p_{TPM_i} and p_{MC1_i} refers to any vertices i on the bone model of TPM or MC1, and f refers to any collected frames.

Then a hyperbolic paraboloid (a saddle surface, the yellow regions in Fig. 4.2) was fitted to this region to construct the *LCS* of the bones following the approach proposed in [109], where the origin of the *LCS* is the saddle point of the fitted surface. The Z-axis and X-axis correspond to the directions of maximum and minimal principal curvature, approximating the ulnar to radial and dorsal to volar respectively. Then the Y-axis is the cross product of the Z-axis and X-axis, pointing to the proximal direction, as shown in Fig. 4.2.
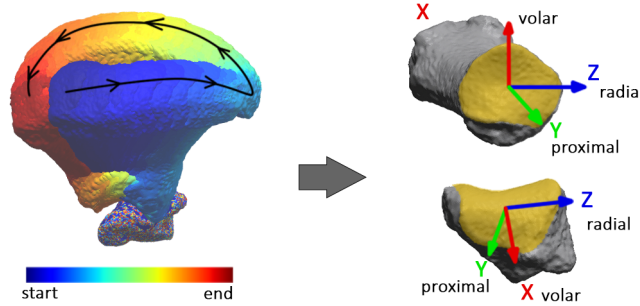
Figure 4.2: The illustration of constructing the local coordinate system (LCS) that is extracted based on the contact area of the full circle of movement.

4.2.3. TRANSFORMATION MATRICES AND MOTION LOCUS

Taking the TPM bone as the reference and LCS_{TPM} as the reference coordinate system, we aligned the mesh of the TPM in all frames and transform the position of the MC1 in the corresponding frames. Considering the full alignment between the LCS_{MC1} and LCS_{TPM} as the reference frame, say $f = f_0$. Then, the relative positions of the MC1 to the TPM in each frame $f = f_i$ were identified with a homogeneous transformation matrix RT_{m,f_i}, which included the translation and rotation from LCS_{TPM} to LCS_{MC1}, as detailed in the Eq.4.1 and illustrated in Fig. 4.2(c). Followingly, the trace of the relative motion was computed from these transforma-

tion matrices. The MC1 bones were represented with a bar from the original of the LCS_{MC1} to the distal direction.

$$\begin{cases} M_{TPM,f_i} = RT_{TPM,f_i} * M_{TPM,f_0} \\ M'_{MC1,f_i} = RT_{TPM,f_i} * M_{MC1,f_0} \\ M_{MC1,f_i} = RT_{m,f_i} * M'_{MC1,f_i} \end{cases} \qquad (4.1)$$

where M_{f_i} means the bone model at the frame $f = fi$, RT_{TPM,f_i} means the homogeneous matrix for aligning the TPM at any frames to the reference frame $f = f0$, and RT_{m,f_i} represents the relative rotation matrix for MC1 at frame $f - f_i$ to the reference frame.

(a) the anatomical LCS alignment and the rotations around the three axes

(b) The relative transformation calculation
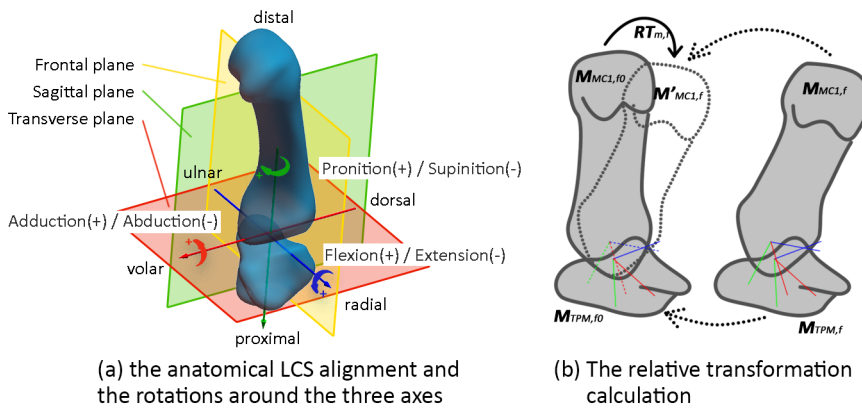
Figure 4.3: The alignment of the two anatomical LCS and the corresponding rotations along the three axes, along with the relative transformation calculation between the two bones. TPM bone is considered as the reference.

4.2.4. KINEMATIC VARIABLES

Six kinematic variables of the movement were analyzed, including the gliding distance, the proximity distance, and the rotation angles. To describe the relative positions between the MC1 and TPM, we introduced azimuth (azi) angle as a control parameter [110], which approximately interprets the position of MC1 in the circumduction. As illustrated in Fig. 4.4a and 4.4b, when azi = 0 and 90, the MC1 is approximately in the pose of flexion and abduction respectively. With the translation aspect in the transformation matrices, the gliding distance and the proximity were calculated, see Fig. 4.4c; and the rotation angles were calculated from the rotation aspect of the transformation matrices, as Fig. 4.4d. Detailed calculations of these variables are as follows.

- **Azimuth (azi) angle**: The angle between the positive X_{TPM} and the projection of the $-Y_{MC1}$ axis on the XZ plane of LCS_{TPM}, as $projv_{XZ}$, suggested in a previous study [109]. Using the rotation information to identify the relative poses in the circumduction. The range of azi is $azi \in [-180, 180] deg$

- **Gliding distance**: The arc length from the origin of LCS_{TPM}, to the proximity point along the two directions of the principal curvatures of the hyperbolic paraboloid surface fitted to the articulate surface of TPM.

- **Proximity distance**: The distance between the origin of LCS_{MC1}, and its proximity point on the articulate surface of TPM.

- **Rotation angles**: The Euler angles calculated from the rotation aspect of the transformation matrices using Z_{TPM},–Y–X_{TPM}, the sequence corresponds to the Flx-Ext, Add-Abd, pronation-supination (Pro-Sup) rotation [109, 111].
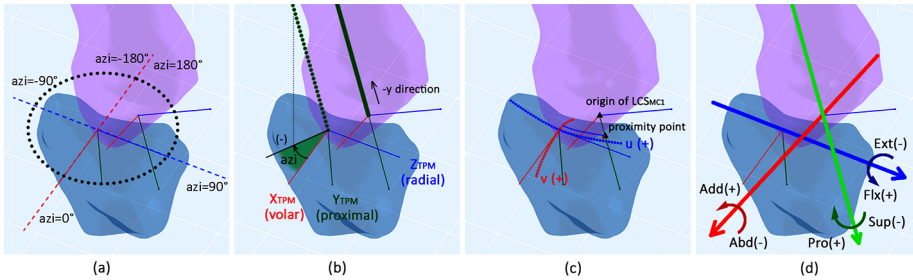
Figure 4.4: Illustrations of parameters extracted from bone models. (a,b) The azi angle is calculated from the projection vector of the $-Y_{MC1}$ axis; (c) the gliding distance and the proximity distance; (d) the three rotation angles. Add: adduction; Abd: abduction; Flx: flexion; Ext: extension; Pro: pronation; Sup: supination; (+): rotations shown in positive values; (-): rotations shown in negative values.

4.3. RESULTS

4.3.1. THE MOTION TRACE OF THE CIRCUMDUCTION

The mean motion traces for males and females are presented in Fig. 4.5a, where the MC1 bone is represented with a bar (50 mm) from the origin of LCS_{MC1} towards the proximal end along $-Y$ axis direction. The gildings of MC1 followed a quasi-ellipse path, between the dorsal-radial tubercle to the saddle point of the TPM articulate surface, as shown in the transverse view. Moreover, the movement of the bar formed a skewed hyperboloid in space. Based on the average trace of all data (both females and males), we calculated the transversal projected area of the polygons that formed by the points on the bar, as the yellow curves indicated in Fig. 4.5b. The point was about 7.2 mm from the distal end of the bar (the saddle point of the articulate surface on MC1 bone); and its trace, as formed by green dots, represents the waist of the skewed hyperboloid with the smallest projected area.

(a) the average motion boundary
for females and males

(b) the average motion boundary
(mixed sexes)
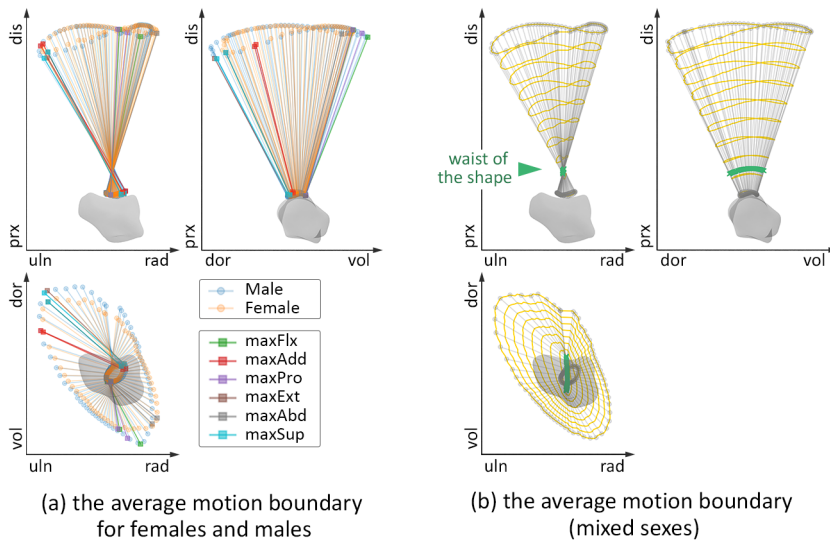
Figure 4.5: (a) Mean motion locus of females (orange) and males (blue); (b) Mean locus of all participants. Yellow polygons: created by the points on the bar for illustration. Green arrow: point on the bar that forms the waist of the hyperboloid shape.

4.3.2. THE ARTHROKINEMATICS VARIABLES DURING THE MOVEMENT

In addition to the motion trace, the extreme and the range of the arthrokinematics variables were calculated. Throughout the maximum reachable circumduction, the origin of the MC1 bone glided along the surface of TPM from -3.9 to 6.8 mm between the ulnar-radial direction, and from -8.6 to 0.5 mm between the dorsal-volar direction. The proximity changed between 1.0 to 2.0 mm. On average (± standard deviation), the MC1 rotated relative to TPM from 33.1° (± 8.4°) extension to 18.2° (± 5.6°) flexion, from 22.2° (± 6.2°) abduction to 19.3° (± 5.6°) adduction, from 17.9° (± 7.8°) supination to 19.3° (± 6.7°) pronation. Details of the movement range for females and males are listed in Table 4.1. The changes of these variables in regards to the azi angles are shown in Fig. 4.6.

Table 4.1: The motion range of the arthrokinematics variables for females and males.

	Gliding distance u (mm)	Gliding distance v (mm)	Proximity distance (mm)
	ulnar(-) – radial(+)	dorsal(-) – volar (+)	
Female	11.0 (± 2.7)	9.5 (± 2.8)	0.8 (± 0.3)
Male	14.2 (± 4.8)	12.7 (± 5.8)	1.1 (± 0.5)
	Flexion-Extension	Adduction-Abduction	Pronation-Supination
Female	48.4° (± 11.2°)	51.4° (± 7.6°)	39.2° (± 8.2°)
Male	53.0° (± 13.2°)	52.8° (± 11.8°)	33.5° (± 7.6°)

Comparing the average of the two sexes, the three size-dependent variables, in the upper row of Fig. 4.6, suggested that the gliding ranges and the range of proximity for males were larger than that for females. In comparison, the rotation angles, which are size-independent variables, for both sexes were generally similar; yet the self-rotation range for females seems slightly larger than that for males, as shown by the bottom row in Fig. 4.6.

4
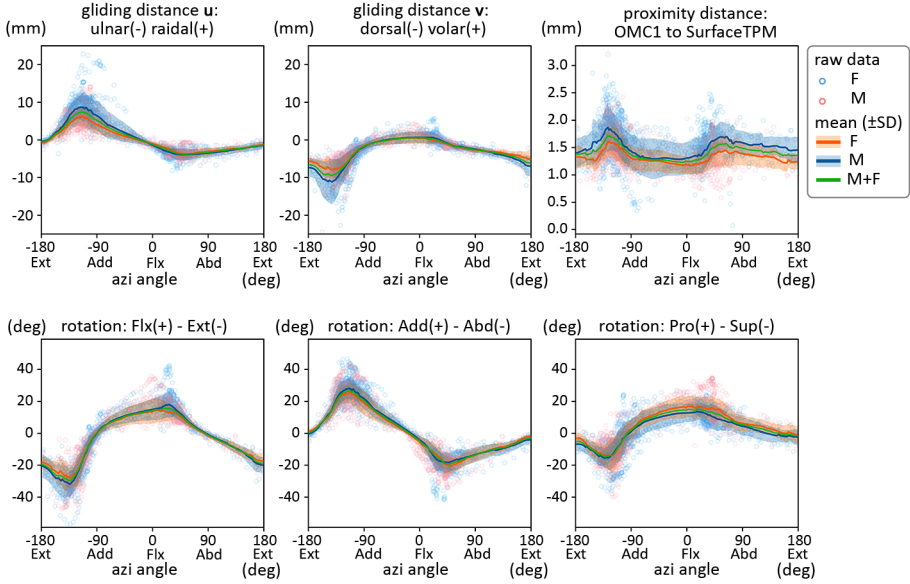
Figure 4.6: The relationship between azimuth (azi) angle and the kinematic variables during the movement, including variables: gliding distance along TPM surface, the proximity distance of the origin of LCS_{MC1}, and the rotation angles. 'F': female; 'M': male; '+': volar direction, radial direction, flexion, adduction, pronation; '-': dorsal direction, ulnar direction, extension, abduction, supination.

4.4. DISCUSSION

4.4.1. THE RANGE OF THE ARTHROKINEMATICS VARIABLES

The ultimate goal of this study was to understand the movement of the thumb-base joint (CMC-1) based on continuous scanning data. For this, the study first evaluated the translations and rotations variables in one circle of maximum circumduction. The mean curves in Fig. 4.6 indicate that the maximum proximity distance and the gliding distance for males are larger than that for females. This can be linked with the bone size and the joint space of asymptomatic males is larger than that of females in general [56, 89]. Still, the pattern of the two mean curves was similar. Likewise, the rotation pattern through the circumduction of males and females are also alike, and females presented slightly higher pronation angles on average, as shown in Fig. 4.6, especially around the flexion pose. Pronation-supination is a

more demanding rotation that increases the instability of the CMC-1. Although no strong statistical difference can be concluded due to the small sample size, the difference in the joint self-rotation for females and males is worth attention in rehabilitation programs or the design of the splint. Compared with previous in-vivo studies on CMC-1, our flexion-extension (flx-ext) and adduction-abduction (add-abd) range were generally comparable with most previous studies [85, 83, 110, 112, 113], yet some studies reported less motion range [32, 106]. Our pronation-supination (pro-sup) range were in accordance with [85], but larger than most studies for about 10 degrees [32, 106, 83, 110, 113]. Flexibility and the performance of each included participant in different studies and the variance in the study designs may introduce measurement differences among studies. Most previous results were based on the thumb linear movement between the four extreme positions; however, this study measured the range of a continuous nature movement with less intervention.

By describing the position of the 1st metacarpal (MC1) relative to the trapezium (TPM) using the azi angles, the rotation of the CMC-1 reached maximum extension, adduction, and supination when the azi approached -118.2° to -132.7°; and when azi approximated to 20.0° to 49.1°, the MC1 rotated most in flexion, abduction, and pronation. The extreme rotations were presented around the two ends of the major axis of the quasi-ellipse locus. The three rotations changed simultaneously through the movement along with the translations, as well as the proximity distance throughout the movement, this implied the screw-home mechanism which is consistent with previous literature [101, 32, 105]. Besides, the peak in the proximity measurement in Fig. 4.6, when the joint reaches the extreme positions in the circumduction, also suggested the migration or the change of the pivot point for joint contact.

4.4.2. THE HYPERBOLOID MOTION TRACE

Based on the mean of the extracted arthrokinematics variables, our analysis suggested that the relative motion trace between the MC1 and the TPM formed a skewed hyperboloid. This motion trace has two mean features for discussion: the quasi-ellipse traces of the MC1 and the waist of the hyperboloid.

Both the proximal and the distal ends of the MC1 formed two quasi-ellipse traces, and this is in accordance with a previous cadaver study [107]. Moreover, the principal axes of these two traces seem approximately orthogonal in the transverse view of Fig. 4.5. The average gliding path of the MC1 was between the center and the radial-dorsal aspect of the articulate surface of the TPM. This finding can be beneficial for identifying an optimal rotation center for ball-socket implants. Currently, the approximate center of the articulate surface is the reference for implantation according to the instruction manual. If minimizing translation in the movement to mitigate the mechanical force for dislocation is the priority factor in optimization [104], we may suggest a slightly dorsal and radial side rotation center if the ball-socket part has to be on the TPM side. However, the rotation center needs to be optimized based on the required movement range and activities. Future biomechanical studies and computations with the symptomatic joint and the joint with arthroplasty are needed.

The skewed hyperboloid motion trace found in this study presents the concurrent

relative translation and rotation of MC1 over the articulate surface of TPM through-out the circumduction. Instead of the planar ellipse cone of motion, which was men-tioned in a cadaver study [108], the hyperboloid shape reflects the nature of insta-bility resulting from the saddle surfaces. Further analysis of the average motion lo-cus found that about 7.2 mm proximal from the MC1 articulate surface formed the smallest orthogonal projection area on the transversal plane. This means that the translation of this point was least in one circle of movement. The projection polygon was almost a slim ellipse aligned in the volar-dorsal direction, as shown in Fig. 4.5. Despite that ball-socket mechanism locates on the TPM side, generally, the center of the circumduction is on the MC1 side for the asymptomatic population. Although using different methods, our finding is in accordance with a recent work that identi-fied that the optimal rotation center was outside the TPM [114].

For visualizing the difference between the two motion mechanisms, the approx-imate theoretical movement paths of the ball-socket mechanism are shown in Fig. 4.7, one with a straight neck implant design and one with 15 degrees for the neck. The theoretical motion trace of the ball-socket design failed to present the natural motion range of the CMC-1. However, considering the functional workspace [115] and the required movement range, by adjusting the rotation center and the implan-tation angles (the elevation angle), the movement range can be optimized for pa-tients to maintain a certain range of motion. Yet, the functional motion range for daily activities needs further in-vivo measurement and research.
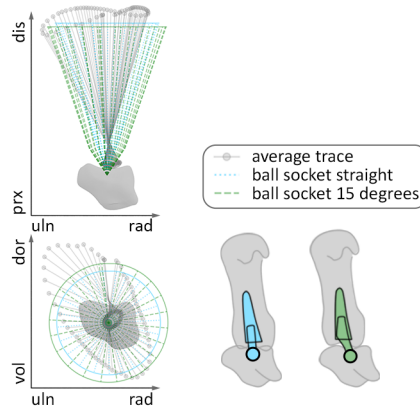
Figure 4.7: Illustration of the average trace of circumduction for asymptomatic CMC-1 and the theoretical trace for CMC-1 with ball-socket replacement.

4.4.3. TWO POTENTIAL TYPES OF MOTION TRACE

Reviewing the motion trace of each dataset, two types of motion locus can be iden-tified based on the ratio of the major and minor of the quasi-elliptic. As examples in Fig. 4.8, the left motion trace presents a relatively slimmer elliptic than the one on the right, although both participants received the instruction to perform the maxi-

mum circumduction following the same instruction video. Among the datasets, the motion loci of around 8 participants were close to the left example in the figure, and the rest were close to the right one. Insufficient guidance may be a factor of these two identical differences, otherwise, the mobility of the joint can be the major contribution to such distinction. The joint mobility and the motion trace can be associated with bone morphology where further studies are needed to confirm this assumption. In addition, a larger dataset can help to verify the classification of two types of motion traces.
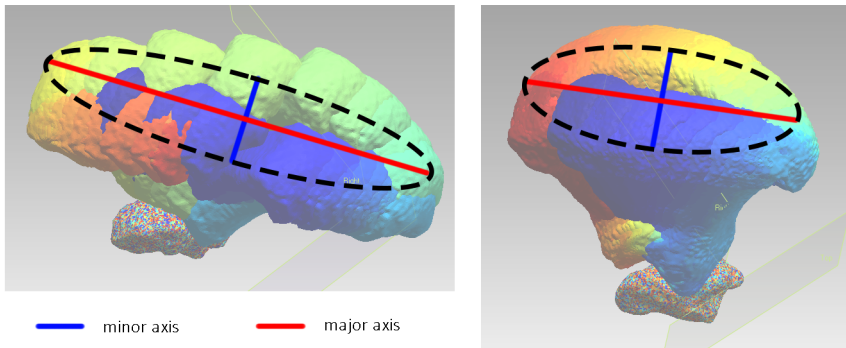
Figure 4.8: Examples of two identical movements.

4.4.4. LIMITATION

One of our limitations was the isolation of the CMC-1 joint in the analysis. The focus of this study was the relative movement between the MC1 and TPM, the chain effect in the full thumb joints and the carpal joints was excluded. Another limitation was the lack of loading scenarios in the measurement. The designed movement presents the maximum reachable range in unloaded situations, loading in functional activities will also increase the instability of the joint [84, 11]. However, understanding the unloaded boundary is also important to assess the computation models or provide insights into optimizing the implants.

4.5. CONCLUSION

This study investigated the movement of the CMC-1 when reaching the maximum range in a circumduction movement without loading. The boundary motion trace in space formed a skewed hyperboloid with quasi-ellipse ends. The relationship between the three rotations and the translations was also studied, and this can serve as a reference when examining the long-term performance of implant designs. Our findings can extend the current understanding of the nature of CMC-1 and offer insights for implant replacement optimization and potential new designs.

5

AN OPTICAL MEASURING SYSTEM

The Chapter demonstrates **the details of the optical tracking system** that was applied in the optical study. The goal is to develop a wireless tracking system to measure the joint rotation angles of all hand fingers during movement. In this chapter, three calculation methods are compared, and the repeatability and accuracy of the system are discussed through experiments. Finally, the measurement results of a pilot study are demonstrated.

5.1. INTRODUCTION

The human hand is a marvel of dexterity which is enabled by 27 bones and 19 joints (excluding the radiocarpal joint) [117, 118]. Literature studies indicated that simplified full-hand kinematic skeletons often have as many as 18-27 degree-of-freedoms (DOFs) [119, 120, 121], which often poses challenges to hand kinematic studies, e.g. scanning and tracking the hand motion in various scenarios [122, 123]. However, tracking hand movements to improve the understanding of hand kinematics is essential in the design of human-computer interaction (HCI) [124, 125], robotic grippers [126], and medical and rehabilitation devices [127, 128].

Among all methods to measure the joint rotation angles, using an (electro-) goniometer is the most classical way in clinical practice [129]. Yet, the quality of the results strongly depends on the skill and the experience of the user. Large inter- and intra- observer variations are inevitable [129, 130], e.g. the intra-observer variation might reach 4 to 10 degrees [131, 132]. Besides, it is challenging for both the participant(s) and the operator(s) when measuring multiple finger joints using a goniometer.

Advancements in technology enable measuring the finger joint rotations in a dynamic setup, where the sensor-based and vision-based approaches are typical examples [133, 134, 135, 136]. In applications using inertial measurement units (IMUs), the sensor modules are often placed at the dorsal side of the hand for estimating joint rotations using the data from the accelerometers and gyroscopes (and magnetometers if available) [137]. The repeatability errors of those systems were reported in the range of 2 to 10 degrees [137, 138, 139, 140]. However, professional 6 DOF IMUs can achieve an orientation accuracy of 0.5 degrees (Root-Mean-Square-Errors, RMSEs) [141]. The flex sensor is another type of sensor employed to measure joint rotation angles. It is thinner and less intrusive with a repeatability error of around 4 to 10 degrees [142, 143]. Some commercial data gloves using flex sensors reported a repeatability error within 2 degrees [144, 145]. However, the movements of the hand and the glove are not always the same due to the fit of the glove. Besides, cables are often required to transmit data and supply power, which further limits or interferes hand movements in performing some daily activities, such as precise manipulations.

On the contrary, the vision-based approaches enable more free movements of hands as the sensors (e.g. cameras) have non-contact with the hand. Typical examples of these approaches are marker-based systems, which capture hand movements by tracking the positions of the optical markers/reflectors attached to fingers [146, 147]. In the past decade, advancements in electronics and computer sciences enable more affordable solutions with cameras and fiducial markers e.g. ArUco marker [148]. One ArUco marker can provide both the spatial position and orientation of the marker based on a 2D image projection. A recent study [149] on measuring the rotation angle of a robot finger indicated that the repeatability error of using ArUco markers was comparable to that of using IMU modules. In addition to the marker-based systems, many marker-less hand tracking systems, which utilized large databases and machine learning algorithms, were developed recently [150, 151, 152].

They can achieve around 10-50 mm accuracy in hand pose estimation. However, the effectiveness of such systems highly depends on the quality of the associated database captured by other motion-capturing systems [151].

In this study, we present a low-cost vision-based tracking system to continuously measure the rotation angles of all finger joints during different types of movements. The aim of the research is to find the best practice for the setup of the system and the data processing methods. The remainder of this paper is arranged as follows. In Section 2, the hardware of the proposed system is introduced. Section 3 elaborates on the data processing process with a focus on identifying the orientation of the markers. In Section 4, we present details of the proposed three methods. Then, the repeatability errors and the measurable range of one camera are reported in Section 5, followed by the results of the experiments with a wooden hand and the experiments on tracking hand movements. Section 6 discusses the results and the use of the proposed system. Finally, a short conclusion is drawn.

5.2. THE SETUP OF THE TRACKING SYSTEM

The proposed system utilized 5 cameras (Brand: GoPro Hero 9) to locate and track ArUco markers as Fig. 5.1. Forty ArUco markers [148] were stuck at the dorsal side of the right hand of the subject. Centered on the hand to be tracked, cameras were positioned towards the hand along a virtual semicircle with a diameter of approximately 500 mm. Instead of using static images, we utilized 30 fps 5K videos to record hand movements. Detailed settings of the videos are listed in Table 5.1. To minimize possible errors introduced by lens distortion, all cameras were calibrated individually with a 12x9 checkerboard before data acquisition. In the calibration process, we positioned the board at different distances and inclination angles regarding the image plane of the camera to cover the envelope of the field of view of the camera.
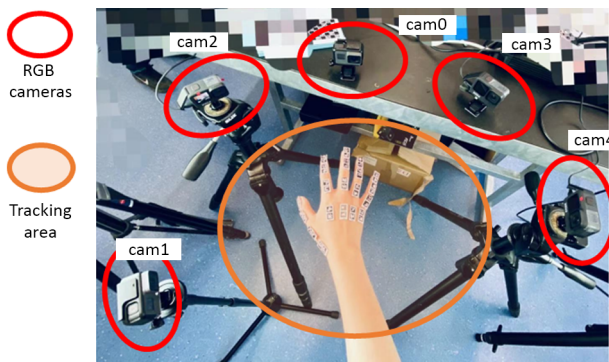
Figure 5.1: The setup of the tracking system.

The ArUco markers were generated using the 4x4 ArUco dictionary. The markers were printed on 300-gram thick paper using an inkjet printer to promise a flat surface during the movements and avoid reflections. The approximate size of each

Table 5.1: The setting of the RGB cameras.

Resolution:	5K (5120x2880 pixels)	Frames per second:	30 fps
Field of View:	Wide	Bit rate:	High
Shutter speed	1/60	Sharpness:	Medium
ISO min:	100	ISO max:	400

marker was 9x9 mm, and this size was selected through several pilots with different participants and the anthropometry database [153]. The forty markers were grouped into 20 pairs following a linear alignment strategy [120], where each pair of markers represents a corresponding segment of the skeleton model in Fig. 5.2(c). Here, the x-axes of the markers are strategically placed towards the distal direction of the hand, hence the markers on each finger are approximately aligned along the axis of the finger as Fig. 5.2(a) and 5.2(b). With the positions and orientations of detected markers, rotation angles between finger segments can be calculated. We extracted the flexion-extension (flx-ext) (as Fig. 5.2(b) angles of all highlighted joints in Fig. 5.2(c) and the radial–ulnar (rad-uln) angles (as Fig. 5.2(a)) of the joints with solid circles in Fig. 5.2(c). Here, although the MPJ for thumb has two DOFs in most kinematic models, only the flx-ext movement is presented in the results.
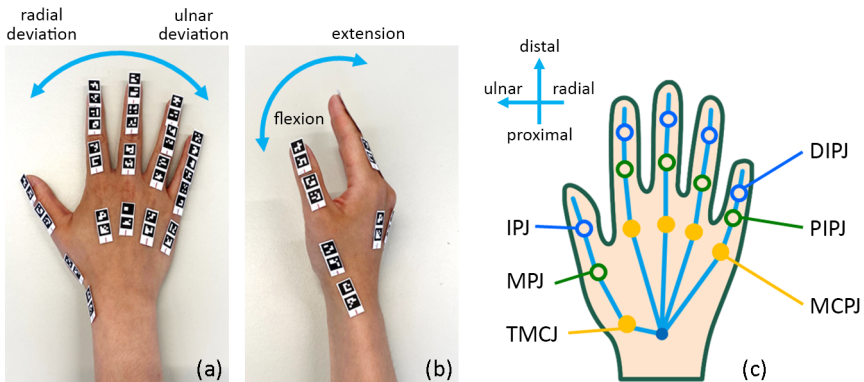
Figure 5.2: Marker placement on the hand. (a) Top view; (b) Side view; (c) The skeletal model of the right hand. Note: rad- radial direction, uln – ulnar direction, flx – flexion, ext-extension, IPJ-interphalangeal joint, MPJ-metacarpophalangeal joint, TMCJ-basal carpometacarpal joint, DIPJ-distal interphalangeal joint, PIPJ-proximal interphalangeal joint, MCPJ-metacarpophalangeal joint.

5.3. Data processing

5.3.1. The workflow

Figure 5.3 presents the workflow of data processing, along with the usage of the positions and orientations of the detected markers. The videos from different cameras

are synchronized first based on their audio streams. Then using OpenCV, the ArUco library, and the adjusted marker size, the positions and orientations of the detected markers in all frames of each video are extracted regarding the corresponding camera coordinate system (CCS). By inter-calibration, all camera coordinates are associated with a reference coordinate system (RCS) and identify the correct orientation in two possible solutions of each marker. After this, the joint rotation angles are calculated using the three proposed methods. The pos-based and orient-x-based method first gathers all detected marker positions and orientations of a frame in the RCS and calculates the angles between two corresponding spatial vectors of a joint. Differently, the orient-mat-based method first calculates the Euler angles with the detected orientations in each CCS, and then, synthetizes all angles identified in different videos regarding each joint.
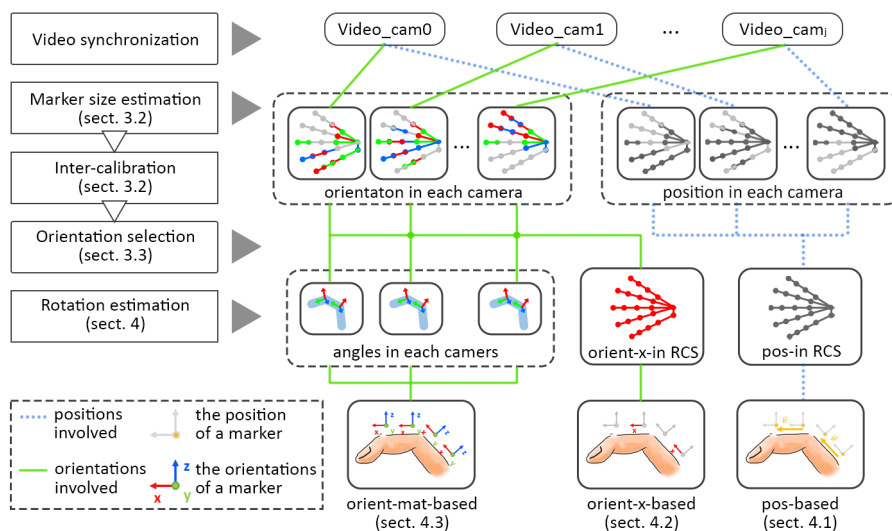
Figure 5.3: The workflow for data processing and the usage of marker positions and orientations.

5.3.2. MARKER SIZE ESTIMATION AND CAMERAS INTER-CALIBRATION

Before each experiment, extra videos of an 8x10 ChArUco board were taken for marker size estimation and inter-calibration. The board included markers of the same size as the markers used for hand tracking, and the board was moved to fill the envelope of the tracking with different inclination angles. After video synchronization, the positions of the markers on the board were then employed to identify marker sizes for each camera and identify the transformation matrices among cameras.

The marker size, defined as the width of the square pattern, is essential in the estimation of marker positions. Since the intrinsic properties vary among cameras, a distance measured in reality may be different from the distance measured in the CCS. Thus, the distances between two horizontally adjacent markers on the board

were measured by a Vernier caliper and computed based on the marker positions extracted from the video of each camera. Then, the marker size can be retrieved when the mean values of these two types of distance are almost the same, and this process was repeated for all cameras. Based on the identified marker sizes, the positions of the markers are computed for inter-calibration and further processes.

To identify the transformation matrix between a camera and the RCS, the detected marker positions $p_{i,j}^k$ was compared with the corresponding marker positions $p_{i,j=RCS}^k$ (if any). In our setup, cam 2 in Fig. 5.1 was selected as the reference camera, and its coordinate system was then the *RCS*. The transformation matrix from the jth CCS (including translation T_j and rotation parts R_j) to the RCS can be found by solving Eq.5.1 using the singular value decomposition (SVD):

$$R_j, T_j = \operatorname*{argmin}_{R,T} \sum \|(R_j^{'} * p_{i,j}^k - T_j^{'}) - p_{i,j=RCS}^k\| \tag{5.1}$$

where $p_{i,j}^k$ is the positions of the marker with index i at the kth synchronized frame in the jth CCS; T_j and R_j are the optimal translation and rotation part of the transformation matrix. Using the transformation matrix, the transformed position $p_{i,j}^k$ in the RCS of position $p_{i,j}^k$ was calculated using Eq.5.2:

$$P_{i,j}^k = R_j * p_{i,j}^k - T_j \tag{5.2}$$

5.3.3. Marker orientation selection

By analyzing the images of the videos frame by frame, the spatial orientations of the detected markers were extracted along with the positions. In the process of identifying the orientations of detected markers, there might be ambiguous results due to the optical illusions [154]. In short, there are two possible solutions in the estimation of a 3D cube from a 2D quadrilateral. Though both can be obtained using the PnP solver, only one of them is the desired solution. This leads to problems in extracting the desired orientations, and it is especially difficult when the optical axis of the camera is close to the normal direction of the marker(s). Before the involvement of manual selections, we utilize the rotation part of the transformation matrices R_j identified in Eq.5.1, and two algorithms, **Algorithm 1** and **2**, to assist the selection procedure. The algorithms are explained with a simplified example shown in Fig. 5.4, where the x-axis stands for time frames, and the y-axis is the number of cameras that detect a marker $i = i_0$ at each frame $k = 0...k_0...l$.

Algorithm 1 uses the information in the synchronized frame gathered by any two cameras to help the selection. First, all the possible solutions of z-axis orientations $oz_{i,j}^{k,u}$ are transformed to RCS as $OZ_{i,j}^{k,u} = R_j * oz_{i,j}^{k,u}$. Here i, j and k are the same as Eq.5.1 and $u = 0$ or $u = 1$, which implies the two possible solutions. For any aligned frame, when a marker is visible by multiple cameras from different viewing angles, two possible solutions $oz_{i,j}^{k,u=0}$ and $oz_{i,j}^{k,u=1}$ of the ith marker in the jth camera at the frame k are compared with that of other cameras and form $4(n-1)$ (pairs) possible
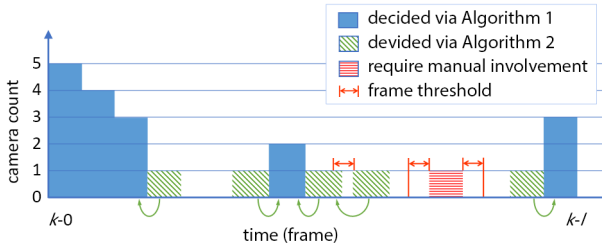
Figure 5.4: An example of a marker $i = i_0$ detected by different number of cameras regarding consecutive frames.

combinations. Here n is the number of cameras that detect this marker at the synchronized frame. In practice, n is often 2 or 3 in the proposed setup. Among these different combinations, the solution of the jth camera that leads to the least angular difference among the possible combinations is considered as the desired solution. With Algorithm 1, the solutions of a marker detected by multiple cameras, i.e., the blue areas in Fig. 5.4 and K_1 in the algorithms are determined. The set U, which notes the selected u value, is updated. K_2, which is the output of Algorithm 1, retains the undetermined frames, and the marker of these frames are visible by only one camera, such as the green and red areas in Fig. 5.4.

Algorithm 1

Input:	Inter-calibration matrix T_j ,
	the possible z-axis orientation $\{oz_{i,j}^{k,u}, k = 0,1,\dots,l, u = 0 \text{ or } 1, i = 0,1,\dots,m, j = 0,1,\dots,n\}$,
	$oz_{i,j}^{k,u} = NA$ if marker was not detected
Output:	$K1$, frames with u selected
	$K2$, frames with u undecided
	$U = \{u_{i,j}^k \mid u = 0 \text{ or } 1, for \ any \ i,j,k\}$, set of selected u
Process:	**For** any i, j, k, u: $OZ_{i,j}^{k,u} = R_j \cdot oz_{i,j}^{k,u}$
	Loop k, i, j:
	$\quad k_0 = k, i_0 = i, j_o = j$
	$\quad$ find $\{j \mid OZ_{i=i_0,j=j_0}^{k=k_0,u} \neq NA\}$ and build set $zj = \{j\}$
	$\quad$ **If** $length \ (zj) \geq 2$:
	$\quad\quad u_{i=i_0,j=j_0}^{k=k_0} = \underset{u=0,1,j\in(zj)}{argmin} \ \left\{arccos\left(OZ_{i=i_0,j=j_0}^{k=k_0,u}, OZ_{i=i_0,j\neq j_0}^{k=k_0,u}\right)\right\}$
	$K1_{i,j} = \{k \mid$ where u is selected$\}$
	$K2_{i,j} = \{k \mid$ where $oz_{i,j}^{k,u} \neq NA$ and $k \notin K1_{i,j}\}$

Based on the information of each camera itself, **Algorithm 2** was applied to select the desired solution for K_2 along the time frame based on the decision of K_1. The solutions were decided by comparing the two possible z-axis orientations of a marker in any undecided frames in K_2 with the determined z-axis orientation of this marker in the nearby frames in K_1. Similar to Algorithm 1, the solution with the least angular difference was taken as the desired solution, as a similar motion status was expected

within a threshold of 15 frames (approx. 0.5 s) regarding the practical movement speed. By iterating this procedure for all undetermined frame sets K_1, K_2 and U are updated automatically. Then, the solution of frames as the blue and green areas in Fig. 5.4, were also decided. However, manual effort was still required for situations such as the red area in Fig. 5.4, where no extra information can be compared neither with other cameras nor within a credible range of frames.

Algorithm 2

Input:	$\{oz_{i,j}^{k,u}, k = 0,1,\dots,l, u = 0 \text{ or } 1, i = 0,1,\dots,m, j = 0,1,\dots,n\}$ $(oz_{i,j}^{k,u} = NA$ if not found$)$,
	$K1$, frames with u selected; $K2$, frames with u undecided, $U = \{u_{i,j}^{k} \mid u = 0 \text{ or } 1, \text{for any } i,j,k\}$,
	δ = frame threshold
Output:	$U = \{u_{i,j}^{k} \mid u = 0 \text{ or } 1, \text{for any } i,j,k\}$
Process:	**If** $K2_{i=i_0,j=j_0} \notin \emptyset$:

      Loop i, j:

        $i_0 = i, j_o = j$

        For each $k_0 \in K2_{i=i_0,j=j_0}$)

          $K_{i=i_0.j=j_0}^{nearby} = [\max(0, k_0 - \delta), \min(k_0 + \delta, l)]$

          If $refK_{i=i_0,j=j_0}^{k=k_0} = (K_{i=i_0.j=j_0}^{nearby} \cap K1_{i=i_0,j=j_0}) \neq \emptyset$:

            $u_{i=i_0,j=j_0}^{k=k_0} = \underset{u=0,1,j=j_0}{\operatorname{argmin}} \left\{ \arccos\left(OZ_{i=i_0,j=j_0}^{k=k_0,u}, OZ_{i=i_0,j=j_0}^{k\in refK, u\in U} \right) \right\}$

            Add $k = k_0$ to $K1$ where $i = i_0, j = j_0$

            Delete $k = k_0$ from $K2$ where $i = i_0, j = j_0$

        Else manual involvement

5.4. ESTIMATION OF JOINT ROTATION ANGLES

5.4.1. THE POS-BASED METHOD

The pos-based method utilized the positions of detected markers in synchronized frames of the videos from different cameras and transformed all camera coordinates to the RCS. Based on the transformed positions of each marker $P_{i,j}^{k}$, a simplified hand skeleton was constructed and the joint rotation angles regarding the initial position of the hand were calculated. Marker positions detected in each camera were transformed to the RCS and plotted in different colors in Fig. 5.5(a). The mean values of each corresponding marker, $\overline{P}_i^{k} = \Sigma_j P_{i,j}^{k}/n$ (n indicates the number of cameras that capture this marker) were used to construct a hand skeleton at the kth frame, as Fig. 5.5(b). Then, a vector constructed by the two paired markers, $V_{seg} = \overline{P}_{dis}^{k} - \overline{P}_{prx}^{k}$, represented the corresponding finger segment, pointing from the proximal to the distal direction. The vectors of the 3rd and 4th metacarpals, V_{m3} and V_{m4}, as highlighted in Fig. 5.5(c), were used to establish the coordinate system of the hand (CS_{hand}) [10] for determining the rotation direction, and the origin of CS_{hand} was the position of the proximal marker of the 3rd metacarpal segment as Fig. 5.5(d). The x-axis of CS_{hand} is the unit vector of V_{m3}, the z-axis is the unit vector of the cross product of V_{m4} and

V_{m3}, and the y-axis is the unit vector of the cross product of z-axis and x-axis.
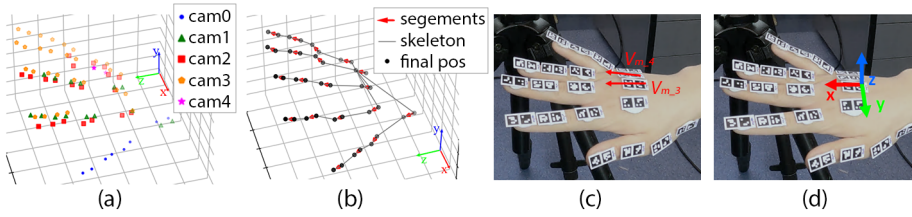
Figure 5.5: The process of extracting hand skeleton (a: marker positions, b: skeleton), and constructing the hand coordinate (c,d).

Based on the CS_{hand} and the found vectors of each finger segment $V_{seg}, seg \in handskeleton$, the flx-ext and rad-uln rotation angles can be calculated using Eq.5.3. In the equation, the direction of the rotation angle is decided by comparing the cross vector of the two segments with a reference vector V_{ref}, which is the y-axis of CS_{hand} for flx-ext angles and the z-axis of CS_{hand} for rad-uln angles.

$$\theta = \text{signum}((V_{prx} \times V_{dis}) \cdot V_{ref}) \, arccos(V_{prx} \cdot V_{dis}) \tag{5.3}$$

5.4.2. THE ORIENT-X-BASED METHOD

The orient-x-based method estimated joint rotation angles based on the transformed x-axis orientation of the detected markers. Different from the pos-based method, this method directly applied the x-axis orientations of detected markers as the vector representing the finger segments, as illustrated in Fig. 5.6. In practice, we used the x-orientation of the proximal marker in the pair. Therefore, information on only half of the markers was needed.
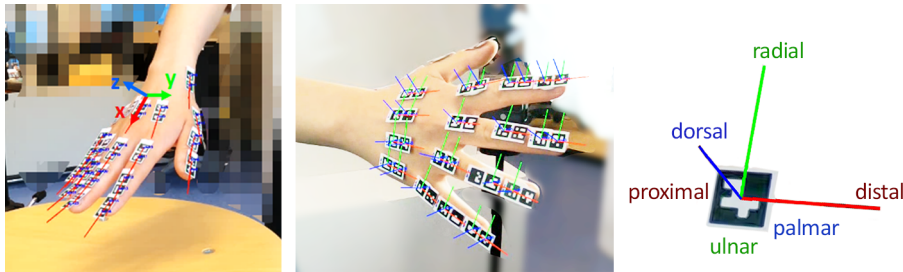
Figure 5.6: The x-axes (the most left) and the orientation (the right two) of each detected marker for each finger segment.

Given $ox_{i,j}^k$, which is the x-axis orientation of the ith marker in the k_{th} frame in the jth CCS, it was first transformed to the RCS by $OX_{i,j}^k = R \cdot ox_{i,j}^k$. The mean orientation $\overline{OX}_i^k = \Sigma_j OX_{i,j}^k / n$ was used to calculate the rotations, where n is the number

of cameras that detect this marker. Same as the pos-based method, the x-axis orientation of the 3rd and 4th metacarpal is applied to construct the CS_{hand} as shown in Fig. 5.6. Afterward, the x-axis orientations of two adjacent finger segments are used to compute the rotation angles following Eq.5.4. The rotation direction is decided by comparing the $V_{ref} = y-axis$ of CS_{hand} and $C_{ref} = z-axis$ of CS_{hand} for the flx-ext and the rad-uln angles, respectively.

$$\theta = \text{signum}((OX_{prx} \times OX_{dis}) \cdot V_{ref}) \; arccos(V_{prx} \cdot V_{dis}) \tag{5.4}$$

5.4.3. THE ORIENT-MAT-BASED METHOD

Different from the orient-x-based method, the orientations of all three axes of detected markers were used in the orient-mat-based method. In practice, we adopted the orientation of the proximal marker in the pair to represent the orientation of the corresponding finger segment $om_{i,j}^k$, where i, j, and k are the same as the last section. Figure 5.6 presents the $om_{i,j}^k$ of the markers at their positions. Here, the x-axis of the marker points from the proximal to the distal side, y-axis points from the ulnar to the radial side, and z-axis points from the palmar to the dorsal side.

Instead of transforming to the RCS, the orientations detected in each CCS were directly used to estimate the joint rotation angles. A rotation matrix R^m was identified between the orientations of two adjacent finger segments $om_{prx,j}^k$, and $om_{dis,j}^k$ as:

$$R^m = om_{dis,j}^k (om_{prx,j}^k)^{-1} = \begin{bmatrix} a_{00} & a_{01} & a_{02} \\ a_{10} & a_{11} & a_{12} \\ a_{20} & a_{21} & a_{22} \end{bmatrix} \tag{5.5}$$

Based on Eq.5.6 and the methods described in [155, 111], Euler angles (β, γ, α) were calculated following Y-Z-X sequence as:

$$\beta = arctan\left(\frac{a_{02}}{a_{00}}\right), \gamma = arcsin(-a_{01}), \alpha = arctan\left(\frac{a_{21}}{a_{11}}\right) \tag{5.6}$$

where β, γ, α correspond to the rotation of flx-ext, rad-uln, and self-rotation (pronation-supination) of the joint, respectively. Then, the final rotation angles of each joint were computed as the mean of the rotation angles of this joint identified by any cameras as $\alpha, \beta, \gamma_{joint}^k = \Sigma_j \alpha, \beta, \gamma_{joint}^k / n$, where n indicates the number of cameras that are able to identify the rotation angle of this joint.

5.5. EXPERIEMENTS

This section first presents the calibration result of the proposed system, followed by the setups and the results of an experiment conducted on the platform of a milling machine. This experiment investigated the accuracy, repeatability, and measurable range using one camera. Then, five cameras were employed to track a wooden hand with fixed joints to study the difference between the measurement results of using a goniometer and using the three proposed methods. Lastly, with the proposed system,

the joint rotations of three participants in performing a continuous hand movement were analyzed.

5.5.1. Camera calibration results

An average of 153 images were used to identify the lens distortions of each camera, and the projection errors were about 0.088 to 0.102. Five cameras were adopted, and one of the cameras (cam 2 in this study) was chosen as the reference. The mean values $\overline{P}_{i,j}^{k}$ and $\overline{OX}_{i}^{k}$ were calculated from the gathered information in the RCS, and they were compared with transformed positions $P_{i,j}^{k}$ and x-axis orientations $OX_{i,j}^{k}$ of each camera, respectively. The number of registrable points and the mean differences of these points and the orientations of markers are listed in Table 5.2.

Table 5.2: The distance/deviation of detected markers in inter-calibration; mean($\pm SD$).

Resolution:	5K (5120x2880 pixels)	Frames per second:	30 fps
Camera	Registered points	distance difference (pos-based)	angular difference (orient-x-based)
cam 0	22,958	3.91 (±13.07)	2.85 (±3.26)
cam 1	63,016	3.98 (±4.36)	2.23 (±2.37)
cam 2 (ref)	84,351	3.29 (±3.16)	2.40 (±2.46)
cam 3	64,144	2.73 (±4.34)	1.76 (±2.15)
cam 4	19,192	7.59 (±66.43)	2.18 (±5.18)

5.5.2. Accuracy, repeatability, and measurable range

To study the effectiveness of the proposed system, we designed an experiment to investigate the accuracy, repeatability, and measurable range of one camera. Three sets of markers were prepared and each set included seven pairs of markers with different marker sizes. These sizes were measured using a Vernier Caliper. The three sets of markers were placed on a standard metal workpiece, which has three flat surfaces as shown in Fig. 5.7(b). The dihedral angle between the surfaces with Set 2 and Set 3 was 90 degrees. This workpiece was fixed on the rotary table of a milling machine, as shown in Fig. 5.7(a), and the rotary table can be moved along the platform in three directions. Two cameras (one was to assist orientation selection) were placed about 25-30 cm away from the machine to acquire video clips. Only the pos-based and the orientation-x-based methods were used, as the orient-x-based and the orient-mat-based methods utilize the same orientation information from one camera and the difference is mainly in processing such information among cameras.

The first part of the experiment investigated the repeatability when using videos from one camera. The marker Set 1 was set facing toward the cameras, and then the workpiece was translated in a 500 × 200 ×100 mm envelope along three axes, every 3 steps in the camera view, resulting in 27 positions. During the translation, we paused the movement for 10 seconds at each position. After extracting all marker
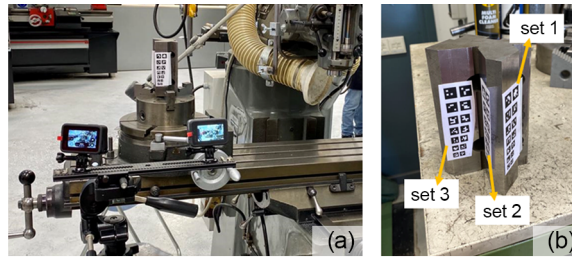
Figure 5.7: Setup of the experiment: (a) the setup on the milling machine, (b) three sets of markers that are attached to the workpiece.

positions and orientations, the x-axis orientation deviations of paired markers were calculated using the pos-based method and the orient-x-based method regarding the x-axis of the camera coordinate, respectively. Theoretically, the angle deviation of each point in these 10 seconds would be zero as both the cameras and the markers were fixed. However, the deviations varied among the marker sizes, as Fig. 5.8 (left), which presents the absolute errors (in degrees) regarding the 7 marker sizes (horizontal axis in the figure). The results of using the orient-x-based method were more stable (MEAN = 2.5 to 3.0, STD = 0.6 to 1.1 degrees) compared to the pos-based method (MEAN = 4.5 to 19.4, STD = 2.6 to 13.1 degrees) which was quite sensitive to the marker size and the errors of small markers were considerably large.
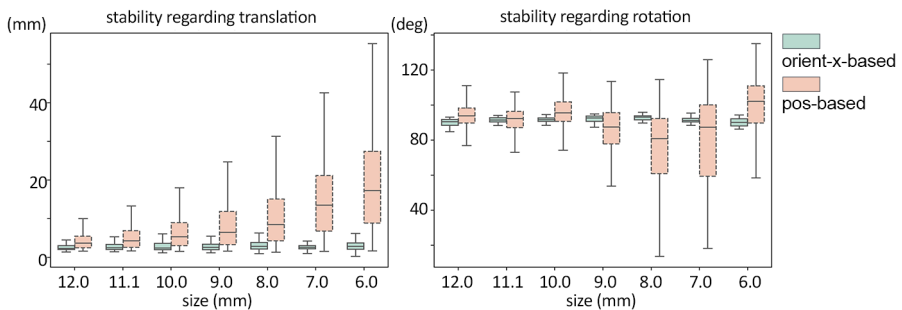
Figure 5.8: (Left) The deviations regarding the size of markers for repeatability investigation. (Right) The deviations regarding the sizes of markers for measuring the angles between Set 2 and Set 3.

The second part evaluated the accuracy of the proposed system. The angles between Set 2 and Set 3 were measured in different positions and angles toward the cameras. For this, the rotary table was moved to the left, medium, and right in the view of one camera along a 500 mm axis. At each position, the workpiece was rotated in a 10-degree step to create different inclination angles regarding the image plane of the camera. The measured angles between Set 2 and Set 3 were expected to be 90 degrees. The mean angles measured using the orient-x-based method were between 90.2 and 92.9 degrees (STD = 1.3 to 2.4 degrees) regarding the marker sizes. In

comparison, the mean angles estimated using the pos-based method deviated much more, even for the markers with a size larger than 9 mm, as presented in Fig. 5.8 (right).

The third part was to find the measurable range of a marker in the view of one camera when the marker was placed in different inclination angles to the image plane of the camera. In this test, the rotary table was placed at the center of the camera view, and the workpiece (with marker Set 1) was continuously rotated 360 degrees while being recorded. Angles between the x-axis of the CCS and the vectors of the 7 marker pairs were computed using the pos-based and orient-x-based methods respectively. The approximate ranges of large markers were slightly larger than the ranges of small markers regardless of the calculation methods, as presented in Fig. 5.9. Considering the results of both methods, the measurable range of a marker in the view of one camera was about 130 to 145 degrees.
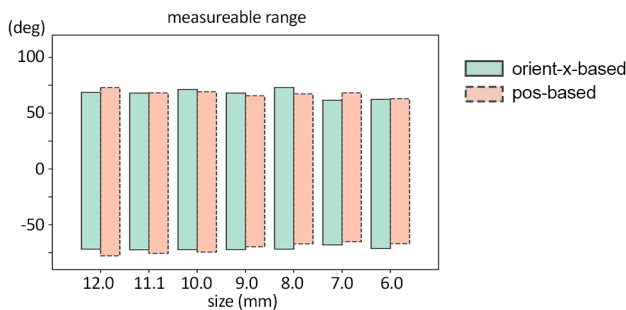
Figure 5.9: Measurable ranges of one camera regarding different sizes of markers.

5.5.3. ROTATION MEASUREMENT OF A WOODEN HAND

Before experiments with participants, a pilot study was conducted with a wooden hand model to measure joint rotations in static poses. Two of the finger joints were fixed, then a researcher held the bottom part of the model and moved it within the envelope of the tracking system. The angles estimated using three proposed methods were compared with the readings from a goniometer. The mean rotation angles of five measurements using the goniometer were around 32 and -15 degrees for the two cases, representing flexion and extension, respectively. The results of the analysis using the three methods are plotted in Fig. 5.10, where the x-axes stand for the frames in the time domain, y-axes are the measured flx-ext angles at the corresponding frames. The mean values were 31.8 ($\pm$6.1) and -15.3 ($\pm$4.1) degrees using the pos-based method; 32.1($\pm$2.8) and -15.5($\pm$0.6) degrees with the orient-x-based method, and 32.6($\pm$1.8) and -15.1($\pm$0.6) using the orient-mat-based method. The mean rotation angles using three methods were close to the readings of the goniometer. However, the standard deviation with the pos-based method was larger than that of using the other two methods. In contrast, the rotations estimated using the orient-x-based and orient-mat-based methods were similar at each frame. Only a slight difference

was observed, and part of the results of case (b) is zoomed-in at the right side of Fig. 5.10.
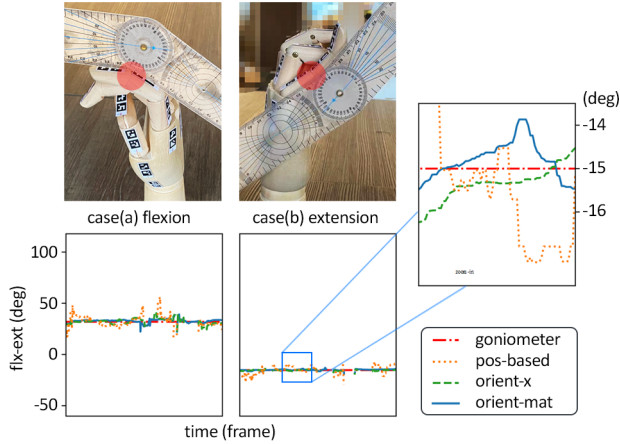
Figure 5.10: The measured flx-ext angles of a wooden hand using the three methods in two cases.

5.5.4. ROTATION MEASUREMENT OF CONTINUOUS HAND MOVEMENTS

The hand movements of three volunteers were recorded and analyzed to evaluate the effectiveness and efficiency of the proposed system and the rotation estimation methods. Participants were instructed to perform a series of movements, starting with the resting pose and then including abduction-adduction of all fingers and flx-ext of all finger joints, as the screenshots in Fig. 5.11. The number of markers detected by each camera and the sum of them are plotted against the video frames in the figure. Most markers can be detected for the first two types of movements; however, the number of detected markers gradually became less during the flx-ext of MCPJ (metacarpophalangeal joint). It was caused by the markers at the distal end of the fingers; when the participant bent those fingers towards the palm, those markers were invisible to either of the five cameras.

The joint rotation angles regarding the resting pose (the initial frame) were calculated using the three methods. The measured rotation of the movement performed by one participant is highlighted in Fig. 5.12, where the 5 columns stand for the five fingers from the thumb to the pinky finger, and each row is in accordance with flx-ext or rad-uln rotation angles of the joints underlined in Fig. 5.2(c). In each sub-figure, the x-axis presents time frames and the y-axis presents the rotation angles in degrees, where the flexion rotation and the radial deviation are in positive values. Measurement results using the pos-based, the orient-x-based, and the orient-mat-based are presented in orange (dotted line), green (dashed line), and blue (solid line) lines, respectively. Comparing the three types of lines, the measured angles using the three methods were mostly comparable, but the abrupt deviation was observed when using the pos-based method. Also, large differences were identified when compar-
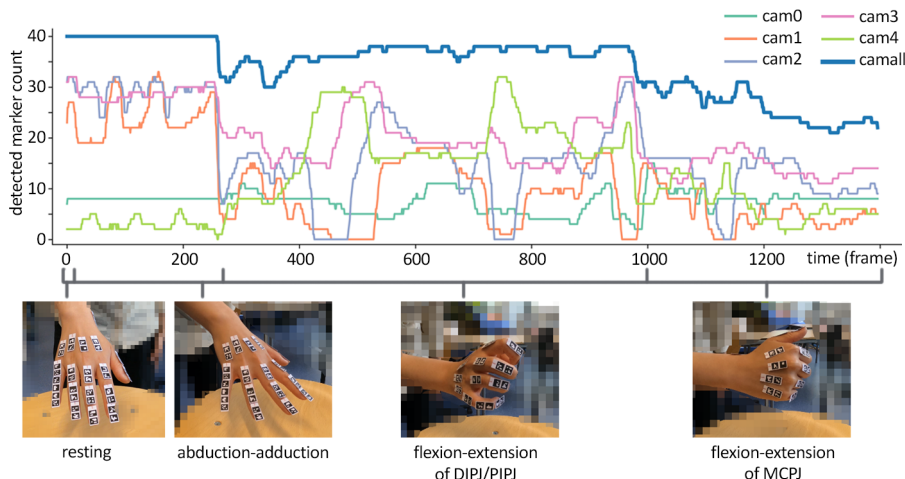
Figure 5.11: The total number of the detected markers corresponding to the movement.

ing the angles calculated using the orient-mat-based method to the results of using the other two methods, as the grey areas in Fig. 5.12. These areas are all related to the joints with multiple DOFs, such as the MPJ (metacarpophalangeal joint) and the CMC-1 (basal carpometacarpal joint) for the thumb and the MCPJ (metacarpophalangeal joint) for the other fingers. Conjectures regarding the differences will be detailed in Section 6.2.
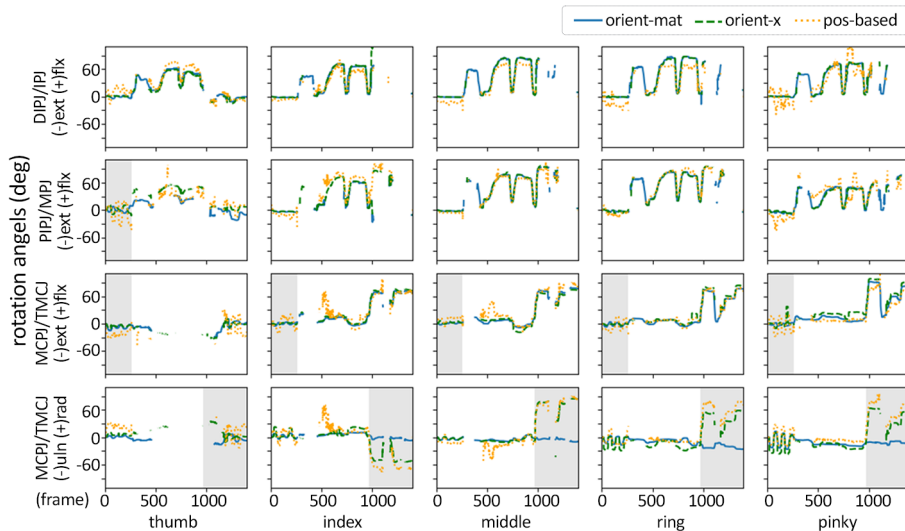
Figure 5.12: Rotation angles of each finger joint regarding time in frames.

Using the orient-mat-based method, we invited more participants to perform the same set of movements. Figure 5.13, which share the same figure structure as Fig. 5.12, presents the results of three participants with hand size around P10, P60, and P40 (based on [153]). The trends of the three lines are different as though they performed the same actions but with different motion speeds and motion ranges.
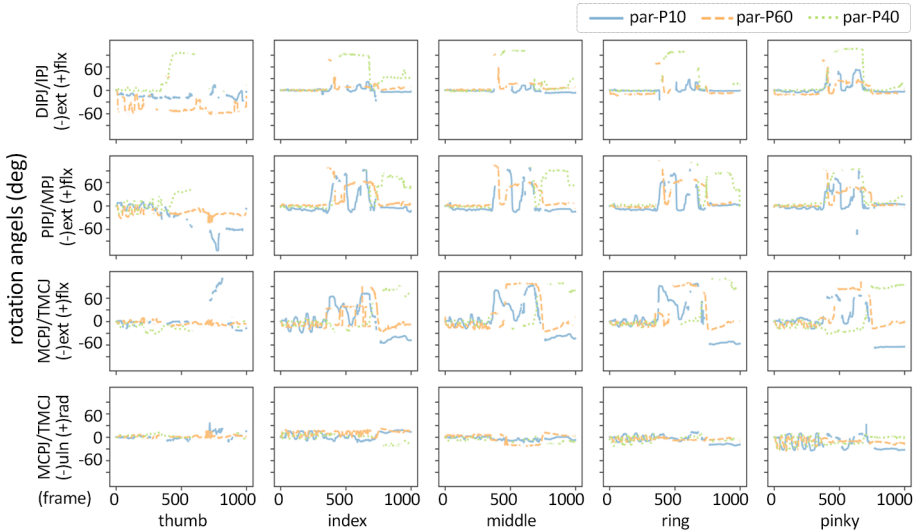
Figure 5.13: Detected rotation angles of hand movements of different participants using the orient-mat-based method.

5.6. DISCUSSION

5.6.1. COMPARISON AMONG THE THREE METHODS

This study proposed a hand-tracking system that utilized five RGB action cameras and ArUco markers to track hand movement and estimate joint rotation angles. Based on the acquired positions and orientations of the markers, we measured finger joint rotations with three methods: the pos-based, the orient-x-based, and the orient-mat-based methods. Comparing the three methods, the latter two have an obvious advantage as they only need half of the number of markers required by using the pos-based method. Other benefits and drawbacks of using each of the proposed three methods are summarized in Table 5.3.

The experiment with the milling machine and the rotary table suggested that the repeatability errors of one camera were about 2.6 to 27.6 (deg) using marker positions, and 0.6 to 2.4 (deg) using detected orientations. The results of using positions are less competitive compared with other tracking systems [137, 138, 139, 140, 143, 144], but the results of using orientations are acceptable as its error was less than 5 degrees, which is a threshold in the evaluation of a tracking system [146] and in the

Table 5.3: A comparison of using the proposed three methods.

	pos-based	orient-x-based	orient-mat-based
Data processing	- 40 markers - requires marker size estimation - may have abbe error	+ less markers (20) + independent from marker size estimation - may need manual involvement	+ less markers (20) + independent from marker size estimation - may need manual involvement
Rotation estimation	+ information of the full skeleton - requires a CT_{hand} + comparable to classical measurements - one DOF rotation	+ information of the full skeleton - requires a CT_{hand} + comparable to classical measurements - one DOF rotation	- measurable range of one camera + no need of a CT_{hand} - may be different to the classical measurements + apply to more scenarios

studies of gait [156].

Considering the results of all the experiments, using the pos-based method often resulted in larger deviations than using the other two methods. There are three conjectures and two of them relate to the processes of estimating the marker sizes and inter-calibration among cameras. The estimation of marker size is critical to extract the correct marker positions, and small errors may introduce large deviations to the follow-up steps, e.g., inter-calibration, and hand skeleton construction. On the contrary, the rotation estimation using the orient-mat-based method is independent of the marker size estimation and inter-calibration. Another conjecture is the abbe error. The length and breadth of finger segments limit the marker size and the distance between the paired markers, thus, any errors in the position estimation could introduce large angular deviations.

5.6.2. Differences of the rotation estimation

The angles estimated using the three methods were similar in most cases as present in Fig. 5.12. However, differences were found in the grey area in Fig. 5.12, where the angles estimated using the orient-mat-based method are distinct from the angles extracted by the other two methods. Also in these areas, the absolute values of the angles calculated using the orient-x-based and the pos-based methods are equal to the absolute angles of the corresponding frames in another type of movement (e.g. the absolute rad-uln angles of MCPJ/CMC-1 after frame 1000 are the same as the absolute flx-ext angles of these joints). The rotation angles calculated by the pos-based and the orient-x-based methods are the angles between two corresponding vectors in 3D, while the rotation angles estimated using the orient-mat-based method are the Euler angles; and these two types of angles are different mathematically. A previous paper [157] discussed that only using vectors to estimate three-dimensional joint

rotations can lead to errors because this calculation method relies on the assumption that the joints only have one DOF, which is not always true for all finger joints. This can be proved by the fact that the grey areas always occur with the joints with multiple DOFs, e.g. MCPJ, TMCJ, and MPJ. Although using the vectors to estimate rotations is theoretically following the same strategy of measuring the rotations with goniometers, which measures the joint rotation by placing the two sides of the meters along with two finger segments, respectively [158], it is unable to automatically classify the flx-ext rotation and rad-uln deviation into the correct movement type. Then, the estimated result includes the rotations caused by both flx-ext and rad-uln deviation, e.g., thumb opposition movement. On the contrary, using the orient-mat-based method can still be applied in this case, as it extracts Euler angles of the rotations of three axes to classify three types of movements: flx-ext, rad-uln deviation, and self-rotation. Thus, we suggest using the Euler angles for rotation estimation.

5.6.3. LIMITATIONS

In the experiments with participants, it was observed that markers rotated along the distal-proximal axis as connective tissues cause the deformation as presented in Fig. 5.14(c,d). This can introduce measurement error, especially for self-rotation. Theoretically, this has no/less influence on using the pos-based and the orient-x-based methods, the self-rotation angles can only be calculated using the orient-mat-based method. A better placement strategy will be explored to reduce such effects.

The proposed system successfully measured joint rotation angles continuously using the RGB cameras and ArUco markers, but the two issues of using a vision-based system still exist: occlusion and the noise of the environment [159]. For instance, for the first posture in Fig. 5.14(a), markers representing the distal phalanges are fully covered by the palm and were invisible by any of the cameras. Thus, information on this part was missing. Another example was the scenario shown in Fig. 5.14(b), where background noise confused the marker detection algorithm. Extra lighting was introduced to improve the detection results, but misdetection was still observed especially for markers with simple patterns, and light reflections on the markers may also lead to the loss of the detection. For the latter issue, we printed the markers with an inkjet printer to minimize the reflection. The influence of marker pattern complexity will also be studied in the future.
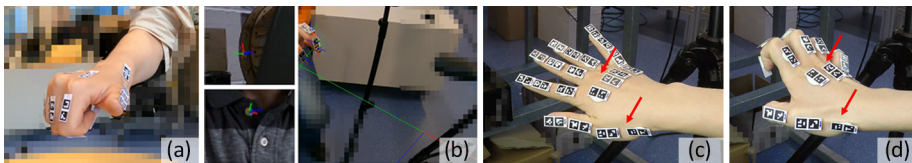
Figure 5.14: Senarios that influence marker detection: (a) the occlusion situation when markers on the distal segments were fully covered; (b) noise in the background and the fault in the detection of markers.Screenshots of the videos without (c) and with (d) extensor digitorum tendons deformation.

5.7. CONCLUSION

In this paper, we proposed a low-cost camera system to measure finger joint rotation angles using ArUco markers. Three methods namely the pos-based, the orient-x-based, and the orient-mat-based methods, were implemented to extract the rotation angles. The first two methods calculate the joint rotations as the angles between two corresponding vectors in the RCS. For the third method, the joint rotations were identified first as the Euler angles between the orientations of two bone segments in the coordinate system of one camera, and then the results of all cameras were synthesized regarding each joint. Experiment results with one camera suggested that using the marker orientation was more stable as the repeatability error was comparable with previous studies using motion capture systems, sensor-based devices, or goniometers. In the use of multiple cameras, the orient-mat-based method outperformed the other two methods regarding both efficiency and reliability, as it is independent of the results of marker size estimation and inter-calibration. Also, this method can be applied to more practical scenarios as it describes the joint rotations in a more appropriate manner. Considering the quality of the results and efficiency of the process, we recommended the orient-mat-based method as a best practice for measuring hand joint rotation angles with action cameras and ArUco markers.

5

6

RANGE OF MOTION FOR FINGER JOINTS

This Chapter presents the joint rotation measurement of finger joints using an optical tracking system that recorded joint movements simultaneously. The goal is **to compare the range of motion (ROM) of finger joints during active, functional, and passive movements**. Hyperextension was observed during functional activities, whose motion range exceed the active ROM, especially during fine manipulations. The chapter tackles the investigation of three types of ROM that are essential to the design of an implant replacement.

This chapter is based on the article in Book "Convergence: Breaking down Barriers between Disciplines" [160].

6.1. Introduction

Range of motion (RoM) is one of the fundamental measurements for studying the biomechanics and kinematics of finger joints [161]. This understanding is crucial to the pathology study and treatment designs for related diseases. However, the significant flexibility of hand fingers challenges the measurement and the study on these joints. There are three types of RoM: active, passive, and functional RoMs (A-RoM, P-RoM, F-RoM). A-RoM presents the maximum motion range when the participants perform movements without any assistance; P-RoM is similar to the active one, but it covers the maximum motion range when the participants perform movements with an external force; F-RoM refers to the motion range for the participants to perform a spectrum of activities of daily living.

A great number of articles measured the RoMs of hips and knees during active or loading scenarios [162, 163], and these studies have contributed to the improvement of the designs of hips and knees implant replacements [164, 165, 166]. On the contrary, limited literature reported the measurement of finger joint RoM, and only several of them compared the A-RoM with either F-RoM or P-RoM [167, 168, 158, 169, 145]. These studies adopted different study protocols and measuring tools. For example, an early study measured the A-RoM and P-RoM of the index to small fingers using a goniometer [167], and recent studies applied a data glove to collect continuous data of finger joints during active and functional hand movements [169, 145]. Most studies concluded that the F-RoM was within the range of the A-RoM [158, 169, 168], but one of them mentioned that joint extension exceed the A-RoM in some moments of functional activities [169].

For a more comprehensive understanding of the RoMs of finger joints, this study aims to challenge the conclusion drawn from current literature by comparing the A-RoM, F-RoM, P-RoM of finger joints. Using an optical tracking system, we continuously measure the rotation angles of target joints continuously during hand activities. Considering the conclusion in previous studies, the initial hypothesis is: the F-RoM is smaller than the A-RoM, and the P-RoM covers the other two RoMs. Since not all three RoMs are combined in one study previously, the present study investigates all three ranges to evaluate the hypothesis.

6.2. Method

6.2.1. Measuring system

To acquire continuous data on joint rotation angles through hand activities, we used an optical tracking system with an accuracy of 2.7 degrees and a repeatability of 0.8 degrees [116]. One part of the system consisted of five RGB cameras (GoPro Inc., San Mateo, CA, USA) which were distributed around the tracking area, as Fig. 6.1(a). All the cameras were in wide-view mode with 5K (3280x2250) resolutions and 30 fps (frame per second). The other part of the system consisted of 20 printed ArUco markers attached to the dorsal side of finger segments. ArUco markers are a type of fiducial marker, which enables researchers to extract the orientation and the position of each

marker in the camera coordinate system from a 2D image [148], and thus to track the movement of each finger segment. The markers were prepared in three sizes: 7.0 mm, 8.6 mm, and 10.0 mm, for different hand sizes [153]. During the participation, all markers were coarsely aligned by placing the x-axis of the markers pointing to the fingertips as Fig. 6.1(b): each marker represented a finger segment.
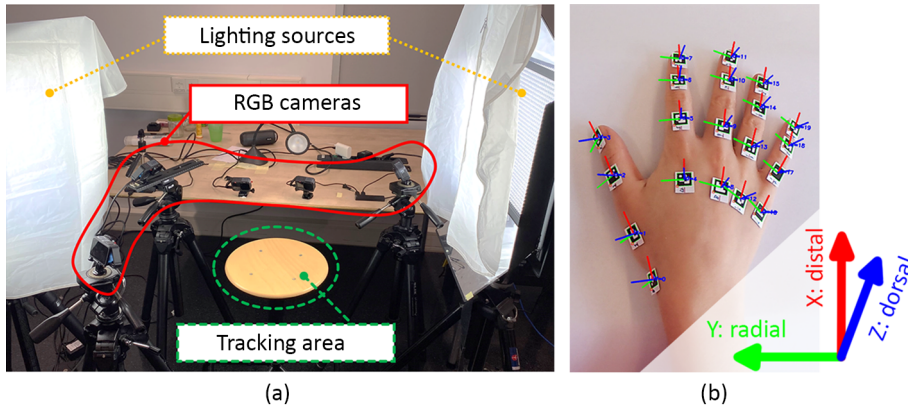
Figure 6.1: The applied tracking system. (a) the setup of the cameras and lightening; (b) the marker placement and the corresponding local coordinate system.

6.2.2. Study protocol and RoM definition

This study included 20 participants (10 males and 10 females) without a history of hand disability or hand surgery. The average age was 31 years (range 21-59 years old). The Human Research Ethical Committee of the Delft University of Technology approved this study. All participants signed the consent form before their participation and indicated their right hand as the dominant hand. The sample size was calculated for the two-tailed Wilcoxon signed-rank test (matched pairs) with an effect size of 0.8 and power of 0.9, and this sample size also affects the one-tailed test with an effect size of 0.8 and power of 0.95 [170].

After attaching the markers, participants performed a set of actions in Fig. 6.2. The figure illustrates some critical postures for the active and passive activities, as well as some potential postures for the functional activities. Action (A1) – (A4) measures the A-RoM, including radial-ulnar (rad-uln) deviation of all fingers, and flexion-extension (flx-ext) of all finger joints. In these actions, we guided the participants to actively bend or rotate their fingers as much as they can. Action (P17) – (P19) also include similar movement but with an external force applied on the fingers. These actions correspond to the P-RoM. We instructed participants to press the finger segment by themselves and increase the force gradually to the maximum that they can accept to avoid any pain or injury during their participation. Lastly, twelve daily activities were measured for the F-RoM. After comparing the included activities in previous literature [158, 169, 168, 145, 171], action (F5) – (F12) and (F14) – (F15) were

selected to cover the most frequent grasp activities in daily life [98]; besides, action (F13) and (F16) represents non-prehensile actions [1]. With the rotation angles of all frames, each type of RoM was defined with the extreme rotation angles of the corresponding actions; from the minimal to the maximum values of the rotation angles.
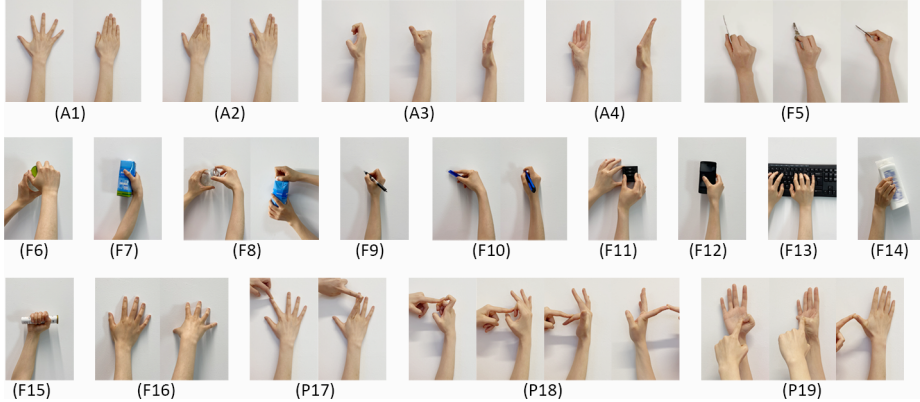
Figure 6.2: Illustrations of included activities. Action (A1) – (A4): active activities, action (F5) – (F16): functional activities, action (P17) – (P19): passive activities.

6

6.2.3. Rotation calculation

We first calculated the rotation of target joints by extracting the 3D orientations of each marker frame by frame with a self-developed Python program and the OpenCV Library [116]. These detected orientations served as the local coordinate system (LCS) of the corresponding finger segments. The analysis included 18 joints: distal interphalangeal joint (DIPJ), proximal interphalangeal joint (PIPJ), metacarpophalangeal joint (MCPJ), and carpometacarpal joint (CMCJ) of index to small fingers; interphalangeal joint (IPJ), metacarpophalangeal joints (MPJ for thumb), and trapeziometacarpal joint (CMC-1) of thumb. Colored markers in Fig. 6.3(a) represent the joints, and the squares with numbers indicate the markers of the corresponding finger segment. The rotation estimation of a joint was based on two adjunct LCSs: R_{dis} and R_{prx}, which are for the distal and proximal finger segments. For example, the rotation of the CMC-1 was calculated from R_{dis} and $R_{prx} = R_0$. Note that the calculation of the CMCJ of long fingers was relative to the 3rd metacarpal (marker number: 8) [113]. For example, the rotation of CMCJ-2 used $R_{dis} = R_4$ and $R_{prx} = R_8$. Here, the CMCJs and CMC-1 analyzed in this study were based on the applied simplified kinematic model in Fig. 6.3(b), which is based on but different from hand anatomy.

Knowing the two LCSs, the rotation calculation employed the transformation matrix T in between $R_{dis} = T * R_{prx}$. The rotation angles were the Euler angles following the X-Y-Z sequence as suggested in the ISB [111]. The positive values indicate flexion, radial deviation, and clockwise rotation (see Fig. 6.3b).
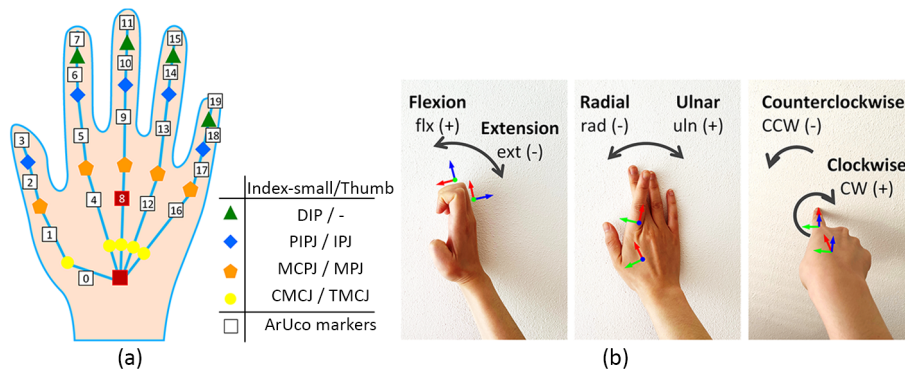
Figure 6.3: (a) The applied simplified hand kinematics model and the corresponding markers. (b) The notation and the descriptions of the rotations along the three axes.

6.2.4. STATISTICAL ANALYSIS

With all three types of RoMs: A-RoM, F-RoM, and P-RoM, the normality of the extreme rotation angles of each range was first examined using the Shapiro-Wilk test. Consequently, the matched boundary values were compared using the Wilcoxon signed-rank (two-tailed) test to investigate if these ranges were different from each other. The null hypothesis was that the extreme rotation angles of any two types of ranges are the same; for example, the maximal flx-ext angles of a joint during active movements is equal to the one during functional activities. Followingly, one-tailed Wilcoxon signed-rank tests were applied to study the relationships among the boundary values. In this study, a P-value smaller than 0.05 was considered statistically significant.

6.3. RESULT

6.3.1. THE MEASURED A-ROM, F-ROM, P-ROM

The extreme values of the three types of RoMs along the three rotation axes had 324 sets of boundary values in total. The normality analysis of these boundary values suggested that 16% of their distribution failed to fit a normal distribution, and thus, Wilcoxon signed-rank tests are applied in the following statistical analysis.

The corresponding extreme values were compared between any two types of RoMs along each rotation axis (the RoMs for CMCJ-3 were excluded since the 3rd metacarpal bone was used as the reference). The two-tailed analysis suggested statistical differences between A-RoM and P-RoM for most joins as expected. Also, the differences were indicated for the flx-ext F-RoM and A-RoM of some joints (see Fig. 6.4).

6.3.2. THE DIFFERENCE AMONG THE THREE ROMS

The differences between any two types of RoMs were calculated to assess the initial hypothesis: max(F-RoM) < max(A-RoM) < max(P-RoM), and min(F-RoM) > min(A-RoM) > min(P-RoM). Table 6.1=6.3 presents the mean (±SD) of all participants; where
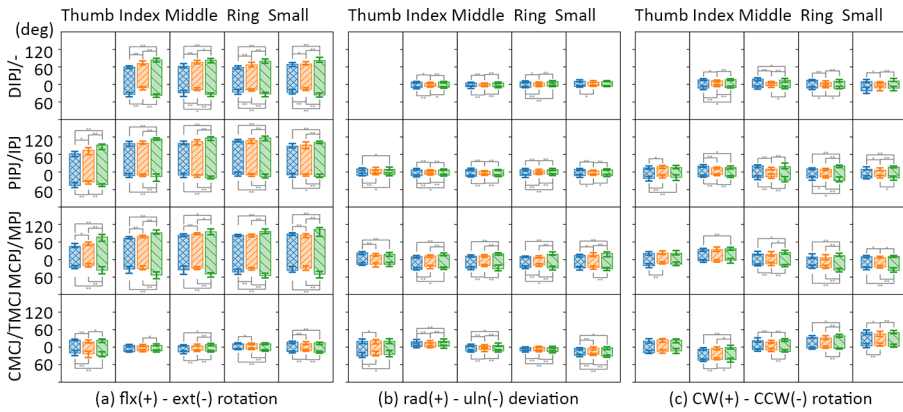
Figure 6.4: The medium, 25, and 75 percentiles of the boundaries of the F-, A-, P-RoM of target joints of all participants, and the result of the two-side matched-pair statistical analysis. (a) flexion-extension rotation; (b) ulnar-radial deviation; (c) self-rotation. Vertical unit: degrees. "CW-CC": clockwise – counter-clockwise; "*","**": the p-value is less than 0.05 or 0.01.

positive values support the hypothesis and negative values contrast the hypothesis. According to Table 6.1, larger F-RoM than A-RoM was found in extension, especially for most DIPJ and IPJ; the difference was about 8 to 20 degrees. Conversely, most differences between maximum boundaries were positive, which meant that the functional flexion range was within the active one. The majority of the rad-uln deviation and self-rotation of F-RoM were larger than the corresponding A-RoM, as most differences were in negative values. The majority of the difference between A-RoM and P-RoM were positive with statistical significance (see Table 6.2). Although little pairs show slightly negative differences, none of them present significance. Similarly, no statistical significance was found in the negative difference in Table 1c.

6.4. DISCUSSION

The goal of this study is to measure and compare A-RoM, F-RoM, P-RoM. The findings partially agree with the initial hypothesis, as the P-RoM was generally the largest motion range among the three and it covers the A-RoM and F-RoM. The measurement in this study showed that our active and P-RoMs were comparable with previous literature [158, 169, 168]; however, our F-RoM is larger than theirs, and our findings invalidate part of the hypothesis that the A-RoM covers the F-RoM.

Apart from the flexion ranges shown in Table 6.1, most differences between the F-RoM and A-RoM suggested that the rotation of hand joints can exceed their active RoM during functional activities in joint extension, rad-uln deviation, and self-rotation; especially the differences were pronounced for the extension of MCPJ and DIP/IPJ. This finding disagreed with the conclusion of previous literature [158, 169, 168]. The definition of the RoMs can affect the results. In some studies, this phenomenon was mentioned, but the extreme values were excluded [158, 169]. Differ-

Table 6.1: Differences between F- and A-RoMs.

	Flexion (Amax-Fmax)	Extension (Fmin-Amin)	Radial (Amax-Fmax)	Ulnar (Fmin-Amin)	CW (Amax-Fmax)	CCW (Fmin-Amin)
CMC-1	-4.8 (±6) *	3.0 (±5) *	-2.6 (±5) *	-4.0 (±8) *	2.0 (±7)	-3.1 (±8)
MP-1	6.0 (±9) *	-5.8 (±13)	-6.9 (±8) *	1.0 (±4)	1.5 (±10)	-9.8 (±7) *
IP-1	7.9 (±15) *	-9.6 (±8) *	0.9 (±4)	-4.0 (±6) *	3.9 (±7) *	-7.9 (±7) *
CMC-2	-1.5 (±5)	-1.6 (±3)	-1.6 (±2) *	1.5 (±4)	1.8 (±4)	-5.6 (±6) *
MCP-2	5.1 (±7) *	-4.5 (±17)	0.8 (±6)	-6.6 (±6) *	1.9 (±7)	-0.6 (±8)
PIP-2	4.6 (±11)	-1.4 (±6)	-3.4 (±4) *	-5.3 (±5) *	-6.3 (±8) *	-6.3 (±6) *
DIP-2	11.6 (±13) *	-20.2 (±13) *	-3.1 (±5) *	-4.9 (±6) *	-4.3 (±8) *	-10.0 (±11) *
CMC-3	/	/	/	/	/	/
MCP-3	5.3 (±7) *	-5.7 (±19)	0.6 (±5)	-10.9 (±9) *	-2.2 (±9)	-4.5 (±6) *
PIP-3	2.9 (±9)	1.6 (±8)	-6.1 (±6) *	-5.3 (±4) *	-9.0 (±6) *	-6.3 (±6) *
DIP-3	12.4 (±8) *	-12.4 (±15) *	-2.5 (±5) *	-3.4 (±6) *	-9.8 (±9) *	-3.4 (±9)
CMC-4	-1.3 (±3) *	-1.4 (±4)	1.1 (±2)	-1.5 (±2) *	-2.1 (±6)	-1.5 (±5)
MCP-4	0.7 (±7)	-10.2 (±13) *	-1.5 (±5)	-6.6 (±5) *	-2.1 (±7)	-1.9 (±10)
PIP-4	-0.6 (±10)	2.9 (±6)	-4.5 (±7) *	-8.4 (±9) *	-3.4 (±8)	-4.0 (±7) *
DIP-4	9.8 (±9) *	-8.4 (±9) *	-2.5 (±6) *	-3.7 (±4) *	-7.9 (±7) *	-3.0 (±9) *
CMC-5	-4.4 (±4) *	-4.5 (±4) *	2.5 (±3) *	-3.4 (±3) *	-4.8 (±9) *	-2.7 (±5) *
MCP-5	-5.6 (±7) *	-5.1 (±12)	3.4 (±5) *	-3.1 (±10)	-2.3 (±11) *	-4.1 (±11)
PIP-5	1.4 (±12)	-0.5 (±4)	-4.4 (±5) *	-4.5 (±6) *	-3.2 (±6) *	-3.5 (±8)
DIP-5	5.1 (±14) *	-8.2 (±9) *	-1.9 (±8)	-2.2 (±7) *	-4.2 (±7) *	-4.0 (±15)

Table 6.2: Differences between A- and P-RoMs.

	Flexion (Pmax-Amax)	Extension (Amin-Pmin)	Radial (Pmax-Amax)	Ulnar (Amin-Pmin)	CW (Pmax-Amax)	CCW (Amin-Pmin)
CMC-1	4.2 (±9) *	1.4 (±4)	3.3 (±8)	-0.7 (±9)	-0.2 (±7)	0.9 (±9)
MP-1	18.7 (±13) *	17.9 (±16) *	1.4 (±8)	-1.3 (±4)	-0.1 (±11)	4.4 (±11)
IP-1	13.6 (±18) *	8.9 (±9) *	1.3 (±5)	1.8 (±4)	-1.0 (±8)	1.9 (±8)
CMC-2	2.0 (±3) *	1.8 (±7)	3.6 (±4) *	-0.5 (±5)	3.5 (±5) *	3.6 (±6) *
MCP-2	11.5 (±21) *	23.7 (±12) *	6.0 (±4) *	3.3 (±8)	3.1 (±9)	-1.1 (±5)
PIP-2	11.5 (±7) *	8.1 (±10) *	2.4 (±3)	3.0 (±2) *	1.7 (±5)	6.9 (±6) *
DIP-2	9.9 (±8) *	24.2 (±10) *	2.6 (±3) *	3.2 (±6) *	5.4 (±8) *	4.8 (±4) *
CMC-3	/	/	/	/	/	/
MCP-3	5.4 (±23) *	21.7 (±9) *	7.0 (±5) *	10.0 (±9) *	7.1 (±11) *	4.8 (±6) *
PIP-3	11.8 (±10) *	7.4 (±7) *	4.6 (±8) *	4.0 (±5) *	9.7 (±7) *	10.0 (±8) *
DIP-3	3.0 (±15) *	17.2 (±14) *	4.1 (±6) *	2.7 (±4) *	7.3 (±7) *	5.1 (±11) *
CMC-4	0.4 (±3)	5.7 (±4) *	-0.9 (±2)	3.2 (±3) *	7.6 (±8) *	4.1 (±6) *
MCP-4	12.2 (±20) *	22.0 (±10) *	11.2 (±8) *	10.9 (±7) *	7.8 (±8) *	10.9 (±11) *
PIP-4	9.0 (±11) *	5.2 (±6) *	5.1 (±8) *	3.6 (±5) *	11.3 (±7) *	10.6 (±10) *
DIP-4	8.0 (±15) *	15.7 (±9) *	2.9 (±4) *	1.0 (±3)	8.1 (±11) *	2.5 (±5) *
CMC-5	1.5 (±5)	6.1 (±3) *	-0.0 (±2)	5.5 (±6) *	6.8 (±8) *	1.5 (±6)
MCP-5	15.3 (±23) *	20.5 (±16) *	3.4 (±4) *	4.8 (±6) *	2.2 (±10) *	10.2 (±10) *
PIP-5	9.9 (±10) *	3.6 (±4) *	3.7 (±5) *	2.4 (±4) *	8.4 (±7) *	4.7 (±9) *
DIP-5	13.1 (±15) *	18.7 (±11) *	1.8 (±8)	0.7 (±8)	7.2 (±10) *	-0.7 (±13)

ently, we included all possible rotation angles during the functional activities. Although the duration of these hyper-rotations might be short, they are still part of the action and are the key movement of the functional task.

The definitions of the A-RoM and P-RoM have little dispute as all studies defined them with the maximum and the minimum angles of the collected data. In contrast,

Table 6.3: Differences between F- and P-RoMs.

	Flexion (Pmax-Fmax)	**Extension** (Fmin-Pmin)	**Radial** (Pmax-Fmax)	**Ulnar** (Fmin-Pmin)	**CW** (Pmax-Fmax)	**CCW** (Fmin-Pmin)
CMC-1	-0.6 (±9)	4.4 (±6) *	0.7 (±7)	-4.8 (±9) *	1.8 (±9)	-2.2 (±10)
MP-1	24.6 (±16) *	12.1 (±14) *	-5.5 (±6) *	-0.3 (±6)	1.4 (±11)	-5.3 (±12)
IP-1	21.5 (±22) *	-0.6 (±7)	2.2 (±4) *	-2.1 (±5) *	2.9 (±7)	-6.0 (±9) *
CMC-2	0.6 (±4)	0.2 (±7)	2.0 (±3) *	1.0 (±4)	5.3 (±6) *	-2.0 (±7)
MCP-2	16.7 (±21) *	19.2 (±19) *	6.8 (±6) *	-3.3 (±6) *	5.0 (±9) *	-1.7 (±9)
PIP-2	16.1 (±9) *	6.7 (±8) *	-1.0 (±4)	-2.3 (±5) *	-4.6 (±7) *	0.6 (±6)
DIP-2	21.5 (±13) *	3.9 (±8)	-0.5 (±4)	-1.7 (±5)	1.1 (±7)	-5.1 (±11) *
CMC-3	/	/	/	/	/	/
MCP-3	10.8 (±21) *	15.9 (±21) *	7.6 (±6) *	-0.9 (±11)	4.9 (±10) *	0.3 (±6)
PIP-3	14.8 (±11) *	9.0 (±9) *	-1.4 (±9)	-1.3 (±4)	0.7 (±10)	3.7 (±10)
DIP-3	15.4 (±17) *	4.9 (±7) *	1.6 (±7)	-0.6 (±5)	-2.5 (±5) *	1.7 (±7)
CMC-4	-0.9 (±3)	4.3 (±5) *	0.2 (±3)	1.6 (±2) *	5.5 (±10) *	2.6 (±7)
MCP-4	12.9 (±19) *	11.8 (±15) *	9.7 (±8) *	4.3 (±8) *	5.7 (±7) *	9.1 (±8) *
PIP-4	8.5 (±10) *	8.1 (±6) *	0.7 (±8)	-4.8 (±9) *	7.9 (±6) *	6.6 (±10) *
DIP-4	17.8 (±14) *	7.4 (±11) *	0.4 (±6)	-2.7 (±5) *	0.2 (±11)	-0.5 (±5)
CMC-5	-3.0 (±3) *	1.6 (±5)	2.4 (±4) *	2.1 (±4) *	2.0 (±11)	-1.1 (±7)
MCP-5	9.7 (±21) *	15.3 (±10) *	6.8 (±6) *	1.7 (±8)	-0.1 (±7)	6.2 (±8) *
PIP-5	11.3 (±11) *	3.1 (±5) *	-0.7 (±6)	-2.1 (±7)	5.2 (±7) *	1.2 (±11)
DIP-5	18.2 (±10) *	10.5 (±12) *	-0.1 (±5)	-1.5 (±8)	3.0 (±9)	-4.8 (±11)

6

the definition for the F-RoM has two major approaches: (1) take the extreme range of the collected data, (2) use percentiles of the measurement, usually 90% of the extreme range. In this study, we adopted the first approach; we defined all three RoMs with the maximal and minimal rotation angles we collected. Using this method requires high-quality data because any outliers in the measurement could influence the range. Contrarily, defining RoMs with percentiles of the measurement is more robust; but this can exclude extreme information. For instance, during the performance of a functional task, the duration of the extreme posture with large rotation angles is short, then this only accounts for a small percentage of the full movement (e.g., less than 10%), and this large rotation angle is excluded. Hence, we included the extreme rotation angles and considered the full motion ranges when measuring the F-RoM, as these extreme rotations also reflect part of the functional activities.

Besides, the measuring approaches also introduced measurement differences among the studies. This study applied an optical tracking system to collect continuous data of joint rotation angles and adopted LCS in the calculation. The advantage of our system was that the rotations of all finger joints can be measured simultaneously, and all joints were considered as three degrees of freedom joints. In comparison, studies using (electro-) goniometers or flex sensors assume the joint as a one-degree-of-freedom joint, which is in contrast to the anatomy. The measured active RoM of our study was consistent with another study that also calculated the rotation angles of finger joints along three axes using captured LCS [147]. We both found that self-rotation coupled with flx-ext and rad-uln deviation. The detected self-rotation and rad-uln deviation indicated that certain torque was applied on the joints during movements. This finding agreed with the conclusion of an in-vivo study that under-

lines the importance of self-rotation when considering the joint rotations of fingers [172]. With the accessibility to advanced devices and techniques, we encourage considering the joints as three degrees of freedom in the measurement and analysis.

Moreover, the selection of the functional activities may also influence the results. In selecting the functional activities, we intended to include both prehensile and non-prehensile activities instead of focusing on the prehensile movement only. The reason was that the prehensile actions are mainly accomplished with finger flexion, then the extension will be excluded. The selected 12 activities in the present study tried to cover more scenarios for the activities of daily living. The moments with hyper-rotation occurred mainly during fine manipulation or power grasp when the force was crucial for controlling the object with fingers or stabilizing the object within the hand. For example, key pinch for opening the door or press for pushing objects. The reaction force during the interaction between the fingers and the object may increase the rotation ranges.

The two main limitations of this study were the sample size and the intervention of a nature movement. Although the number of included participants is adequate for matched-pair comparisons, increasing the sample size may enable detailed statistical analysis related to gender, handiness, and hand size [167]. The applied optical tracking system was a marker-based system. Marker loosening was observed when participants with small hands performed some functional activities and those frames were excluded. To avoid such issues and record more natural movements in the future, a marker-less tracking system can be an option [173]. Nonetheless, these systems currently are less robust than marker-based systems and they require a larger database for training and ensuring tracking accuracy [151].

In summary, this study suggested that A-RoM had a large overlap but was unable to cover the range for some functional activities. Thus, the study on both F-RoM and P-RoM are as important as the one on A-RoM for a comprehensive understanding of the kinematics of hand joints. The knowledge of all three types of RoMs can support clinical diagnosis and treatment. Also, it can contribute to the optimization and evaluation of hand-related designs, e.g. implant designs for fingers or hand splints.

6

7

GENERAL DISCUSSION

This chapter addresses the research questions, summarizes the findings from both the skeleton system and the skin system studies, and discusses their implications in three contexts: medical, engineering, and design. The fundamental research findings are shown to support the development and validation of implant replacement designs.
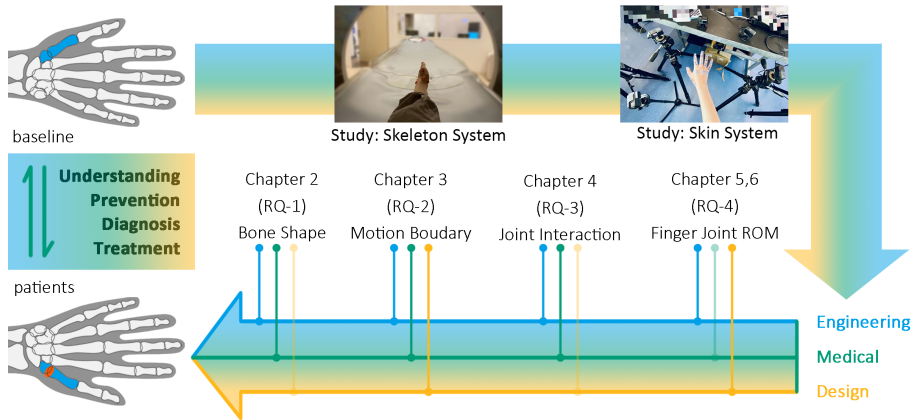
Figure 7.1: The Framing of this dissertation.

7.1. RECAP OF THE STUDY GOAL

The initial of this dissertation was to look for an optimization solution for treating the CMC-1 joint OA, possibly with patient-specific solutions. Yet, in the exploration phases, a knowledge gap to support the design solutions was noticed. The function of implant replacements is to replace degenerated bone tissues with artificial components, and the goal of this treatment is to restore the mobility and functionality of the joint, as well as to relieve the pain. However, the natural (healthy and non-degenerated) state of the CMC-1 joint is unclear. Therefore, this dissertation was adjusted to the main research question **"What is the natural state of asymptomatic CMC-1?"**. The outcomes of this dissertation are based on the healthy population, which serves as a baseline by combining medical understanding and engineering analysis to support and guided the implant replacement design solutions. Research, as this dissertation tackled fundamental questions, is beneficial to understand the pathology (etiology) of the CMC-1 OA, which can ultimately find its application in **prediction, prevention, diagnostic, and treatment** (see Fig. 7.1).

7.2. CONCLUSIONS TO THE RESEARCH QUESTIONS

This dissertation tried to answer the main RQ "What is the natural state of asymptomatic CMC-1?" with the framing as shown in Fig. 7.1. Four detailed research questions were elaborated based on an in-vivo study (the skeleton system, or the internal system) and an optical study (the skin system, or the external system). A relatively large 4D CT dataset for the circumduction of healthy CMC-1 joints was collected for investigating the internal system (the skeleton level), and an optical tracking system was developed to support the external system (the skin level)

RQ1: What's the shape variance among asymptomatic CMC-1?

Chapter 2 utilizes paired data to address RQ1 with two key findings through an assessment of the geometric shape variations of the trapezium (TPM) and 1st metacarpal bone (MC1) of the asymptomatic population. (1) The findings indicate that bones on the dominant side are consistently slightly larger than those on the non-dominant side. (2) This chapter establishes connections between regions of the bone exhibiting significant shape variance and the attachment sites of ligaments and tendons.

RQ2, RQ3: What's the contact pattern between the two bones during the movement? What's the movement boundaries of the asymptomatic CMC-1?

Chapter 3 investigated the contact pattern between the TPM and the MC1 during the maximum reachable circumduction, addressing RQ2. Chapter 4 focused on exploring the trace of the boundary motion and delved into the detailed changes in arthrokinematics variables throughout the circumduction movement, addressing RQ3. There are three key take outs in these two chapters. (1) The recurrence frequency for females was higher than that for males when assuming a 1.5 mm joint space, which is correlated to the higher prevalence of CMC-1 OA among females. (2) The contract ratio for females was generally larger than that for males across most frames, while the contact area during full circumduction was similar. (3) The mean boundary motion trace of MC1 regarding TPM formed a skewed hyperbolic shape, with the waist of the shape located on the MC1 side. This indicates that the rotation center of the CMC-1 is located outside the TPM.

RQ4: What's the range of motion for finger joints in different scenarios?

Chapter 5 developed the optical tracking system that was applied in the study based on the skin system. Chapter 6 compared the range of motion (ROM) for all finger joints during a series of hand activities for RQ4. Three types of motion ranges were measured: active ROM, functional ROM, and passive ROM. (1) The findings underlined that the functional ROM can exceed the active ROM in some tasks, especially during fine and power manipulation. (2) Understanding the passive ROM is also essential for the optimization and validation of joint-related designs.

7.3. Reflection and Insights

The primary objective of CMC-1 joint is to enable joint mobility and functionality. The mechanical understanding of the joint includes bone morphology (Chapter 2), joint movement (range of motion) (Chapter 3,4,5,6), and the loading scenarios (see Fig. 7.2). This dissertation tackled the first two elements. The baseline understanding of the joint behavior, the average and the variance, is essential to guide the development of an implant replacement. For the CMC-1 joint, the movement and the force of the joint is currently especially important, followed by the research on the morphology, as the articulate surfaces are reshaped during the surgery.
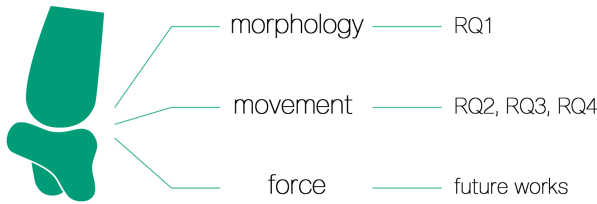
Figure 7.2: The key topics in Biomechanics related to the reflection.

7.3.1. DEMANDS OF BASELINE KNOWLEDGE IN THE MEDICAL CONTEXT

UNDERSTANDING THE WHOLE POPULATION MORE THAN SEX-LINKED DIFFERENCES
This dissertation primarily investigated the average and the variations of the bone morphology and motion patterns. Additionally, Chapter 2-4 also compare the average results of the two sexes, because the consensus that the prevalence of CMC-1 OA for females is significantly higher than that for males [16, 18, 17, 14]. Along with several studies [56, 89, 57], Chapter 2, has concluded that the shape similarity between females and males, excluding the bone size: males have larger bones than females. Findings in the motion loci (Chapter 4) and contact patterns (Chapter 3) also indicated sex-lined similarity; however, the contact ratio in most frames where higher for females than males. This posed the possibility that the higher contact ratio in movement may contribute to osteoarthritis. Several factors may contribute to osteoarthritis [12, 73], and the sex-linked difference is highly related to genetic factors. From the mechanical point of view, understanding the fundamental causes of the degeneration process may offer deeper insights into the etiology of joint osteoarthritis. The findings in this dissertation extend to the reflection that if bone size (Chapter 2), bone shape [43], or the motion pattern (Chapter 3, Chapter 4) is the contributor to the vulnerability of CMC-1 OA. The contribution of these factors remains to be studied. Investigation of the average and the variations among the population may provide a better indicator of the etiology, prevention, and diagnosis.

ADOPTING SYMMETRIC ASSUMPTION AS REFERENCE
The human torso is generally regarded as a symmetrical entity [47, 48, 46], and bilateral information plays a crucial role in diagnosis and treatment. Especially, when it comes to the upper limbs, such as the hands, the two hands are classified as dominant and non-dominant hands because of the distinction use of them [67, 49, 68]. This classification is adopted in this dissertation instead of left and right hands. The relatively higher variation around the attachment sites on the bones for both within-subject and between-subject analysis indicated the potential association between joint movement/loading and bone morphology. In clinical practices, hand surgeons now tend to adopt treatment plans based on the healthy contralateral condition for patient-specific surgical guidance and implants [44, 49, 174]. It is essential to validate the symmetry assumption. Chapter 2 addressed the investigation of the bilateral bone models. The bones on the dominant sides were found to be slightly but con-

sistently larger than those on the non-dominant sides, although the within-subject shape variances were not statistically significant compared to the between-subject shape variances. The sizing influence is suggested to be considered when adopting the bilateral information.

7.3.2. CHALLENGES FOR RESEARCH IN THE ENGINEERING CONTEXT

CONDUCTING IN-VIVO STUDIES TO SUPPORT/OPTIMIZE BALL-SOCKET MECHANISM

Based on the in-vivo study, Chapter 4 showed that the average motion trace of thumb maximum circumduction formed an approximate skewed one-sheet hyperbolic surface in the space, and the waist of this shape was located on the metacarpal side instead of the TPM side. This anatomical joint mechanism differs from the ball-socket mechanism of the CMC-1 implant replacement [104, 31]. The ball-socket mechanism for the CMC-1 joint can be referred to as the one for hip implants. The debate that if the ball-socket can represent and fulfill the necessary motion range remain a topic of discussion when concerns the unsatisfied durability and success rate for the CMC-1 implant replacements. Some studies suggested that the ball-socket design fails to replicate the natural motion mechanism of a healthy CMC-1 joint [104]; while some researchers argued that the ligament scission during the arthroplasty surgery can alter the movement mechanism of the joint, thus the saddle joint system can be challenging for patients to control the thumb. However, answering this question requires further studies (e.g., Chapter 7.6.2). As the articulate morphology, ligament status, and contact biomechanics has deviated since the joint degeneration, the understanding of the symptomatic state is also essential for answering this topic. Therefore, in addition to challenging the ball-socket design with a surface-replacement design, an alternative direction for optimizing the future design in the new design iterations can consider the optimal rotation centers [114] based on the findings and open for an innovative movement mechanism.

SIMPLIFYING THE STUDY TO INCREASE THE RESEARCH ACCESSIBILITY

Utilizing the 4D CT scanning techniques, the in-vivo study successfully collected the bone positions for a 12-second circumduction movement into around 40-50 frames. The results of this study fill the knowledge gap of the 3D form of an active motion boundary (Chapter 4) and the contact change throughout the movement circle (Chapter 3). The findings in this dissertation are valuable to extend current knowledge focusing on selected static extreme positions. The 3D form based on continuous form indicated clear potential guidance to simplify the targe movement along two principal directions which can still represent the full motion boundary. The end of the motion boundary presents a quasi-elliptical locus (see Fig. 3.7, Fig. 3.4), which shows that the relative positions of the MC1 to the TPM in the flexion and the abduction are along the major principal axes of the elliptic and the abduction and extension are close to the abduction; yet the representative positions to the minor principal axis of the elliptic is undetermined. A mathematical envelope may be needed to further identify the key corresponding frames, thus simulating the full circle of motion range with these key frames. The advantages of reducing the study frames into static scan-

ning include the increase of scanning resolution and the reduction of the radiation dose to patients, which can greatly improve the accessibility to researchers in all related fields. Moreover, focusing on the key positions can benefit the research on the force and the contact pattern, and thus bridge the understanding without loading (the active boundary) and with loading (the passive boundary).

7.3.3. OPPORTUNITIES OF OPTIMIZATION IN THE DESIGN CONTEXT

SCALE MATTERS THE CHALLENGES FOR RESEARCH AND DESIGN

The focus joint in this dissertation is the CMC-1, which is a delicate joint in a complex system enabling a wide range of motion. This complex system and the small bone size have considerable influence on the research on this joint and the development of the implants for this joint. The average bone size of TPM were 19.7 mm x 15.0 mm 12.9 mm (Chapter 2). There are limited commercial options, mainly the ball-socket with a straight neck and the 15-degree neck with several different sizes. In contrast, extensive studies on bone morphology, the joint range of motion, joint loading biomechanics, gait analysis, etc. on the hip and knee have greatly benefited and supported the development of implant replacements for the hip and knee. In comparison, The small bone size challenges the cup fixation, issues of the bone compositions, the operation space, the accuracy of the cut, etc. The small size of the thumb-base joint has less tolerance for mispositioning than the one for big joints. Currently, the operation outcomes are highly dependent on the experience of the surgeon, encompassing factors such as implantation angles, depth, and appropriate sizing. Despite having an anatomically perfect implant, incorrect or sub-optimal placement can occur during several stages of the procedure. In this regard, filling the knowledge gap as contributed in this dissertation is also crucial to support the optimization of the motion mechanism [114], the fixation mechanism [175], and the operation tools.

DESIGNERS CONNECTS ALL STOCKHOLDERS

Chapter 5 and Chapter 6 tackled the discussion on the user requirements in daily activities and the extremities of the joint. The three ranges of motion: the active range of motion, the functional range of motion, and the passive range of motion are related to the stakeholder map in the design phase (see Fig 7.3). "Design" is a coordination phase, which collected the needs of users (surgeons and patients), addresses them to the research communities, and also optimizes product design with reliable production technologies. "Research" supports the design for users and the manufacturing limits; additionally, "Research" influences the medical device standards in the industry. "Manufacturing" is the media that realize concepts into products for users following production standards. In the case of CMC-1 implant design, surgeons and patients are considered as the end user. They tend to prioritize active mobility and functional mobility respectively in evaluating the outcome of surgeries; from the engineering (manufacturing) point of view, passive movement, which challenges the limits of the implants, is the focus in developing and bringing the implant replacements to the market. In summary, the optimization of the implant designs requires
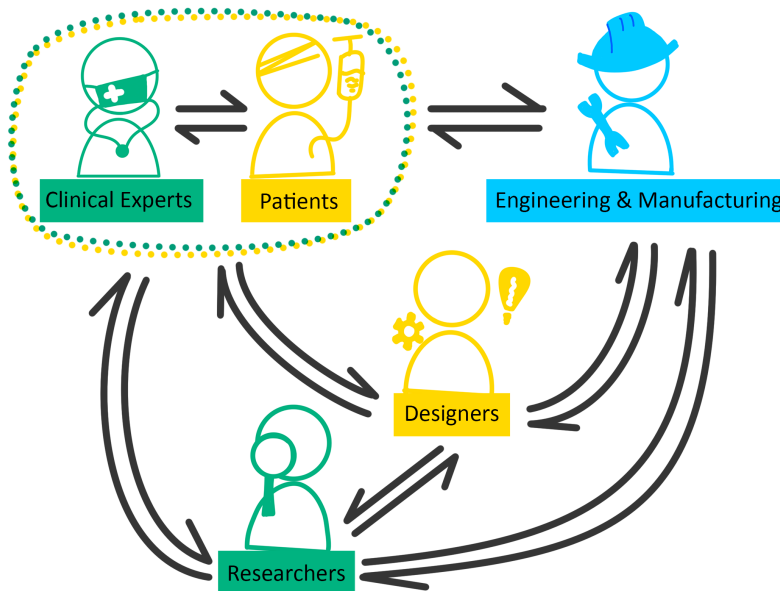
Figure 7.3: (Partial of) the stakeholder map for implant design.

an effective transformation of the research findings to applications, with well coordination across different aspects from all stakeholders. In this dissertation, after realizing the knowledge gap, the findings in the in-vivo study can better support the design; and the optical study leads to the reflection on the validation protocols in evaluating an implant and observing the needs of end users.

7.4. Limitation

Loading scenarios
The joint performance during loading tasks is excluded in this dissertation. This study focuses on the kinematics of the joint. However, to further understand the mechanical properties of the CMC-1 OA, knowledge from multiple aspects is needed (but not limited) (see Fig. 7.3). Since CMC-1 OA also bears a considerable load on the joint, the stress distribution of the joint contact during force-related tasks (e.g., [82, 84]) requires further study.

Activities of daily living
In addition to the loading scenarios, the required motion ranges during activities of daily living for the CMC-1 joint are unclear. In this dissertation, the circumduction was evenly interpolated, while the movement frequency can be various, e.g., the load for the flexion and the adduction can be higher than the extension and the abduction. Also, the evaluation of the treatment outcome for patients varies among the population due to different requirements on the activities in daily living. Future studies may

combine the measurements from the skin system with the in-vivo system, thus to better define the required motion range for the thumb and the CMC-1 joint.

AGE-RELATED ANALYSIS AND THE INVOLVEMENT OF PATIENTS

The missing age-related analysis and the long-term follow-up of the dataset, as well as the comparison between patients and healthy participants, are other limitations of this dissertation. CMC-1 OA is an age-related and sex-lined disease, however, the distribution of the age of included participants was mainly between 20 to 35 years old. Analysis and the conclusion with age factor can hardly be concluded with the statistical requirement. Longitudinal studies and/or datasets including patient data may suggest a highly related understanding of the pathology of joint degeneration.

7.5. FUTURE PROJECTS

1) AN AUTHENTIC PHANTOM

As mentioned in the Section (engineering context), access to the anatomical joint model can invoke the involvement of engineers and bring diverse solutions in understanding the complex system at hand and solving the issues. A recent study also pointed out that the current skeleton model for estimating thumb movement is less accurate than expected (TUD master project1). A concert consensus can be beneficial to further studies on the CMC-1. This will require a systematic knowledge of the attached ligament and tendons.

2) THE RELATIONSHIP BETWEEN THE SKELETON (INTERNAL) SYSTEM AND SKIN (EXTERNAL) SYSTEM.

As introduced in Chapter 1, the CMC-1 is a small joint in a deep position, which challenges precise measurement of it. For the long fingers, and the most joints that connect the two long bones, the joint rotation can be estimated with an optical system; and this increases the accessibility to engineering research. Similarly, if the movement of the CMC-1 can be estimated through skin markers (optical markers or sensors), this can enable the measurement of the required mobility during functional activities and passive movement. A preliminary result is enclosed in Appendix (Chapter Appendix 1). Further improvement in this topic will be helpful for future measurement and understanding of the movement of this unique joint.

3) IN-DEPTH ANALYSIS OF THE KEY ELEMENTS

The three elements to understand the CMC-1 behaviors (as summarized in Fig. 7.2) are discussed relatively individually in this dissertation. However, the connections between these elements are worth a future analysis in depth. For instance, the relationship between the curvature of the articulate surface of the two bones and the range of motion; the alignment of the coordinate systems during the movement may reflect the mobility and the flexibility of the movement. Although the significance of the relationship among these elements is unknown, the investigation has the potential to guide researchers and clinicians in better understanding this unique and essential joint.

8

APPENDIX I: POTENTIAL SYSTEMS CONNECTION

8.1. Introduction

The thumb-base joint is essential for daily thumb functional activities. Non-invasive studying approaches, e.g., skin markers, can hardly reach this small and deep joint [113, 176]; yet clinical research on it is necessary. Some studies have evaluated the skin effect on long fingers during flexion [177, 178]; however, the soft-tissue influence on the thumb remains unknown. This pilot study aims to explore and compare the measurement of the thumb using internal (bones) and external (skin markers) systems.

8.2. Method

The data of three healthy volunteers with consent were employed. Volunteers performed thumb circumduction with five T-markers on the skin [113] (Fig. 8.1) during 4D CT scanning. All T-markers, trapezium (TPM), and the first metacarpal (MC1) in all frames were segmented, meshed, and registered. The local coordinate systems (LCS) of each bone/marker were localized, and the relative (Euler) rotations and translations were extracted for analysis. Here, ZYX sequences were used for flexion-extension, adduction-abduction, and self-rotation.
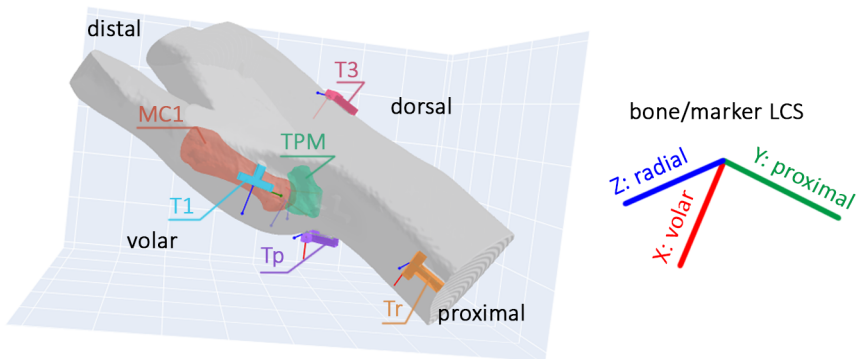
Figure 8.1: T-Marker placement and local coordinate systems (LCS).

8.3. Result and discussion

The rotations and translation of markers (Tp, Tr, T3 / T1) in relative to bones (TPM / MC1) were calculated. T3 was more representative of TPM as suggested by relatively small variation ranges among three possible combinations (Table 1); yet, their relative movement during large wrist motion was unclear. The translation between T1 and MC1 was comparable with the skin effect in long fingers [177, 178], but the rotation differences were larger than the results in a cadaver study [179], especially when the markers were close to the tendons during abduction and extension. Possibly, relocating T1 at the radial side of MC1 or different markers and placement strategies

[176] may reduce such influence.

The rotations and translations measured with external systems (T1 in relative to Tp, Tr, T3) and internal systems (bone MC1 in relative to bone TPM) generally showed a similar trend with motion (Figure 2), regardless of amplified differences. Hand sizes and the distance of marker placement may explain translation differences. Besides, the flexion-extension differences between the internal and external systems increase when the internal rotation decrease; the adduction-abduction curves of external systems were most close to the curves of internal systems at flexion gesture (approx.: frame 30).

Marker VS Bone	Flexion-Extension (degree)	Adduction-Abduction (degree)	Self- rotation (degree)	Translation (mm)
Tp-TPM	27, 14, 31	24, 29, 18	19, 23, 35	6.7, 5.4, 8.0
Tr-TPM	0- , 19, 28	0- , 13, 13	0- , 22, 18	0- , 4.8, 3.6
T3-TPM	08, 05, 17	07, 05, 13	13, 10, 22	3.8, 2.3, 2.0
T1-MC1	20, 30, 18	25, 17, 26	31, 49, 27	6.3, 3.2, 3.8
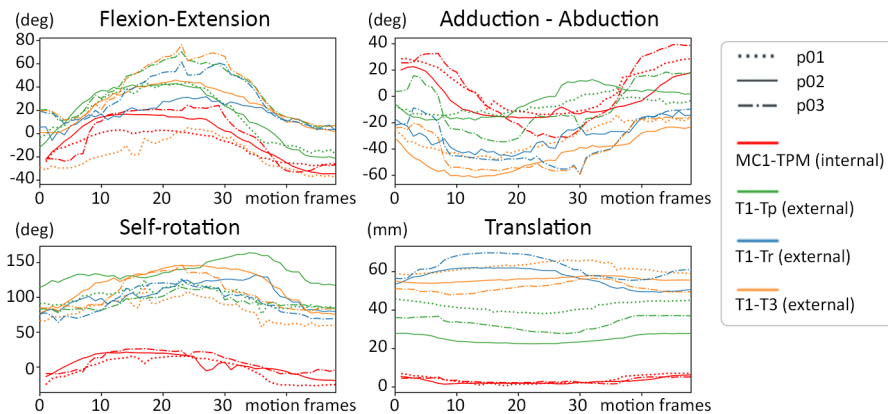
Figure 8.2: The relative rotations and translations of three volunteers.

8.4. CONCLUSION

The relative rotations and translations measured with external systems generally presented a similar trend as the measurement with internal systems, especially using T1 and T3 markers. Still, further research is necessary to assess the detailed relationships between the internal and external systems, thus can contribute to clinical diagnosis and future thumb biomechanical studies.

ACKNOWLEDGEMENTS

As I approach the end of this long and challenging PhD journey, I am filled with gratitude for the many people who have made this significant achievement possible.

I would like to start by expressing my deepest gratitude to Prof. dr. ir. Richard Goossens, Dr. Song Yu, and Dr. Gerald Kraan. Thank you for all the discussions throughout this journey. I could not have undertaken this without your supervision. I wish to express my special thanks to Prof. Richard Goossens for providing encouragement and opportunities, especially during the difficult and uncertain time To Dr. Gerald Kraan, my sincere thanks for providing invaluable collaboration opportunities and deepening my understanding of this project. I am also grateful to all the committee members for your time and efforts on my dissertation and defense.

I am grateful for the collaboration with Ian Blom and Dr. Nina Mathijssen. I cannot make progress on this PhD project without your assistance. Ian, your quick reply and instant support were exceptionally encouraging and deeply appreciated. Essentially, I would like to thanks all my participants. Although I cannot list your name here, your contribution is invaluable to my research and sincerely appreciated. I would also like to acknowledge the scholarship support from my country.

I would also thanks to Prof. dr. ir. Jo M.P. Geraedts and Dr. Yu Song for inspiring and setting me on my journey at TU Delft. My appreciation also extends to Prof. dr. ir. Peter Vink for your insightful lectures and the enjoyable moments we shared at the IDE band. I am thankful for the greetings and the conversations with Mr. Bertus early in the morning and your help on my hobby projects. I appreciate the talk with Dr. Johan Molembroek for extending my knowledge on anthropometry studies. My appreciation also extends to Dr. Ir. Marijke Melles, Dr. Ir. Sonja Paus-Buzink, and the AED section for the warm and inviting atmosphere. Additionally, I value the insightful collaboration with Dr. Ir. Gerwin Smit on the graduation project; the invited meetings and discussions were both enjoyable and beneficial to my work.

Furthermore, I would like to extend my appreciation to my lab mates, office mates, and friends. Jun Xu, Tao Hou, Hongpeng Zhou, Argun, Tessa Essers, Elvis, Yuguang Zhao, Yunran Qiu, Illaria, Soyeon Kim, Cehao Yu, Xueliang Li, Tim, Di Meng, Gerbera, Maxim, Dolores, Sumalee, Lyè, Farzam, Jiwei Zhou, it was nice to work and share the joyful moments with you. Maxim, thanks for translating my summary into Dutch. Tingting Wang, Xueqing Miao, Qiang Liu, thanks for inviting me to the badminton hours. Important thanks are extended to Dr. Tess Dekker and Dr. Patrizia D'Olivo for guiding me through the METC protocol application process in the early stage of my PhD journey. Zishun Liu, Zhong Gao, Dr. WMR Rusli, Julie Mottet, thank you for sharing knowledge and experience with me. Additionally, Selina, Sara, Rafaela, and Jolanda, thanks for your invaluable assistance, warm care, and the sweets offer

throughout these years. All these bring many colorful memories to my journey in TU Delft.

8

BIBLIOGRAPHY

[1] Aaron M Dollar. Classifying human hand use and the activities of daily living. *The human hand as an inspiration for robot hand development*, pages 201–216, 2014.

[2] Alfred B Swanson. Evaluation of impairment of function in the hand. *Surgical Clinics of North America*, 44(4):925–940, 1964.

[3] Lynette A Jones and Susan J Lederman. *Human hand function*. Oxford university press, 2006.

[4] Amy L Ladd. The teleology of the thumb: on purpose and design. *The Journal of hand surgery*, 43(3):248–259, 2018.

[5] Bart Visser, Michiel P De Looze, Matthijs P De Graaff, and Jaap H Van Dieën. Effects of precision demands and mental pressure on muscle activation and hand forces in computer mouse tasks. *Ergonomics*, 47(2):202–217, 2004.

[6] Ewa Gustafsson, Peter W Johnson, and Mats Hagberg. Thumb postures and physical loads during mobile phone use–a comparison of young adults with and without musculoskeletal symptoms. *Journal of Electromyography and Kinesiology*, 20(1):127–135, 2010.

[7] Esra Erkol İNal, Kadir Demirci, Azİze ÇetİNtürk, Mehmet Akgönül, and Serpİl Savaş. Effects of smartphone overuse on hand function, pinch strength, and the median nerve. *Muscle & nerve*, 52(2):183–188, 2015.

[8] Jinghong Xiong and Satoshi Muraki. An ergonomics study of thumb movements on smartphone touch screen. *Ergonomics*, 57(6):943–955, 2014.

[9] Sterling Bunnell. Opposition of the thumb. *JBJS*, 20(2):269–284, 1938.

[10] WP Cooney 3rd and EY Chao. Biomechanical analysis of static forces in the thumb during hand function. *JBJS*, 59(1):27–36, 1977.

[11] L Athlani, M Bergere, D Motte, B Prandi, J-Y Beaulieu, and F Moissenet. Trapeziometacarpal joint loading during key pinch grip: A cadaver study. *Hand Surgery and Rehabilitation*, 41(2):204–209, 2022.

[12] David J Hunter, Lyn March, and Mabel Chew. Osteoarthritis in 2020 and beyond: a lancet commission. *The Lancet*, 396(10264):1711–1712, 2020.

[13] Saeede Dahaghin, Sita MA Bierma-Zeinstra, AZ Ginai, HAP Pols, JMW Hazes, and BW Koes. Prevalence and pattern of radiographic hand osteoarthritis and association with pain and disability (the rotterdam study). *Annals of the rheumatic diseases*, 64(5):682–687, 2005.

[14] Yuqing Zhang, Jingbo Niu, Margaret Kelly-Hayes, Christine E Chaisson, Piran Aliabadi, and David T Felson. Prevalence of symptomatic hand osteoarthritis and its impact on functional status among the elderly: The framingham study. *American journal of epidemiology*, 156(11):1021–1027, 2002.

[15] Robbert M Wouters, Ana-Maria Vranceanu, Harm P Slijper, Guus M Vermeulen, Mark JW van Der Oest, Ruud W Selles, Jarry T Porsius, Hand-Wrist Study Group, et al. Patients with thumb-base osteoarthritis scheduled for surgery have more symptoms, worse psychological profile, and higher expectations than nonsurgical counterparts: a large cohort analysis. *Clinical Orthopaedics and Related Research*, 477(12):2735, 2019.

[16] MJW Van der Oest, LS Duraku, ER Andrinopoulou, RM Wouters, SMA Bierma-Zeinstra, RW Selles, and JM Zuidam. The prevalence of radiographic thumb base osteoarthritis: a meta-analysis. *Osteoarthritis and Cartilage*, 29(6):785–792, 2021.

[17] Jessica Bijsterbosch, Willemien Visser, Herman M Kroon, Tanja Stamm, Ingrid Meulenbelt, Tom WJ Huizinga, and Margreet Kloppenburg. Thumb base involvement in symptomatic hand osteoarthritis is associated with more pain and functional disability. *Annals of the rheumatic diseases*, 69(3):585–587, 2010.

[18] JL Van Saase, LK Van Romunde, ARNOLD Cats, JP Vandenbroucke, and HA Valkenburg. Epidemiology of osteoarthritis: Zoetermeer survey. comparison of radiological osteoarthritis in a dutch population with that in 10 other populations. *Annals of the rheumatic diseases*, 48(4):271–280, 1989.

[19] A-M Gay, A Cerlier, A Iniesta, and R Legré. Surgery for trapeziometacarpal osteoarthritis. *Hand Surgery and Rehabilitation*, 35(4):238–249, 2016.

[20] Anne J Spaans, L Paul Van Minnen, Moshe Kon, Arnold H Schuurman, AR Ton Schreuders, and Guus M Vermeulen. Conservative treatment of thumb base osteoarthritis: a systematic review. *The Journal of hand surgery*, 40(1):16–21, 2015.

[21] Margreet Kloppenburg, Sjoerd van Beest, and Féline PB Kroon. Thumb base osteoarthritis: a hand osteoarthritis subset requiring a distinct approach. *Best Practice & Research Clinical Rheumatology*, 31(5):649–660, 2017.

[22] Glyka Martou, Karen Veltri, and Achilleas Thoma. Surgical treatment of osteoarthritis of the carpometacarpal joint of the thumb: a systematic review. *Plastic and reconstructive surgery*, 114(2):421–432, 2004.

8

[23] Vincent R Hentz. Surgical treatment of trapeziometacarpal joint arthritis: a historical perspective. *Clinical Orthopaedics and Related Research®*, 472:1184–1189, 2014.

[24] Augustin Lerebours, Frederic Marin, Salima Bouvier, Christophe Egles, Alain Rassineux, and Alain-Charles Masquelet. Trends in trapeziometacarpal implant design: a systematic survey based on patents and administrative databases. *The Journal of Hand Surgery*, 45(3):223–238, 2020.

[25] European board of hand surgery. *White book of hand surgery in europe*. Federation of European Societies for Surgery of the Hand (FESSH), 2020.

[26] Qi Yin, Merel J-L Berkhout, and Marco JPF Ritt. Current trends in operative treatment of carpometacarpal osteoarthritis: a survey of european hand surgeons. *European Journal of Plastic Surgery*, 42:365–368, 2019.

[27] Nederlandse Vereniging voor Plastische Chirurgie (NVPC). *Conservatieve en Chirurgische Behandeling van Primaire Artrose van de Duimbasis.* Nederlandse Vereniging voor Handchirurgie (NVVH), 2014.

[28] Philippe Bellemère and Bruno Lussiez. Thumb carpometacarpal implant arthroplasty. *Hand Clinics*, 38(2):217–230, 2022.

[29] Guus M Vermeulen, Harm Slijper, Reinier Feitz, Steven ER Hovius, Thybout M Moojen, and Ruud W Selles. Surgical management of primary thumb carpometacarpal osteoarthritis: a systematic review. *The Journal of hand surgery*, 36(1):157–169, 2011.

[30] Aparna D Ganhewa, Rui Wu, Michael P Chae, Vicky Tobin, George S Miller, Julian A Smith, Warren M Rozen, and David J Hunter-Smith. Failure rates of base of thumb arthritis surgery: a systematic review. *The Journal of hand surgery*, 44(9):728–741, 2019.

[31] Jason J Srnec, Eric R Wagner, and Marco Rizzo. Implant arthroplasty for proximal interphalangeal, metacarpophalangeal, and trapeziometacarpal joint degeneration. *The Journal of Hand Surgery*, 42(10):817–825, 2017.

[32] Priscilla D'Agostino, Benjamin Dourthe, Faes Kerkhof, Filip Stockmans, and Evie E Vereecke. In vivo kinematics of the thumb during flexion and adduction motion: evidence for a screw-home mechanism. *Journal of Orthopaedic Research*, 35(7):1556–1564, 2017.

[33] Eni Halilaj, Douglas C Moore, Tarpit K Patel, David H Laidlaw, Amy L Ladd, Arnold-Peter C Weiss, and Joseph J Crisco. Older asymptomatic women exhibit patterns of thumb carpometacarpal joint space narrowing that precede changes associated with early osteoarthritis. *Journal of biomechanics*, 48(13):3634–3640, 2015.

8

[34] Faes D Kerkhof, Evie E Vereecke, Olivier Vanovermeire, Jeroen Vanhaecke, Maarten Vanneste, and Filip Stockmans. Trapeziometacarpal stabilization through dorsoradial ligament reconstruction: An early post-surgery in vivo biomechanical analyses. *Journal of Orthopaedic Research®*, 36(11):2851–2864, 2018.

[35] Satoshi Shimawaki, Takuma Murai, Masataka Nakabayashi, and Hideharu Sugimoto. Measurement of flexion angle of the finger joint during cylinder gripping using a three-dimensional bone model built by x-ray computed tomography. *Applied bionics and biomechanics*, 2019, 2019.

[36] FD Kerkhof, Eddy Brugman, Priscilla D'Agostino, Benjamin Dourthe, GH van Lenthe, Filip Stockmans, Ilse Jonkers, and EE Vereecke. Quantifying thumb opposition kinematics using dynamic computed tomography. *Journal of biomechanics*, 49(9):1994–1999, 2016.

[37] Gerard A Ateshian, Jon W Ark, Melvin P Rosenwasser, Robert J Pawluk, Louis J Soslowsky, and Van C Mow. Contact areas in the thumb carpometacarpal joint. *Journal of orthopaedic research*, 13(3):450–458, 1995.

[38] Laurence Cheze, Raphaël Dumas, J-J Comtet, Claude Rumelhart, and Michel Fayet. Determination of the number of degrees of freedom of the trapeziometacarpal joint–an in vitro study. *IRBM*, 33(4):272–277, 2012.

[39] Michelle Marshall, Danielle van der Windt, Elaine Nicholls, Helen Myers, and Krysia Dziedzic. Radiographic thumb osteoarthritis: frequency, patterns and associations with pain and clinical assessment findings in a community-dwelling population. *Rheumatology*, 50(4):735–739, 2011.

[40] FV Wilder, JP Barrett, and EJ Farina. Joint-specific prevalence of osteoarthritis of the hand. *Osteoarthritis and cartilage*, 14(9):953–957, 2006.

[41] Jeonghwan Kim, Hyun Sik Gong, Jihyeung Kim, Min Bom Kim, Young Ho Lee, and Goo Hyun Baek. The relationship between the bony morphology of first metacarpal base and the stability of the thumb carpometacarpal joint in a normal female population: Level 1 evidence. *Journal of Hand Surgery*, 40(9):e29, 2015.

[42] MTY Schneider, Ju Zhang, CG Walker, JJ Crisco, A-PC Weiss, AL Ladd, PMF Nielsen, and Thor Besier. Early morphologic changes in trapeziometacarpal joint bones with osteoarthritis. *Osteoarthritis and cartilage*, 26(10):1338–1344, 2018.

[43] Christopher D Flanagan, Pierre Tamer, Daniel R Cooperman, Joseph J Crisco, Amy L Ladd, and Raymond W Liu. An anatomical evaluation of the trapezium and its relationship to basilar joint osteophytic change. *HAND*, 17(4):714–722, 2022.

8

[44] Philipp Honigmann, Ralf Schumacher, Romy Marek, Franz Büttner, Florian Thieringer, and Mathias Haefeli. A three-dimensional printed patient-specific scaphoid replacement: a cadaveric study. *Journal of Hand Surgery (European Volume)*, 43(4):407–412, 2018.

[45] Zhen-jiang Ma, Zi-fan Liu, Qing-song Shi, Tao Li, Zhi-yuan Liu, Ze-zheng Yang, Yi-hao Liu, Yuan-jin Xu, Kerong Dai, Chao Yu, et al. Varisized 3d-printed lunate for kienböck's disease in different stages: Preliminary results. *Orthopaedic surgery*, 12(3):792–801, 2020.

[46] Alexandra S Gabrielli, Tom Gale, MaCalus Hogan, and William Anderst. Bilateral symmetry, sex differences, and primary shape factors in ankle and hindfoot bone morphology. *Foot & Ankle Orthopaedics*, 5(1):2473011420908796, 2020.

[47] K Islam, A Dobbe, A Komeili, K Duke, M El-Rich, S Dhillon, S Adeeb, and NM Jomha. Symmetry analysis of talus bone: a geometric morphometric approach. *Bone & joint research*, 3(5):139–145, 2014.

[48] Nazlı Tümer, Vahid Arbabi, Willem Paul Gielis, Pim A de Jong, Harrie Weinans, Gabrielle JM Tuijthof, and Amir A Zadpoor. Three-dimensional analysis of shape variations and symmetry of the fibula, tibia, calcaneus and talus. *Journal of anatomy*, 234(1):132–144, 2019.

[49] Nazlı Tümer, Olivier Hiemstra, Yvonne Schreurs, Gerald A Kraan, Johan van der Stok, and Amir A Zadpoor. The three-dimensional shape symmetry of the lunate and its implications. *Journal of Hand Surgery (European Volume)*, 46(6):587–593, 2021.

[50] M Beck, M Kalhor, M Leunig, and R Ganz. Hip morphology influences the pattern of damage to the acetabular cartilage: femoroacetabular impingement as a cause of early osteoarthritis of the hip. *The Journal of bone and joint surgery. British volume*, 87(7):1012–1018, 2005.

[51] MMA Van Buuren, Nigel K Arden, SMA Bierma-Zeinstra, Wichor M Bramer, Nicola C Casartelli, DT Felson, Graeme Jones, Nancy E Lane, Claudia Lindner, Nicola A Maffiuletti, et al. Statistical shape modeling of the hip and the association with hip osteoarthritis: a systematic review. *Osteoarthritis and cartilage*, 29(5):607–618, 2021.

[52] Lowell M Smoger, Kevin B Shelburne, Adam J Cyr, Paul J Rullkoetter, and Peter J Laz. Statistical shape modeling predicts patellar bone geometry to enable stereo-radiographic kinematic tracking. *Journal of biomechanics*, 58:187–194, 2017.

[53] D Humes, H Jähnich, A Rehm, and JP Compson. The osteology of the trapezium. *The Journal of Hand Surgery: British & European Volume*, 29(1):42–45, 2004.

8

[54] Ryo Yoshida, Hugh O House, Rita M Patterson, Munir A Shah, and Steven F Viegas. Motion and morphology of the thumb metacarpophalangeal joint. *The Journal of hand surgery*, 28(5):753–757, 2003.

[55] Eni Halilaj, Douglas C Moore, David H Laidlaw, Christopher J Got, Arnold-Peter C Weiss, Amy L Ladd, and Joseph J Crisco. The morphology of the thumb carpometacarpal joint does not differ between men and women, but changes with aging and early osteoarthritis. *Journal of biomechanics*, 47(11):2709–2714, 2014.

[56] MTY Schneider, Ju Zhang, JJ Crisco, APC Weiss, AL Ladd, Poul Nielsen, and Thor Besier. Men and women have similarly shaped carpometacarpal joint bones. *Journal of biomechanics*, 48(12):3420–3426, 2015.

[57] Joseph J Crisco, James C Coburn, Douglas C Moore, and Mohammad A Upal. Carpal bone size and scaling in men versus in women. *The Journal of hand surgery*, 30(1):35–42, 2005.

[58] F Loisel, S Chapuy, P-B Rey, L Obert, B Parratte, L Tatu, and D Lepage. Dimensions of the trapezium bone: a cadaver and ct study. *Surgical and Radiologic Anatomy*, 37:787–792, 2015.

[59] Liangfeng Xu, Robert J Strauch, Gerard A Ateshian, Robert J Pawluk, Van C Mow, and Melvin P Rosenwasser. Topography of the osteoarthritic thumb carpometacarpal joint and its variations with regard to gender, age, site, and osteoarthritic stage. *The Journal of hand surgery*, 23(3):454–464, 1998.

[60] Wan MR Rusli and Angela E Kedgley. Statistical shape modelling of the first carpometacarpal joint reveals high variation in morphology. *Biomechanics and modeling in mechanobiology*, 19(4):1203–1210, 2020.

[61] Martijn van de Giessen, Mahyar Foumani, Geert J Streekstra, Simon D Strackee, Mario Maas, Lucas J van Vliet, Kees A Grimbergen, and Frans M Vos. Statistical descriptions of scaphoid and lunate bone shapes. *Journal of biomechanics*, 43(8):1463–1469, 2010.

[62] Paul C Bettinger, Ronald L Linscheid, Richard A Berger, William P Cooney III, and Kai-Nan An. An anatomic study of the stabilizing ligaments of the trapezium and trapeziometacarpal joint. *The Journal of hand surgery*, 24(4):786–798, 1999.

[63] Mitsuhiko Nanno, William L Buford Jr, Rita M Patterson, Clark R Andersen, and Steven F Viegas. Three-dimensional analysis of the ligamentous attachments of the first carpometacarpal joint. *The Journal of hand surgery*, 31(7):1160–1170, 2006.

[64] Matthew F Koff, Obinwanne F Ugwonali, Robert J Strauch, Melvin P Rosenwasser, Gerard A Ateshian, and Van C Mow. Sequential wear patterns of the

8

articular cartilage of the thumb carpometacarpal joint in osteoarthritis. *The Journal of hand surgery*, 28(4):597–604, 2003.

[65] Jack M Haglin, Adam EM Eltorai, Joseph A Gil, Stephen E Marcaccio, Juliana Botero-Hincapie, and Alan H Daniels. Patient-specific orthopaedic implants. *Orthopaedic surgery*, 8(4):417–424, 2016.

[66] Andrew Y Zhang, Sarah Van Nortwick, Elisabet Hagert, and Amy L Ladd. Thumb carpometacarpal ligaments inside and out: a comparative study of arthroscopic and gross anatomy from the robert a. chase hand and upper limb center at stanford university. *Journal of wrist surgery*, 2(01):055–062, 2013.

[67] Hwa S Jung and Hyung-Shik Jung. Hand dominance and hand use behaviour reported in a survey of 2437 koreans. *Ergonomics*, 52(11):1362–1371, 2009.

[68] Hiroshi Kousaka, Hiroshi Mizoguchi, Masahiro Yoshikawa, Hideyuki Tanaka, and Yoshio Matsumoto. Role analysis of dominant and non-dominant hand in daily life. In *2013 IEEE International Conference on Systems, Man, and Cybernetics*, pages 3972–3977. IEEE, 2013.

[69] Margarita Vergara, Joaquin L Sancho-Bru, Verónica Gracia-Ibáñez, and Antonio Pérez-González. An introductory study of common grasps used by adults during performance of activities of daily living. *Journal of Hand Therapy*, 27(3):225–234, 2014.

[70] Michael Benjamin and Dennis McGonagle. Entheses: tendon and ligament attachment sites. *Scandinavian journal of medicine & science in sports*, 19(4):520–527, 2009.

[71] Thomas P Andriacchi, Seungbum Koo, and Sean F Scanlan. Gait mechanics influence healthy cartilage morphology and osteoarthritis of the knee. *The Journal of Bone and Joint Surgery. American volume.*, 91(Suppl 1):95, 2009.

[72] Cara L Lewis, Natalie M Laudicina, Anne Khuu, and Kari L Loverro. The human pelvis: variation in structure and function during gait. *The Anatomical Record*, 300(4):633–642, 2017.

[73] Margreet Kloppenburg and Wing-Yee Kwok. Hand osteoarthritis—a heterogeneous disorder. *Nature Reviews Rheumatology*, 8(1):22–31, 2012.

[74] Jennifer Moriatis Wolf, Aleksandra Turkiewicz, Isam Atroshi, and Martin Englund. Occupational load as a risk factor for clinically relevant base of thumb osteoarthritis. *Occupational and environmental medicine*, 77(3):168–171, 2020.

[75] Luc Fontana, Stéphanie Neel, Jean-Marc Claise, Sylvie Ughetto, and Pierre Catilina. Osteoarthritis of the thumb carpometacarpal joint in women and occupational risk factors: a case-control study. *The Journal of hand surgery*, 32(4):459–465, 2007.

8

[76] Rie Kodama, Shigeyuki Muraki, Hiroyuki Oka, Toshiko Iidaka, Masatoshi Teraguchi, Ryohei Kagotani, Yoshiki Asai, Munehito Yoshida, Yutaka Morizaki, Sakae Tanaka, et al. Prevalence of hand osteoarthritis and its relationship to hand pain and grip strength in japan: the third survey of the road study. *Modern rheumatology*, 26(5):767–773, 2016.

[77] Jonathan T Evans, Jonathan P Evans, Robert W Walker, Ashley W Blom, Michael R Whitehouse, and Adrian Sayers. How long does a hip replacement last? a systematic review and meta-analysis of case series and national registry reports with more than 15 years of follow-up. *The Lancet*, 393(10172):647–654, 2019.

[78] John Slamin and Brian Parsley. Evolution of customization design for total knee arthroplasty. *Current reviews in musculoskeletal medicine*, 5:290–295, 2012.

[79] Ali Hosseini, Samuel K Van de Velde, Michal Kozanek, Thomas J Gill, Alan J Grodzinsky, Harry E Rubash, and Guoan Li. In-vivo time-dependent articular cartilage contact behavior of the tibiofemoral joint. *Osteoarthritis and cartilage*, 18(7):909–916, 2010.

[80] Blaž Mavčič, Aleš Iglič, Veronika Kralj-Iglič, Richard A Brand, and Rok Vengust. Cumulative hip contact stress predicts osteoarthritis in ddh. *Clinical orthopaedics and related research*, 466:884–891, 2008.

[81] Priscilla D'Agostino, Benjamin Dourthe, Faes Kerkhof, G Harry Van Lenthe, Filip Stockmans, and Evie E Vereecke. In vivo biomechanical behavior of the trapeziometacarpal joint in healthy and osteoarthritic subjects. *Clinical Biomechanics*, 49:119–127, 2017.

[82] Marco TY Schneider, Ju Zhang, Joseph J Crisco, Arnold-Peter C Weiss, Amy L Ladd, Kumar Mithraratne, Poul Nielsen, and Thor Besier. Trapeziometacarpal joint contact varies between men and women during three isometric functional tasks. *Medical engineering & physics*, 50:43–49, 2017.

[83] Akira Goto, Shuai Leng, Kazuomi Sugamoto, William P Cooney, Sanjeev Kakar, and Kristin Zhao. In vivo pilot study evaluating the thumb carpometacarpal joint during circumduction. *Clinical Orthopaedics and Related Research®*, 472:1106–1113, 2014.

[84] Li-Chieh Kuo, Chien-Ju Lin, Guan-Po Chen, I Jou, Chien-Kuo Wang, Irina G Goryacheva, Marat Z Dosaev, Fong-Chin Su, et al. In vivo analysis of trapeziometacarpal joint kinematics during pinch tasks. *BioMed research international*, 2014, 2014.

[85] Kemble K Wang, Xin Zhang, David McCombe, David C Ackland, Eugene T Ek, and Stephen K Tham. Quantitative analysis of in-vivo thumb carpometacarpal joint kinematics using four-dimensional computed tomography. *Journal of Hand Surgery (European Volume)*, 43(10):1088–1097, 2018.

8

[86] Fong-Chin Su, Chien-Ju Lin, Chien-Kuo Wang, Guan-Po Chen, Yung-Nien Sun, Alan K Chuang, and Li-Chieh Kuo. In vivo analysis of trapeziometacarpal joint arthrokinematics during multi-directional thumb motions. *Clinical Biomechanics*, 29(9):1009–1015, 2014.

[87] Shuai Leng, Kristin Zhao, Mingliang Qu, Kai-Nan An, Richard Berger, and Cynthia H McCollough. Dynamic ct technique for assessment of wrist joint instabilities. *Medical physics*, 38(S1):S50–S56, 2011.

[88] Benjamin Dourthe, Reza Nickmanesh, David R Wilson, Priscilla D'Agostino, Amit N Patwa, Mark W Grinstaff, Brian D Snyder, and Evie Vereecke. Assessment of healthy trapeziometacarpal cartilage properties using indentation testing and contrast-enhanced computed tomography. *Clinical Biomechanics*, 61:181–189, 2019.

[89] Eni Halilaj, David H Laidlaw, Douglas C Moore, and Joseph J Crisco. How do sex, age, and osteoarthritis affect cartilage thickness at the thumb carpometacarpal joint? insights from subject-specific cartilage modeling. In *Bioimaging and Visualization for Patient-customized Simulations*, pages 103–111. Springer, 2014.

[90] Lionel Athlani, Damien Motte, Mariette Bergere, Julie Mottet, J-Y Beaulieu, and Florent Moissenet. Assessment of trapezial prosthetic cup migration: A biomechanical study. *Hand Surgery and Rehabilitation*, 40(6):754–759, 2021.

[91] Jonathan T Kaplan, Corey P Neu, Hicham Drissi, Nancy C Emery, and David M Pierce. Cyclic loading of human articular cartilage: the transition from compaction to fatigue. *Journal of the mechanical behavior of biomedical materials*, 65:734–742, 2017.

[92] Feichen Yang, Jiacheng Zhao, William J Koshut, John Watt, Jonathan C Riboh, Ken Gall, and Benjamin J Wiley. A synthetic hydrogel composite with the mechanical behavior and durability of cartilage. *Advanced Functional Materials*, 30(36):2003451, 2020.

[93] Maksim Kovler, Katie Lundon, Nancy McKee, and Anne Agur. The human first carpometacarpal joint: osteoarthritic degeneration and 3-dimensional modeling. *Journal of Hand Therapy*, 17(4):393–400, 2004.

[94] Vincent D Pellegrini Jr. Osteoarthritis of the trapeziometacarpal joint: the pathophysiology of articular cartilage degeneration. i. anatomy and pathology of the aging joint. *The Journal of hand surgery*, 16(6):967–974, 1991.

[95] S Miyamura, K Oka, T Sakai, H Tanaka, R Shiode, S Shimada, T Mae, K Sugamoto, H Yoshikawa, and T Murase. Cartilage wear patterns in severe osteoarthritis of the trapeziometacarpal joint: a quantitative analysis. *Osteoarthritis and Cartilage*, 27(8):1152–1162, 2019.

8

[96] SC Faber, F Eckstein, S Lukasz, R Mühlbauer, J Hohe, K-H Englmeier, and M Reiser. Gender differences in knee joint cartilage thickness, volume and articular surface areas: assessment with quantitative three-dimensional mr imaging. *Skeletal radiology*, 30:144–150, 2001.

[97] Benjamin Dourthe, Priscilla D'Agostino, Filip Stockmans, Faes Kerkhof, and Evie Vereecke. In vivo contact biomechanics in the trapeziometacarpal joint using finite deformation biphasic theory and mathematical modelling. *Medical Engineering & Physics*, 38(2):108–114, 2016.

[98] Ian M Bullock, Joshua Z Zheng, Sara De La Rosa, Charlotte Guertler, and Aaron M Dollar. Grasp frequency and usage in daily household and machine shop tasks. *IEEE transactions on haptics*, 6(3):296–308, 2013.

[99] BB Seedhom. Conditioning of cartilage during normal activities is an important factor in the development of osteoarthritis. *Rheumatology*, 45(2):146–149, 2006.

[100] Li-Chieh Kuo, William P Cooney III, Kenton R Kaufman, Qing-Shan Chen, Fong-Chin Su, and Kai-Nan An. A quantitative method to measure maximal workspace of the trapeziometacarpal joint—normal model development. *Journal of Orthopaedic Research*, 22(3):600–606, 2004.

[101] J Ollie Edmunds. Current concepts of the anatomy of the thumb trapeziometacarpal joint. *The Journal of hand surgery*, 36(1):170–182, 2011.

[102] Jonathan Tsehaie, Kim R Spekreijse, Robbert M Wouters, Reinier Feitz, Steven ER Hovius, Harm P Slijper, Ruud W Selles, Hand-Wrist Study Group, et al. Predicting outcome after hand orthosis and hand therapy for thumb carpometacarpal osteoarthritis: a prospective study. *Archives of Physical Medicine and Rehabilitation*, 100(5):844–850, 2019.

[103] Christina M Ward, Taften Kuhl, and Brian D Adams. Five to ten-year outcomes of the universal total wrist arthroplasty in patients with rheumatoid arthritis. *JBJS*, 93(10):914–919, 2011.

[104] V Spartacus, A Mayoly, A Gay, T Le Corroller, M Némoz-Gaillard, S Roffino, and P Chabrand. Biomechanical causes of trapeziometacarpal arthroplasty failure. *Computer methods in BiomeChaniCs and BiomediCal engineering*, 20(11):1233–1235, 2017.

[105] Joseph J Crisco, Eni Halilaj, Douglas C Moore, Tarpit Patel, Arnold-Peter C Weiss, and Amy L Ladd. In vivo kinematics of the trapeziometacarpal joint during thumb extension-flexion and abduction-adduction. *The Journal of hand surgery*, 40(2):289–296, 2015.

[106] Yohei Kawanishi, Kunihiro Oka, Hiroyuki Tanaka, Kiyoshi Okada, Kazuomi Sugamoto, and Tsuyoshi Murase. In vivo 3-dimensional kinematics of thumb

8

carpometacarpal joint during thumb opposition. *The Journal of Hand Surgery*, 43(2):182–e1, 2018.

[107] Shigeharu Uchiyama, William P Cooney, Glen Niebur, Kai-Nan An, and Ronald L Linscheid. Biomechanical analysis of the trapeziometacarpal joint after surface replacement arthroplasty. *The Journal of hand surgery*, 24(3):483–490, 1999.

[108] Toshihiko Imaeda, William P Cooney, Glen L Niebur, Ronald L Linscheid, and Kai-Nan An. Kinematics of the trapeziometacarpal joint: a biomechanical analysis comparing tendon interposition arthroplasty and total-joint arthroplasty. *The Journal of hand surgery*, 21(4):544–553, 1996.

[109] Eni Halilaj, Michael J Rainbow, Christopher J Got, Douglas C Moore, and Joseph J Crisco. A thumb carpometacarpal joint coordinate system based on articular surface geometry. *Journal of Biomechanics*, 46(5):1031–1034, 2013.

[110] Joseph J Crisco, Tarpit Patel, Eni Halilaj, and Douglas C Moore. The envelope of physiological motion of the first carpometacarpal joint. *Journal of biomechanical engineering*, 137(10), 2015.

[111] Ge Wu, Frans CT Van der Helm, HEJ DirkJan Veeger, Mohsen Makhsous, Peter Van Roy, Carolyn Anglin, Jochem Nagels, Andrew R Karduna, Kevin McQuade, Xuguang Wang, et al. Isb recommendation on definitions of joint coordinate systems of various joints for the reporting of human joint motion—part ii: shoulder, elbow, wrist and hand. *Journal of biomechanics*, 38(5):981–992, 2005.

[112] Michael P Chae, David J Hunter-Smith, Inoka De-Silva, Stephen Tham, Robert T Spychal, and Warren Matthew Rozen. Four-dimensional (4d) printing: a new evolution in computed tomography-guided stereolithographic modeling. principles and application. *Journal of Reconstructive Microsurgery*, 31(06):458–463, 2015.

[113] WP Cooney 3rd, Michael J Lucca, EY Chao, and RL Linscheid. The kinesiology of the thumb trapeziometacarpal joint. *JBJS*, 63(9):1371–1381, 1981.

[114] Atsuro Murai, Akihiro Kurosawa, Kaoru Tada, Hiroshi Tachiya, Atsuya Tamai, Mika Akahane, Masashi Matsuta, Yuta Nakamura, Hiroki Kawashima, and Hiroyuki Tsuchiya. Optimal center of rotation for ball-and-socket thumb carpometacarpal arthroplasty identified using three-dimensional kinematic analysis. *Frontiers in Bioengineering and Biotechnology*, page 931, 2022.

[115] Jie Tang, Xudong Zhang, and Zong-Ming Li. Operational and maximal workspace of the thumb. *Ergonomics*, 51(7):1109–1118, 2008.

[116] Tianyun Yuan, Yu Song, Gerald A Kraan, and Richard HM Goossens. Identify finger rotation angles with aruco markers and action cameras. *Journal of Computing and Information Science in Engineering*, 22(3):031011, 2022.

8

[117] ASSH. Body anatomy: Upper extremity joints | the hand society.

[118] Ian M Bullock, Júlia Borràs, and Aaron M Dollar. Assessing assumptions in kinematic hand models: a review. In *2012 4th IEEE RAS & EMBS International Conference on Biomedical Robotics and Biomechatronics (BioRob)*, pages 139–146. IEEE, 2012.

[119] James J Kuch and Thomas S Huang. Human computer interaction via the human hand: a hand model. In *Proceedings of 1994 28th Asilomar Conference on Signals, Systems and Computers*, volume 2, pages 1252–1256. IEEE, 1994.

[120] Lisa Reissner, Gabriella Fischer, Renate List, Pietro Giovanoli, and Maurizio Calcagni. Assessment of hand function during activities of daily living using motion tracking cameras: A systematic review. *Proceedings of the Institution of Mechanical Engineers, Part H: Journal of Engineering in Medicine*, 233(8):764–783, 2019.

[121] Yusheng Yang, Tianyun Yuan, Toon Huysmans, Willemijn S Elkhuizen, Farzam Tajdari, and Yu Song. Posture-invariant three dimensional human hand statistical shape model. *Journal of Computing and Information Science in Engineering*, 21(3), 2021.

[122] Yusheng Yang, Jun Xu, Willemijn S Elkhuizen, and Yu Song. The development of a low-cost photogrammetry-based 3d hand scanner. *HardwareX*, 10:e00212, 2021.

[123] Gavin Buckingham. Hand tracking for immersive virtual reality: opportunities and challenges. *Frontiers in Virtual Reality*, page 140, 2021.

[124] Jen-Hsuan Hsiao, Yu-Heng Deng, Tsung-Ying Pao, Hsin-Rung Chou, and Jen-Yuan Chang. Design of a wireless 3d hand motion tracking and gesture recognition glove for virtual reality applications. In *Information Storage and Processing Systems*, volume 58103, page V001T07A007. American Society of Mechanical Engineers, 2017.

[125] Aditya Thakur and Rahul Rai. User study of hand gestures for gesture based 3d cad modeling. In *International Design Engineering Technical Conferences and Computers and Information in Engineering Conference*, volume 57052, page V01BT02A017. American Society of Mechanical Engineers, 2015.

[126] Ian M Bullock, Raymond R Ma, and Aaron M Dollar. A hand-centric classification of human and robot dexterous manipulation. *IEEE transactions on Haptics*, 6(2):129–144, 2012.

[127] Jiamin Wang, Oumar Barry, Andrew J Kurdila, and Sujith Vijayan. On the dynamics and control of a full wrist exoskeleton for tremor alleviation. In *Dynamic Systems and Control Conference*, volume 59155, page V002T27A008. American Society of Mechanical Engineers, 2019.

8

[128] Jelle Ten Kate, Gerwin Smit, and Paul Breedveld. 3d-printed upper limb prostheses: a review. *Disability and Rehabilitation: Assistive Technology*, 12(3):300–314, 2017.

[129] George F Hamilton and Peter A Lachenbruch. Reliability of goniometers in assessing finger joint angle. *Physical Therapy*, 49(5):465–469, 1969.

[130] Lisa Reissner, Gabriella Fischer, Renate List, William R Taylor, Pietro Giovanoli, and Maurizio Calcagni. Minimal detectable difference of the finger and wrist range of motion: Comparison of goniometry and 3d motion analysis. *Journal of orthopaedic surgery and research*, 14(1):1–10, 2019.

[131] Bridget Ellis and Anne Bruton. A study to compare the reliability of composite finger flexion with goniometry for measurement of range of motion in the hand. *Clinical rehabilitation*, 16(5):562–570, 2002.

[132] Erika Lewis, Lynn Fors, and William J Tharion. Interrater and intrarater reliability of finger goniometric measurements. *The American Journal of Occupational Therapy*, 64(4):555–561, 2010.

[133] Ali Erol, George Bebis, Mircea Nicolescu, Richard D Boyle, and Xander Twombly. Vision-based hand pose estimation: A review. *Computer Vision and Image Understanding*, 108(1-2):52–73, 2007.

[134] Huiyu Zhou and Huosheng Hu. Human motion tracking for rehabilitation—a survey. *Biomedical signal processing and control*, 3(1):1–18, 2008.

[135] Weiya Chen, Chenchen Yu, Chenyu Tu, Zehua Lyu, Jing Tang, Shiqi Ou, Yan Fu, and Zhidong Xue. A survey on hand pose estimation with wearable sensors and computer-vision-based methods. *Sensors*, 20(4):1074, 2020.

[136] Hanxuan Yang, Ling Shao, Feng Zheng, Liang Wang, and Zhan Song. Recent advances and trends in visual tracking: A review. *Neurocomputing*, 74(18):3823–3831, 2011.

[137] James Connolly, Joan Condell, Brendan O'Flynn, Javier Torres Sanchez, and Philip Gardiner. Imu sensor-based electronic goniometric glove for clinical finger movement analysis. *IEEE Sensors Journal*, 18(3):1273–1281, 2017.

[138] Christina Salchow-Hömmen, Leonie Callies, Daniel Laidig, Markus Valtin, Thomas Schauer, and Thomas Seel. A tangible solution for hand motion tracking in clinical applications. *Sensors*, 19(1):208, 2019.

[139] Bor-Shing Lin, I-Jung Lee, Shu-Yu Yang, Yi-Chiang Lo, Junghsi Lee, and Jean-Lon Chen. Design of an inertial-sensor-based data glove for hand function evaluation. *Sensors*, 18(5):1545, 2018.

8

[140] Tommaso Lisini Baldi, Mostafa Mohammadi, Stefano Scheggi, and Domenico Prattichizzo. Using inertial and magnetic sensors for hand tracking and rendering in wearable haptics. In *2015 IEEE World Haptics Conference (WHC)*, pages 381–387. IEEE, 2015.

[141] NDI. Aurora sensors.

[142] Giovanni Saggio, Francesco Riillo, Laura Sbernini, and Lucia Rita Quitadamo. Resistive flex sensors: a survey. *Smart Materials and Structures*, 25(1):013001, 2015.

[143] Hadrien O Michaud, Laurent Dejace, Séverine De Mulatier, and Stéphanie P Lacour. Design and functional evaluation of an epidermal strain sensing system for hand tracking. In *2016 IEEE/RSJ International Conference on Intelligent Robots and Systems (IROS)*, pages 3186–3191. IEEE, 2016.

[144] CyberGlove Systems. Cyberglove iii.

[145] Néstor J Jarque-Bou, Manfredo Atzori, and Henning Müller. A large calibrated database of hand movements and grasps kinematics. *Scientific data*, 7(1):12, 2020.

[146] Gabriella Fischer, Diana Jermann, Renate List, Lisa Reissner, and Maurizio Calcagni. Development and application of a motion analysis protocol for the kinematic evaluation of basic and functional hand and finger movements using motion capture in a clinical setting—a repeatability study. *Applied Sciences*, 10(18):6436, 2020.

[147] Jérôme Coupier, Samir Hamoudi, Sonia Telese-Izzi, Véronique Feipel, Marcel Rooze, and Serge Van Sint Jan. A novel method for in-vivo evaluation of finger kinematics including definition of healthy motion patterns. *Clinical Biomechanics*, 31:47–58, 2016.

[148] Sergio Garrido-Jurado, Rafael Muñoz-Salinas, Francisco José Madrid-Cuevas, and Manuel Jesús Marín-Jiménez. Automatic generation and detection of highly reliable fiducial markers under occlusion. *Pattern Recognition*, 47(6):2280–2292, 2014.

[149] Nathan Elangovan, Anany Dwivedi, Lucas Gerez, Che-Ming Chang, and Minas Liarokapis. Employing imu and aruco marker based tracking to decode the contact forces exerted by adaptive hands. In *2019 IEEE-RAS 19th International Conference on Humanoid Robots (Humanoids)*, pages 525–530. IEEE, 2019.

[150] Franziska Mueller, Florian Bernard, Oleksandr Sotnychenko, Dushyant Mehta, Srinath Sridhar, Dan Casas, and Christian Theobalt. Ganerated hands for real-time 3d hand tracking from monocular rgb. In *Proceedings of the IEEE conference on computer vision and pattern recognition*, pages 49–59, 2018.

8

[151] Shanxin Yuan, Qi Ye, Bjorn Stenger, Siddhant Jain, and Tae-Kyun Kim. Big-hand2. 2m benchmark: Hand pose dataset and state of the art analysis. In *Proceedings of the IEEE Conference on Computer Vision and Pattern Recognition*, pages 4866–4874, 2017.

[152] Guillermo Garcia-Hernando, Shanxin Yuan, Seungryul Baek, and Tae-Kyun Kim. First-person hand action benchmark with rgb-d videos and 3d hand pose annotations. In *Proceedings of the IEEE conference on computer vision and pattern recognition*, pages 409–419, 2018.

[153] T. Huysmans and J. F. M Molenbroek. Dined / anthropometry in design.

[154] Denis Oberkampf, Daniel F DeMenthon, and Larry S Davis. Iterative pose estimation using coplanar feature points. *Computer Vision and Image Understanding*, 63(3):495–511, 1996.

[155] Edmund Y Chao. *Biomechanics of the hand: a basic research study*. World scientific, 1989.

[156] Jennifer L McGinley, Richard Baker, Rory Wolfe, and Meg E Morris. The reliability of three-dimensional kinematic gait measurements: a systematic review. *Gait & posture*, 29(3):360–369, 2009.

[157] PL Cheng and M Pearcy. A three-dimensional definition for the flexion/extension and abduction/adduction angles. *Medical & biological engineering & computing*, 37:440–444, 1999.

[158] GI Bain, N Polites, BG Higgs, RJ Heptinstall, and AM McGrath. The functional range of motion of the finger joints. *Journal of Hand Surgery (European Volume)*, 40(4):406–411, 2015.

[159] Franziska Mueller, Dushyant Mehta, Oleksandr Sotnychenko, Srinath Sridhar, Dan Casas, and Christian Theobalt. Real-time hand tracking under occlusion from an egocentric rgb-d sensor. In *Proceedings of the IEEE International Conference on Computer Vision*, pages 1154–1163, 2017.

[160] Kraan G. Yuan T, Song Y. Comparing the active, functional, and passive range of motion of finger joints using dynamic measurement. *Convergence: Breaking down Barriers between Disciplines.*

[161] Randall D Lea and John J Gerhardt. Range-of-motion measurements. *JBJS*, 77(5):784–798, 1995.

[162] A Hemmerich, H Brown, S Smith, SSK Marthandam, and UP Wyss. Hip, knee, and ankle kinematics of high range of motion activities of daily living. *Journal of orthopaedic research*, 24(4):770–781, 2006.

8

[163] Kenichi Kono, Hiroshi Inui, Tetsuya Tomita, Takaharu Yamazaki, Shuji Take-tomi, Ryota Yamagami, Kohei Kawaguchi, Tomofumi Kage, Takahiro Arakawa, and Sakae Tanaka. Effect of weight-bearing in bicruciate-retaining total knee arthroplasty during high-flexion activities. *Clinical Biomechanics*, 92:105569, 2022.

[164] Susan J Mulholland and Urs P Wyss. Activities of daily living in non-western cultures: range of motion requirements for hip and knee joint implants. *International Journal of Rehabilitation Research*, 24(3):191–198, 2001.

[165] Douglas A Dennis, Richard D Komistek, James B Stiehl, Scott A Walker, and Kendall N Dennis. Range of motion after total knee arthroplasty the effect of implant design and weight-bearing conditions. *The Journal of arthroplasty*, 13(7):748–752, 1998.

[166] Masanobu Hirata, Yasuharu Nakashima, Daisuke Hara, Masayuki Kanazawa, Yusuke Kohno, Kensei Yoshimoto, and Yukihide Iwamoto. Optimal anterior femoral offset for functional range of motion in total hip arthroplasty—a computer simulation study. *International Orthopaedics*, 39:645–651, 2015.

[167] William J Mallon, Howard R Brown, and James A Nunley. Digital ranges of motion: normal values in young adults. *The Journal of hand surgery*, 16(5):882–887, 1991.

[168] Mary C Hume, Harris Gellman, Harry McKellop, and Robert H Brumfield Jr. Functional range of motion of the joints of the hand. *The Journal of hand surgery*, 15(2):240–243, 1990.

[169] Verónica Gracia-Ibáñez, Margarita Vergara, Joaquin L Sancho-Bru, Marta C Mora, and Catalina Piqueras. Functional range of motion of the hand joints in activities of the international classification of functioning, disability and health. *Journal of Hand Therapy*, 30(3):337–347, 2017.

[170] Franz Faul, Edgar Erdfelder, Axel Buchner, and Albert-Georg Lang. Statistical power analyses using g* power 3.1: Tests for correlation and regression analyses. *Behavior research methods*, 41(4):1149–1160, 2009.

[171] Eni Halilaj, Douglas C Moore, Tarpit K Patel, David H Laidlaw, Amy L Ladd, Arnold-Peter C Weiss, and Joseph J Crisco. Thumb carpometacarpal joint congruence during functional tasks and thumb range-of-motion activities. In *2014 36th Annual International Conference of the IEEE Engineering in Medicine and Biology Society*, pages 4354–4357. IEEE, 2014.

[172] R Degeorges and C Oberlin. Measurement of three-joint-finger motions: reality or fancy? a three-dimensional anatomical approach. *Surgical and Radiologic Anatomy*, 25:105–112, 2003.

8

[173] Jinne E Geelen, Mariana P Branco, Nick F Ramsey, Frans CT Van Der Helm, Winfred Mugge, and Alfred C Schouten. Markerless motion capture: Ml-mocap, a low-cost modular multi-camera setup. In *2021 43rd Annual International Conference of the IEEE Engineering in Medicine & Biology Society (EMBC)*, pages 4859–4862. IEEE, 2021.

[174] Sarah S Nagel, U Kneser, and B Bickert. Short report letter: combined bilateral carpal coalition of the scaphoid and trapezium and of the lunate and triquetrum. *Journal of Hand Surgery (European Volume)*, 43(1):100–101, 2018.

[175] M. Schijf. *A Clear Cut Case: The Development of a Surgical Instrument for Orthopaedic Surgery*. TU Delft, 2022.

[176] Lillian Y Chang and Nancy S Pollard. Method for determining kinematic parameters of the in vivo thumb carpometacarpal joint. *IEEE Transactions on Biomedical Engineering*, 55(7):1897–1906, 2008.

[177] Jae Hun Ryu, Natsuki Miyata, Makiko Kouchi, Masaaki Mochimaru, and Kwan H Lee. Analysis of skin movement with respect to flexional bone motion using mr images of a hand. *Journal of biomechanics*, 39(5):844–852, 2006.

[178] CD Metcalf, C Phillips, A Forrester, J Glodowski, K Simpson, C Everitt, A Darekar, L King, D Warwick, and AS Dickinson. Quantifying soft tissue artefacts and imaging variability in motion capture of the fingers. *Annals of biomedical engineering*, 48:1551–1561, 2020.

[179] Raviraj Nataraj and Zong-Ming Li. Robust identification of three-dimensional thumb and index finger kinematics with a minimal set of markers. *Journal of biomechanical engineering*, 135(9), 2013.

CURRICULUM VITÆ

Tianyun (Helen) YUAN

11-11-1992	Born in Shanghai, China.

2011–2015	Bachelor in Industrial Design
	Donghua University, Shanghai, China

2015–2017	Master in Mechanical Engineering
	Prairie View A&M University, Texas, the United States

2018–2023   PhD. in Industrial Design Engineering
Delft University of Technology, Delft, the Netherlands

Dissertation: Movement of Thumb-Base Joints: In-Vivo Anatomy and Biomechanics to Support Implant Design

Promotor: Prof. dr. ir. R.H.M. Goossens
Dr. Y. Song

Copromotor: Dr. G.A. Kraan

LIST OF PUBLICATIONS

6. **Yuan, T**, Song, Y., Blom, I.F., Mathijssen, N.M.C., Goossens, R.H.M., and Kraan, G.A. *Sex differences of the contact between trapezium and 1st metacarpal in a continuous circumduction*, submitted.

5. **Yuan, T.**, Song, Y., Blom, I.F., Mathijssen, N.M.C., Goossens, R.H.M., and Kraan, G.A. *Investigating the arthrokinematics of thumb carpometacarpal joint during circumduction with 4D CT*, submitted.

4. **Yuan, T.**, Song, Y., Goossens, R.H.M., and Kraan, G.A. *Comparing the Active, Functional, and Passive Range of Motion of Finger Joints Using Dynamic Measurement*, Proceedings of the International Conference on Healthcare Systems Ergonomics and Patient Safety, HEPS 2022.

3. **Yuan, T.**, Song, Y., Kraan, G.A., and Goossens, R.H.M., 2022, *Identify Finger Rotation Angles With ArUco Markers and Action Cameras*, Journal of Computing and Information Science in Engineering 22(3), 031011.

2. Yang, Y. **Yuan, T.**, Huysmans, T., Elkhuizen, W.S., Tajdari, F., and Song, Y., *Posture-invariant three dimensional human hand statistical shape model*, Journal of Computing and Information Science in Engineering 21 (3).

1. **Yuan, T.**, Peng, X., Zhang, D., and Li, L., *Direct 3D Printing System: from Point Cloud to Additive Manufacturing*, CAD and Applications, 17(4), pp. 825-835.